

SAND REPORT

SAND2006-7538

Unlimited Release

Printed October 2006

A Low-Power Pressure- and Temperature- Programmed Separation System for a Micro Gas Chromatograph

Joseph A. Potkay, Gordon R. Lambertus, Richard D. Sacks,
Kensall D. Wise, and Alex L. Robinson

Prepared by
Sandia National Laboratories
Albuquerque, New Mexico 87185 and Livermore, California 94550

Sandia is a multiprogram laboratory operated by Sandia Corporation,
a Lockheed Martin Company, for the United States Department of Energy's
National Nuclear Security Administration under Contract DE-AC04-94AL85000.

Additional funding provided through Engineering Research Centers Program of the National Science Foundation under
Award Number EEC-9986866.

Approved for public release; further dissemination unlimited



Sandia National Laboratories

Issued by Sandia National Laboratories, operated for the United States Department of Energy by Sandia Corporation.

NOTICE: This report was prepared as an account of work sponsored by an agency of the United States Government. Neither the United States Government, nor any agency thereof, nor any of their employees, nor any of their contractors, subcontractors, or their employees, make any warranty, express or implied, or assume any legal liability or responsibility for the accuracy, completeness, or usefulness of any information, apparatus, product, or process disclosed, or represent that its use would not infringe privately owned rights. Reference herein to any specific commercial product, process, or service by trade name, trademark, manufacturer, or otherwise, does not necessarily constitute or imply its endorsement, recommendation, or favoring by the United States Government, any agency thereof, or any of their contractors or subcontractors. The views and opinions expressed herein do not necessarily state or reflect those of the United States Government, any agency thereof, or any of their contractors.

Printed in the United States of America. This report has been reproduced directly from the best available copy.

Available to DOE and DOE contractors from
U.S. Department of Energy
Office of Scientific and Technical Information
P.O. Box 62
Oak Ridge, TN 37831

Telephone: (865) 576-8401
Facsimile: (865) 576-5728
E-Mail: reports@adonis.osti.gov
Online ordering: <http://www.doe.gov/bridge>

Available to the public from
U.S. Department of Commerce
National Technical Information Service
5285 Port Royal Rd.
Springfield, VA 22161

Telephone: (800) 553-6847
Facsimile: (703) 605-6900
E-Mail: orders@ntis.fedworld.gov
Online order: <http://www.ntis.gov/help/ordermethods.asp?loc=7-4-0#online>



A Low-Power Pressure- and Temperature- Programmed Separation System for a Micro Gas Chromatograph

Joseph A. Potkay, Gordon R. Lambertus, Richard D. Sacks, and Kensall D. Wise

Engineering Research Center for Wireless Integrated MicroSystems
The University of Michigan, Ann Arbor, MI 48109-2101

Alex L. Robinson, fellowship PI
Advanced Sensor Technologies
P.O. Box 5800
Albuquerque, NM 87185-1425

Abstract

This thesis presents the theory, design, fabrication and testing of the microvalves and columns necessary in a pressure- and temperature-programmed micro gas chromatograph (μ GC). Two microcolumn designs are investigated: a bonded Si-glass column having a rectangular cross section and a vapor-deposited silicon oxynitride (Sion) column having a roughly circular cross section. Both microcolumns contain integrated heaters and sensors for rapid, controlled heating. The 3.2 cm x 3.2 cm, 3 m-long silicon-glass column, coated with a non-polar polydimethylsiloxane (PDMS) stationary phase, separates 30 volatile organic compounds (VOCs) in less than 6 min. This is the most efficient micromachined column reported to date, producing greater than 4000 plates/m. The 2.7 mm x 1.4 mm Sion column eliminates the glass sealing plate and silicon substrate using deposited dielectrics and is the lowest power and fastest GC column reported to date; it requires only 11 mW to raise the column temperature by 100 °C and has a response time of 11s and natural temperature ramp rate of 580 °C/min. A 1 m-long PDMS-coated Sion microcolumn separates 10 VOCs in 52s. A system-based design approach was used for both columns.

The 7.5 mm x 10.3 mm integrated microvalve enables low-power pressure programming of the dual-column ensemble and is the first microvalve to utilize a hybrid actuation mechanism consisting of a thermopneumatic drive with an electrostatic hold. The valve has an open flow rate of 8 sccm at 4.6 torr, a leak rate of 1.3×10^{-3} sccm at 860 torr, a closed-to-open fluidic resistance ratio greater than one million, an actuation time

of 430 ms, and a hold power of 60 mW while closed. In addition, the valve requires no power to open, 108 mJ to close, and has a built-in position sensor with a sensitivity of 1.3 fF/torr. The design of an improved microvalve that should require only 35 mJ to close in 140 ms, a hold power of 6 mW without electrostatic latching, and no hold power with an electrostatic voltage of 180V is presented.

Overall, the valve and columns presented in this dissertation set the stage for high-performance, portable, vapor analysis instruments.

This research was performed at the University of Michigan Engineering Research Center for Wireless Integrated MicroSystems, and was partially funded by the Excellence in Engineering Fellowship through Sandia National Laboratories' LDRD University Programs. Principle Investigator Alex Robinson served as liaison and was not directly involved in performance of the work.

© Joseph Allen Potkay

All rights reserved
2006

Acknowledgements

By Joseph Potkay

First and foremost, I would like to thank God for all the gifts and blessings in my life and for all the opportunities I have been given. I hope I always seek out His will in everything I do and use His gifts wisely.

Second, I would like to thank my advisor, Dr. Ken Wise, for his guidance, wisdom, patience, understanding, and advice. I am truly lucky to have had the opportunity to be advised by someone that is not only an excellent mentor and a great human being, but also a legend in the field.

I would like to thank the members of my dissertation committee – Drs. Gianchandani, Lynch, Maharbiz and Zellers – for their advice, time, and help directing my thesis research. In addition, I would like to thank the additional members of my prelim committee: Dr. Khalil Najafi for his guidance and leadership and Dr. Richard Sacks for his expertise and his enthusiasm. He will be missed.

Next, I would like to thank all my friends at Michigan for their support and friendship. Thanks Eric, Tzeno, Helena, Sang Hyun, Jae Yoong, Allan, Andy K., Gayatri, Christine, Sunny, Amir, Rob, Razi, Randy, Shaelah, Sang Won, Jing, Ying, Jenn, and all the others that I missed. I would like to especially thank Neil Welch for our brainstorming sessions, chess games, and his knowledge, friendship and copious assistance, and Jay Mitchell for his support, openness for discussion and debate, willingness to help at any time, and fabrication help.

I would also like to thank all the students that have graduated before me, mentored me, and shown me the way. Thanks Andy, Troy, Pedram, Arvi, Patty, Junseok,

Dave, John C., Brian J., Yuan, Burcu, Hanseup, Willie, Stefan, Gary, Masoud, Mohamed, Haluk, and all the others that I missed. I especially would like to thank Dr. TJ Harpster for keeping me from being too serious and for being a caring friend. Thanks buddy.

Next, I would like to thank all of the WIMS staff for all their help and assistance, including Karen, Bonnie, Robert, Barb, Trasa, Mary, Peggy, Rose, Jonathan, Pam and Luke. I also would like to thank Mr. Joe Giachino for our discussions and for sharing his wisdom.

Next, I would like to thank all of the SSEL/MNF staff who keep the lab running smoothly and made my thesis possible. Thanks to Dr. Grimard, Brian, Brendan, Greg, Russ, Phil, Rob, Dave, Jim, Matt, Tony, Fred, Steve, Cedric, Tim, Terre, Katharine, Gerry, Dennis, and Sandrine. I especially would like to thank Ms. Ning Gulari for her processing advice, friendship, and willingness to help others.

Next, I would like to thank my parents, Debbie and Duke Benevento, for their love and support. Without their love and sacrifice, I would not be where I am today. I would also like to thank my new parents (in-laws), Bob and Judy Kiessel, for their support and making me feel like part of the family.

Finally, I would like to thank my wife, Christina, for her love, support, and patience while I have been finishing my degree. I am looking forward to the rest of our lives together.

Table of Contents

Chapter 1	17
1. 1.1 Gas-Phase Chemical Sensing	17
2. 1.2 Microfabricated Vapor Sensors	22
3. 1.3 Previous μ GC Research.....	22
4. 1.4 Temperature- and Pressure-Programmed Separations.....	27
5. 1.5 Previous Microvalve Research	29
6. 1.6 WIMS μ GC System Overview	32
7. 1.7 Research Summary	34
Chapter 2.....	36
8. 2.1 System-Based Column Theory and Design.....	36
9. 2.2 Pressure Sensor Design and Simulation	40
10. 2.3 Fabrication	42
11. 2.4 Testing and Results.....	46
12. 2.5 Integration into the Environmental Monitor.....	52
Chapter 3.....	54
13. 3.1 Motivation and Background	54
14. 3.2 System-Based Column Theory and Design.....	57
15. 3.3 Thermal Modeling	61
16. 3.4 Sion Column Fabrication.....	64
17. 3.5 Sion Column Testing and Results.....	70
Chapter 4.....	76
18. 4.1 Device Concept.....	77
19. 4.2 Design and Analysis	79
20. 4.3 Fabrication	99

21. 4.4 Testing and Results.....	105
22. 4.5 An Improved Microvalve	114
Chapter 5.....	115
23. 5.1 Thesis Summary	115
24. 5.2 Suggestions for Future Work.....	117
Distribution List.....	128

List of Figures

Figure 1.1: A simple diagram of a traditional gas chromatography system.	20
Figure 1.2: The first integrated μ GC, reported by Stanford in 1979 [1].....	23
Figure 1.3: The Microsensor Technology GC system (left) and a separation of 9 VOCs that it achieved in less than 50 seconds [2].....	23
Figure 1.4: The components of the Sandia μ ChemLab® project (left) [3] and the recent monolithic version (right) [4].....	24
Figure 1.5: Components of the SLS Micro Technology hand-held GC system [5].	25
Figure 1.6: The size and energy progress of GC systems.....	26
Figure 1.7: Diagram showing the concept of pressure programming. In (a), the valve is closed and flow passes through both columns. In (b), the valve is open, and flow is stopped in the first column and doubled in the second column.	28
Figure 1.8: A bistable valve with pneumatically coupled membranes and electrostatic actuation [6].	31
Figure 1.9: A mechanically bistable electromagnetically actuated microvalve [7].....	32
Figure 1.10: Conceptual drawing of the WIMS μ GC system.....	33
Figure 2.1: Contour plot of the number of theoretical plates, N , as a function of the column width and column length [59]. The column depth and differential pressure are fixed at 250 μ m and 0.4 atm, respectively.	39
Figure 2.2: Contour plot of the hold-up time, t_m , as a function of the column width and column length [59]. The column depth and differential pressure are fixed at 250 μ m and 0.4 atm, respectively.	39

Figure 2.3: Diagram of the pressure sensor structure.	40
Figure 2.4: Theoretical pressure sensor response for different side lengths.....	42
Figure 2.5: The non-etched back 1 m (left) and 3 m (right) columns.....	43
Figure 2.6: The complete silicon-glass column process flow, including integrated pressure sensors.	44
Figure 2.7: 0.9 and 3m columns (upper right) etched back to reduce their thermal mass. The inset on the left is a channel that was broken to inspect the wall thickness.	45
Figure 2.8: A SEM of the integrated pressure sensors and etched back column and a picture of the front and back of a 3m silicon-glass column die (inset).....	46
Figure 2.9: Chromatogram achieved using the 3 m column coated with a non-polar stationary phase. The injection pulse was 250 ms wide, the differential pressure was 0.5 atm, and the temperature of the column was ramped from 58 °C to 74 °C at 9 °C/min [48]......	48
Figure 2.10: A 30 component separation achieved using the 3m column in under 6 minutes [56].	49
Figure 2.11: Photograph of the pressure sensors and column in the test setup.	50
Figure 2.12: Measured capacitance versus differential pressure for the bossed pressure sensor at the inlet and midpoint of the column.	51
Figure 2.13: Measured capacitance versus differential pressure for the bossed pressure sensor at the outlet of the column.	51
Figure 2.14: An early μ GC prototype [photo courtesy of E. Gamble]	52
Figure 2.15: The separation of a 7-vapor mixture achieved using an early μ GC prototype [63]. The analysis was performed at 25 °C and split flow injection was employed to decrease the peak width exiting the preconcentrator. Compounds in the mixture: 0 water; 1 trichloroethylene; 2 toluene; 3 perchloroethylene; 4 n-butyl acetate; 5 m-xylene; 6 styrene; 7 n-nonane	53
Figure 3.1: Drawing of the Sion column structure.	56
Figure 3.2: Simplified cross section of the Sion microcolumn.....	56
Figure 3.3: Average carrier flow rate for different column lengths versus the column diameter. An inlet and outlet pressure of 1 atm and 0.5 atm (380 torr), respectively, were assumed.	59

Figure 3.4: The number of theoretical plates for different column lengths versus the column diameter. An inlet and outlet pressure of 1 atm and 0.5 atm (380 torr), respectively, were assumed.....	59
Figure 3.5: Holdup time for different column lengths versus the column diameter. An inlet and outlet pressure of 1 atm and 0.5 atm (380 torr), respectively, were assumed.	60
Figure 3.6: Model for thermal losses of the suspended dielectric column.	61
Figure 3.7: Equivalent circuit for thermal model of the suspended dielectric column. The numbers represent the values at 100 °C in vacuum; thus, losses through the surrounding air are negligible.	61
Figure 3.8: Theoretical power loss (at a 100 °C temperature rise) as a function of pressure for a 0.5 m column suspended at 2 points using the model in Fig. 3.7. The model predicts a power consumption of 14 mW in vacuum.	64
Figure 3.9: Process flow for the low mass microcolumns. The column is formed from a released stress free PECVD dielectric layer with Ti/Pt heaters. Stress minimization of both the dielectric layer and the metal layer is critical for release. Au-Si eutectic formation bonds the two wafers together.....	65
Figure 3.10: Cross section of a sealed buried channel with a height of 72µm, width of 97µm, and ceiling thickness of 15µm.....	66
Figure 3.11: SEM of a side view of the broken column just before release. The Au-Si eutectic bond is visible in the middle left of the picture, where the two wafers come into contact.....	68
Figure 3.12: SEMs of the bottom side of the released dielectric column.....	68
Figure 3.13: Picture of the center heater and channels, looking through the bottom side of the transparent column.....	69
Figure 3.14: Picture of the side heater and suspended inlet, looking through the bottom side of the transparent column.	69
Figure 3.15: Picture of the finished column on a dime. The three ports can be seen in the upper left, bottom middle and upper right of the die. The integrated sensor array is on the right.	70
Figure 3.16: Measured steady-state temperature versus power data for a single heater in the suspended column.	72

Figure 3.17: Measured power loss of the column versus pressure. The deviation from the theoretical graph is due to temperature non-uniformity at higher pressures. The power required in vacuum represents over a 5X improvement in power over previously published devices.	72
Figure 3.18: Measured transient response of one of the heaters in the column.	73
Figure 3.19: Separation 10 components in 52s using the 1 m column. A temperature program of 30-100 °C at 50 °C/min was used in conjunction with a flame ionization detector.	74
Figure 3.20: Separation of four CWA simulants and an explosive simulant in 60s utilizing the 1 m column. A temperature program of 30-100 °C at 50 °C/min was used in conjunction with a flame ionization detector.	75
Figure 4.1: Drawing which displays the main components of the microvalve.	77
Figure 4.2: 3D drawing of the microvalve.	78
Figure 4.3: The theoretical deflection of the valve diaphragm. The two curves show the impact of the diaphragm thickness on the diaphragm's response.	81
Figure 4.4: First order thermal circuit for thermopneumatic actuator.	82
Figure 4.5: Simulated transient response for the energized thermopneumatic actuator, without latching. The input power of 250 mW was applied at 0s and removed at 20s.	83
Figure 4.6: A top view drawing of the heater grid. The black lines represent the individual p++ silicon beams and the grey rectangles are the anchors.	85
Figure 4.7: The n th node in the distributed thermal model of the heater.	86
Figure 4.8: Theoretical temperature distribution of all the nodes in the heater grid after applying 250 mW for 400 ms.	87
Figure 4.9: Theoretical temperature distribution of one row of the heater grid after applying 250 mW for 400 ms.	88
Figure 4.10: A plot of the actuation cavity pressure versus temperature based on the Clausius-Clapeyron relation. Pentane was used in the current devices.	90
Figure 4.11: Theoretical pressure transient response utilizing the simple thermal model and the Clausius-Clapeyron equation.	90
Figure 4.12: Theoretical open flow rate for a differential pressure of 5 torr showing the effect of the channel length and height.	92
Figure 4.13: Theoretical valve flow rate as a function of valve plate deflection.	93

Figure 4.14: The theoretical response of the position sensor.....	94
Figure 4.15: Theoretical response of the position sensor as a function of actuation pressure.	95
Figure 4.16: Theoretical effect of the spring constant of the diaphragm on the electrostatic hold voltage.....	96
Figure 4.17: The fabrication process for the top half of the microvalve.	100
Figure 4.18: The remainder of the fabrication process for the microvalve.	101
Figure 4.19: A SEM of the bottom side of the valve diaphragm showing the corrugations and valve plate.	102
Figure 4.20: Picture of the bottom of the finished valve body wafer.	103
Figure 4.21: Picture of the top of the finished valve body wafer.	103
Figure 4.22: SEM of the full heater die. The bond ring surrounds the heater and the electrical leads can be seen at the bottom of the picture.....	104
Figure 4.23: SEM of the suspended heater grid, anchor, recess, and electrical feedthrough.	104
Figure 4.24: The finished valve die (right) and bottom side of the valve body (left)....	105
Figure 4.25: Measured open flow rate for the valve.....	106
Figure 4.26: Measured response of the position sensor.....	107
Figure 4.27: Valve flow rate as a function of the actuation pressure.	108
Figure 4.28: Measured results for the pneumatic switching (1500 torr) of 0.06 sccm. .	109
Figure 4.29: Measured results for the pneumatic switching (1500 torr) of 2.1 sccm. ...	110
Figure 4.30: Measured thermopneumatic transient response with 90 mW applied to the heater.....	111
Figure 4.31: Measured thermopneumatic transient response with 200 mW applied to the heater.....	112
Figure 4.32: Measured thermopneumatic transient response with 250 mW applied to the heater.....	112
Figure 4.33: Measured leak rate versus applied electrostatic latch voltage. An actuation pressure of 2000 torr was used in conjunction with the electrostatic latch.....	113

List of Tables

<p>Table 1.1: A survey of microvalve technologies and performance from industry (top half) and academia (bottom half). $P_{diff,max}$ is defined as the maximum pressure that the valve can close under. Some of the data below is taken from [34]. Technology key: tpneu- thermopneumatic; EM - electromagnetic; ES - electrostatic; SMA - shape memory alloy; bimet - bimetallic; piezo - piezoelectric</p>	30
<p>Table 3.1: Thermal properties of the column materials.....</p>	62
<p>Table 3.2: GSI PECVD process parameters for the stress free oxynitride structural film. </p>	67
<p>Table 3.3: STS ICP Etcher process parameters for the dry, isotropic channel etch.</p>	67
<p>Table 3.4: Measured response time of the corner and center of the column while actuating the corner heaters. This represents a 4X improvement in speed over previously published devices.</p>	73
<p>Table 4.1: Thermal properties of the relevant valve materials.</p>	82
<p>Table 4.2: Properties of various possible working fluids for the thermopneumatic actuator.....</p>	89
<p>Table 4.3: Tradeoffs in the valve design. A_E is the area of the electrostatic hold, t this the dielectric thickness for the electrostatic hold, h is the diaphragm thickness, and d is the heater recess depth. \uparrow signifies an increase, \downarrow signifies a decrease, and $-$ signifies no change.....</p>	98

Chapter 1

Introduction

The research described in this dissertation centers around the design and fabrication of a low-power pressure- and temperature-programmed separation system for a micro gas chromatograph (μ GC). Thus, this dissertation focuses on two main components: a microcolumn that is the heart of the μ GC and performs the gaseous separation, and microvalves that modulate the column pressure, thereby enhancing separation in the dual-column system. The current chapter introduces gas sensing, microfabricated sensing devices and systems, and presents an overview of the WIMS μ GC system. Subsequent chapters cover the microcolumns and valves.

1.1 Gas-Phase Chemical Sensing

Accurate gas and vapor sensing is critically needed for a wide variety of applications, including industrial process control, food processing/monitoring, environmental monitoring, pharmaceutical screenings, health care, and homeland security. The targeted compounds range from water vapor to environmental pollutants and chemical warfare agents, and span a large range of volatilities. In each application, it is important to identify and quantify some or all of the chemical species in a mixture.

All chemical sensors (detectors) utilize a mechanism to transduce or convert the desired information from the chemical domain into the electrical domain, where it can be

processed using analog and digital electronic circuitry. There are several important performance metrics for chemical sensors. The ideal sensor would consume no power, occupy a small footprint, exhibit high sensitivity, be stable, have a fast response, and be highly selective. However, the importance of each of these metrics depends on the application, and tradeoffs exist among many of them.

Numerous chemical sensing technologies exist or have been pursued in the past. A complete review of chemical sensors is given elsewhere [8, 9], but a brief review of the technologies follows. In the following review, the chemical transducers relevant to this dissertation are grouped into four general categories: electrochemical sensors, mass sensors, optical sensors and spectrometers. It should be noted that some detector technologies have been omitted and some of the detectors have characteristics that cover multiple categories. Nevertheless, the review is adequate as an introduction to gas-phase sensing and to motivate the work of this thesis. After the review, gas chromatography is introduced as a method to improve the selectivity of chemical detectors.

In electrochemical sensors, a chemical species interacts with the device, usually by absorption, and alters its electrical characteristics. In a chemiresistive sensor, for example, chemicals adsorbed onto a film alter the film's resistivity [10]. On the other hand, in a flame ionization detector (FID), another electrochemical sensor, ions generated by burning organic compounds produce a current that is collected and quantified. However, the sample is destroyed in the process. In yet another electrochemical sensor, the Chemical Field Effect Transistor (CHEMFET), the work function of the metal-insulator-semiconductor structure varies when exposed to gaseous components. Finally, in a thermal conductivity detector (TCD), the thermal conductance of the gas surrounding

the sensor varies based on the gas composition and concentration, and this in turn alters the temperature (and resistance) of the device.

In mass sensors, interacting chemicals alter the mass of the sensor which in turn alters one of its electrical properties. In a surface acoustic wave (SAW) sensor [11], for example, the resonant frequency of a piezoelectric structure is altered when interacting with a chemical species.

Optical sensors utilize the unique optical properties of different gases to identify them. In an infrared-based detector (IRD), for example, an infrared beam scans the gas sample at different frequencies and the returned spectrum is compared to known spectra [12].

In spectrometers, the chemical species being analyzed is dispersed according to some property (e.g. mass or energy) and the dispersion is measured. In Mass Spectrometry (MS) systems, the gas to be analyzed is bombarded with an electron beam with sufficient energy to fragment the molecules. The resulting charged particles are accelerated in a vacuum through a magnetic field, which sorts the charged particles on the basis of mass-to-charge ratio. This spectrum is then analyzed to determine the original components of the gaseous mixture. This approach, however, damages the original gas molecules. In addition, mass spectrometers typically require large amounts of energy to ionize the sample, require very low pressures, and have a complex designs.

The above-mentioned transducers perform well in controlled environments; however, in an arbitrary environment with a complex mixture of gaseous components, they often generate incorrect results. That is, because of poor selectivity, they respond to unintended compounds and, in many applications, this is unacceptable. Recently,

multiple (electrochemical or mass) sensors have been combined in devices known as sensor arrays or electronic noses. In these arrays, the different devices achieve partial selectivity relative to each other, usually through the use of different thin film coatings on each device. Pattern recognition is used to analyze the response pattern of the array and results in improved analysis of mixtures. However, to date, sensor arrays and pattern recognition have only been successfully used for simple mixtures [13-16].

Separation systems, such as gas chromatography (GC) systems, provide enhanced selectivity and analysis of complex mixtures by isolating or separating some or all individual component in the mixture. The chemical can be identified after isolation utilizing one of the detectors above and the magnitude of the sensor response determines its concentration. In a more powerful technique, a separation system can be combined with a spectrometer or sensor array in order to further improve selectivity.

In a gas chromatography system, shown in Fig. 1.1, the separation process begins when a sample is injected into a separation channel or column. The column is usually coated with a thin film, known as the stationary phase, which enhances the separation

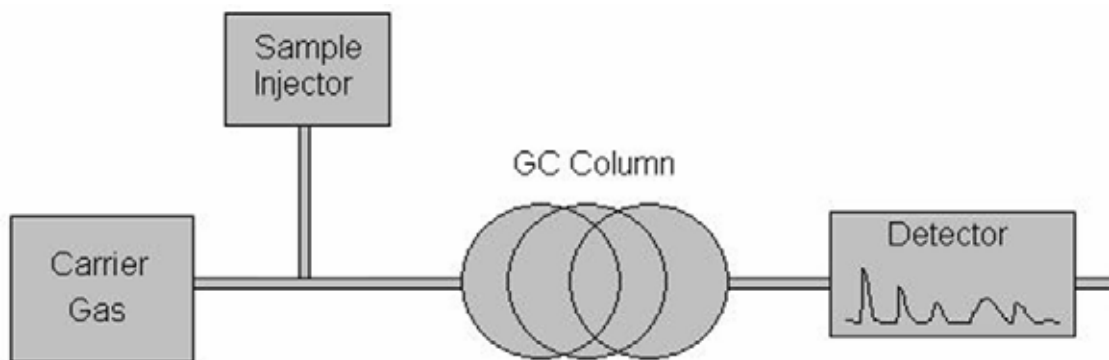


Figure 1.1: A simple diagram of a traditional gas chromatography system.

ability of the column and can be chosen based on the targeted compounds. As a carrier gas (such as helium, hydrogen or nitrogen) transports the sample through the column, the individual components in the mixture spend different amounts of time absorbed in the stationary phase on the wall of the column. This process is dependent on several variables, including component vapor pressures and polarities, column temperature, carrier gas velocity, and stationary phase characteristics. In general, compounds that spend less time in the stationary phase exit the end of the column first, where they are detected. Thus, the elution time can be used to identify the compound, and the magnitude of the detector signal can be used to determine its concentration.

Commercial GC systems exist, but are inconvenient in field use due to variables such as size and power. Examples of commercial GC systems are the Agilent 3000, which consumes 70W, has a 10ppm detection limit and an analysis time (not including preconcentration) of 3 minutes, and the Varian 4900, which consumes up to 180W, but has a detection limit of 1ppm. The price of such commercial systems varies based on specifications and configuration, but typically is around \$20,000 to \$50,000. In the case of some commercial GCs, gas samples are collected in the field and analyzed in the laboratory using a conventional GC, but this process is inefficient at best. By miniaturizing such systems, lower power levels may be achieved, facilitating analysis directly in the field. The addition of integrated preconcentrators to such miniaturized microsystems could also aid in reducing analysis time relative to commercial systems.

1.2 Microfabricated Vapor Sensors

Micromachined vapor sensor systems, in general, offer several advantages over their macroscopic counterparts. The first advantage is the increased portability of the system due to its decreased size. Micromachined sensing systems can be distributed in environments in which their macroscopic counterparts cannot. With regard to thermal properties, micromachining permits the creation of very low-mass, highly isolated structures that may be heated rapidly, reducing the response time of and power required for many devices. In addition, as a device is scaled down to a smaller size, the ratio of surface area to volume increases, a property that can be highly advantageous in the separation process of gas chromatography, as well as in other devices. With regard to cost, micromachined devices can be batch fabricated in parallel, reducing the cost of the system. However, in many cases, this advantage does not apply to the packaging and testing of the device, although many advances are being made in this area. While all of the above advantages have sparked research in the miniaturization of many vapor sensing systems, past devices have still lacked speed, sensitivity, stability or selectivity. A micro GC (μ GC) system potentially provides solutions to all of these problems, especially selectivity, since it is capable of separating components in space and time.

1.3 Previous μ GC Research

The first efforts to produce an integrated μ GC began in 1970 at Stanford [1]. The system, developed by Terry, et. al., and shown in Fig. 1.2, was fabricated on single 50 mm silicon wafer and contained a sample injector, a separation column, and a

detector. In 1992, Microsensor Technology, Inc, reported a μ GC system with a micromachined injector and TCD detector, and a miniature, but not micromachined, fused silica column [2]. The system achieved several notable results, including the separation of 9 VOCs in less than 50 seconds, as shown in Fig. 1.3. In 1994, Reston and Kolesar reported a three component (injector, column and detector) miniature GC

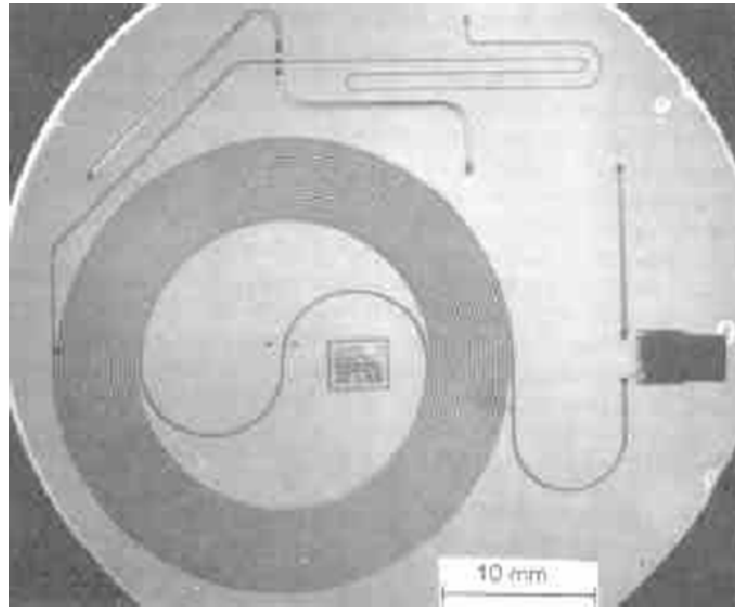


Figure 1.2: The first integrated μ GC, reported by Stanford in 1979 [1].

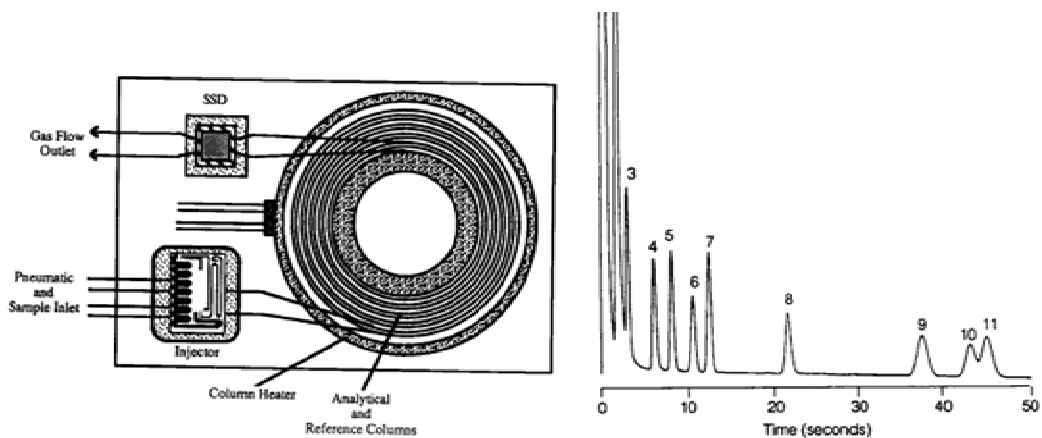


Figure 1.3: The Microsensor Technology GC system (left) and a separation of 9 VOCs that it achieved in less than 50 seconds [2].

[17]. The system targeted the separation and detection of ammonia and nitrogen dioxide by coating the column with a copper phthalocyanine (CuPc) stationary phase. The system also utilized a dual detector scheme – a TCD and a chemiresistor – to improve selectivity and sensitivity to certain compounds.

In 1996, the efforts in this field were accelerated when Sandia National Laboratories began work on the μ ChemLab[®] project. The system contains a microfabricated preconcentrator, a silicon-on-glass microcolumn with a high-aspect-ratio rectangular cross section, and a SAW sensor array detector as shown in Fig. 1.4 [3]. More recently, Sandia has fabricated a monolithic version of its μ ChemLab[®] with integrated preconcentrator, column and detector [4]. No separation results have been published, however. In 1998, Lawrence Livermore published work on 5 m-long fusion

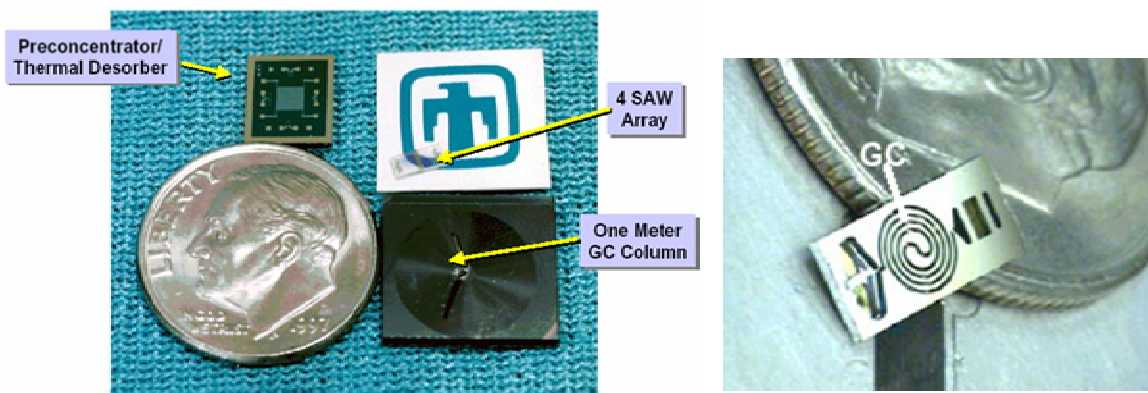


Figure 1.4: The components of the Sandia μ ChemLab[®] project (left) [3] and the recent monolithic version (right) [4].

bonded circular column. In more recent work, the column has been incorporated into a hand-held gas chromatography system consuming 24 W and weighing 8 lbs [18]. In 2000, the Technical University of Hamburg-Harburg presented work on micromachined separation columns with a plasma polymerized stationary phase and successfully demonstrated the separation of several alkanes. The column achieved roughly 1000

plates [19]. In 2002, Noh and Hesketh at Georgia Tech made progress towards lower power with their work on parylene columns with embedded heaters. These columns achieved a 70 °C temperature rise in 30s at 45 mW and had very low mass, but no experimental separations were demonstrated [20].

In industry, work in GC's with micromachined components has accelerated as well. SLS Micro Technology of Germany has commercialized a 70g hand-held GC system, shown in Fig. 1.5, which consumes 20 W of power and achieves a sensitivity of 7 ppm. The column in the system occupies an area of 2 cm² and requires 5 W to heat it to 200 °C in 30s [5]. Another startup company, C2V in the Netherlands is producing a 206 cc, 3 W, part-per-million sensitivity μ GC system with microfabricated valves

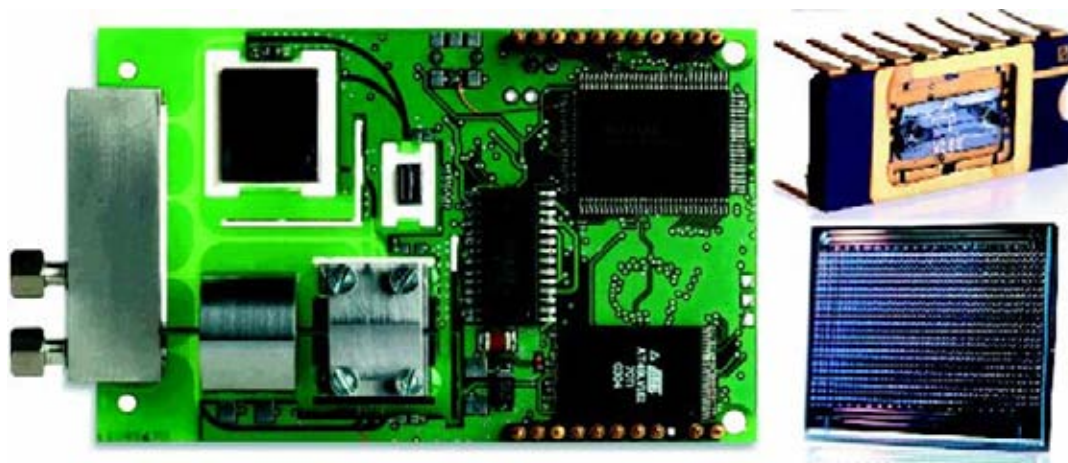


Figure 1.5: Components of the SLS Micro Technology hand-held GC system [5].

and TCD [21]. It utilizes a conventional capillary column and external carrier gas, however. Other new μ GC companies include Sandia spin-offs Defiant Technologies [22] and Nanodetex [23].

Although all of these efforts have yielded important progress, they have not yet provided the high performance and low-power operation needed for many applications.

In addition, none of the systems developed to date have been completely miniaturized or fully integrated.

More recently, the Defense Advanced Research Projects Agency (DARPA) Micro Gas Analyzer (MGA) program, started in 2004, seeks to develop a 2 cc, 0.5 J per analysis, part-per-trillion sensitivity, 4s analysis-time micro gas analyzer for the detection of chemical warfare agents (CWAs) [24]. With Honeywell, Sandia, and the University of Illinois involved, the project promises to advance the field of μ GCs even further.

Figure 1.6 displays a summary of the progress in GC systems in terms of energy and size and the projected specifications for the WIMS μ GC system.

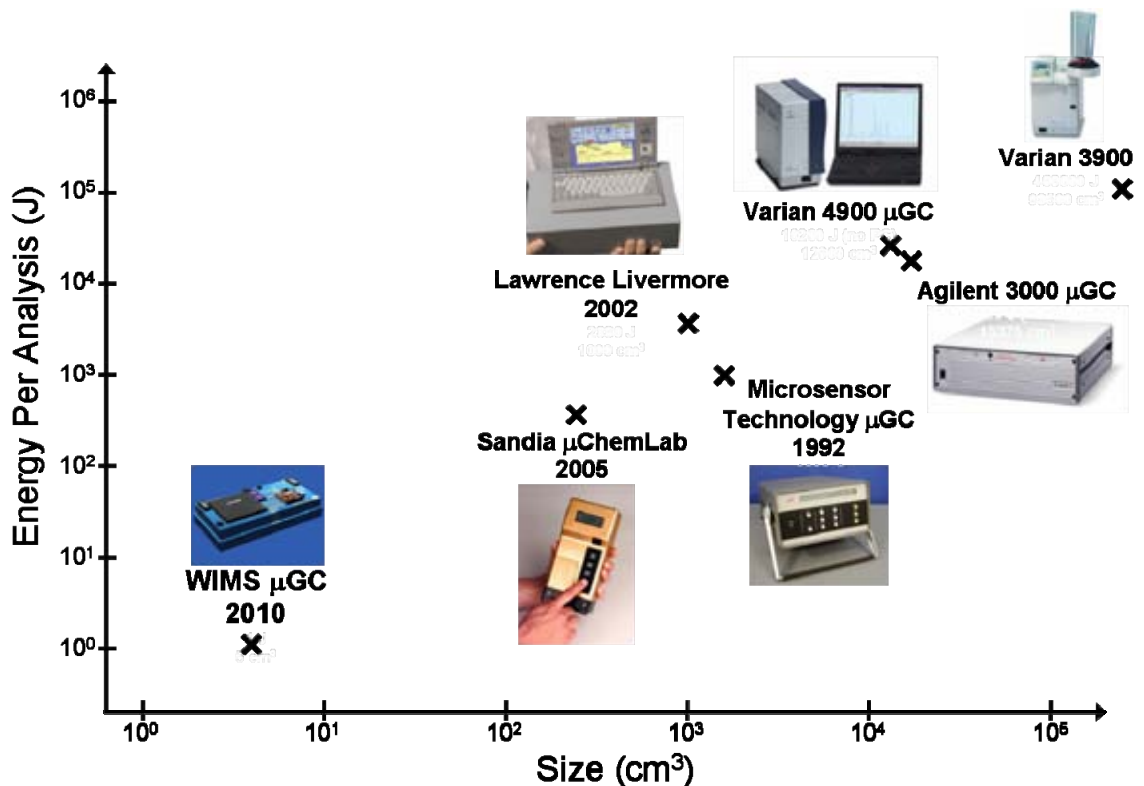


Figure 1.6: The size and energy progress of GC systems.

1.4 Temperature- and Pressure-Programmed Separations

Temperature and pressure programming of the column in a GC system has proven useful in reducing the system analysis time and in improving the separation ability of the column. Furthermore, models have been developed to predict the effect of programming on the final chromatogram [25].

Temperature programming is based on the fact that the column temperature has a large impact on the sorption and desorption of gases into and out of the stationary phase (i.e., their retention) [26-28], and thus on the overall analysis time. In fact, temperature programming can provide a significant decrease in the analysis time of mixtures of components that span a large range of boiling points with only a small decrease in resolution [25, 29, 30]. During temperature programming, the column temperature is typically ramped from a low temperature to a high temperature; these temperatures depend on the targeted components in the mixture. Faster temperature ramp rates are used to decrease analysis time. However, maintaining a column temperature greater than ambient and changing the column temperature (ramping) can require large amounts of power and energy. Thus, to minimize power, it is important that the column be designed to be thermally efficient.

Pressure programming utilizes the fact that the separation of components is dependent on the carrier gas flow rate, which is directly related to the differential pressure across the column. This dependence on flow rate is discussed in Sections 2.1 and 3.2. Pressure programming can be achieved in several ways, including using a programmable pressure source or mass flow controller. However, a much simpler

approach is shown in Fig 1.7. In this approach, the separation column has been split into two sections (one non-polar, one polar) with a valve in parallel with the first column.

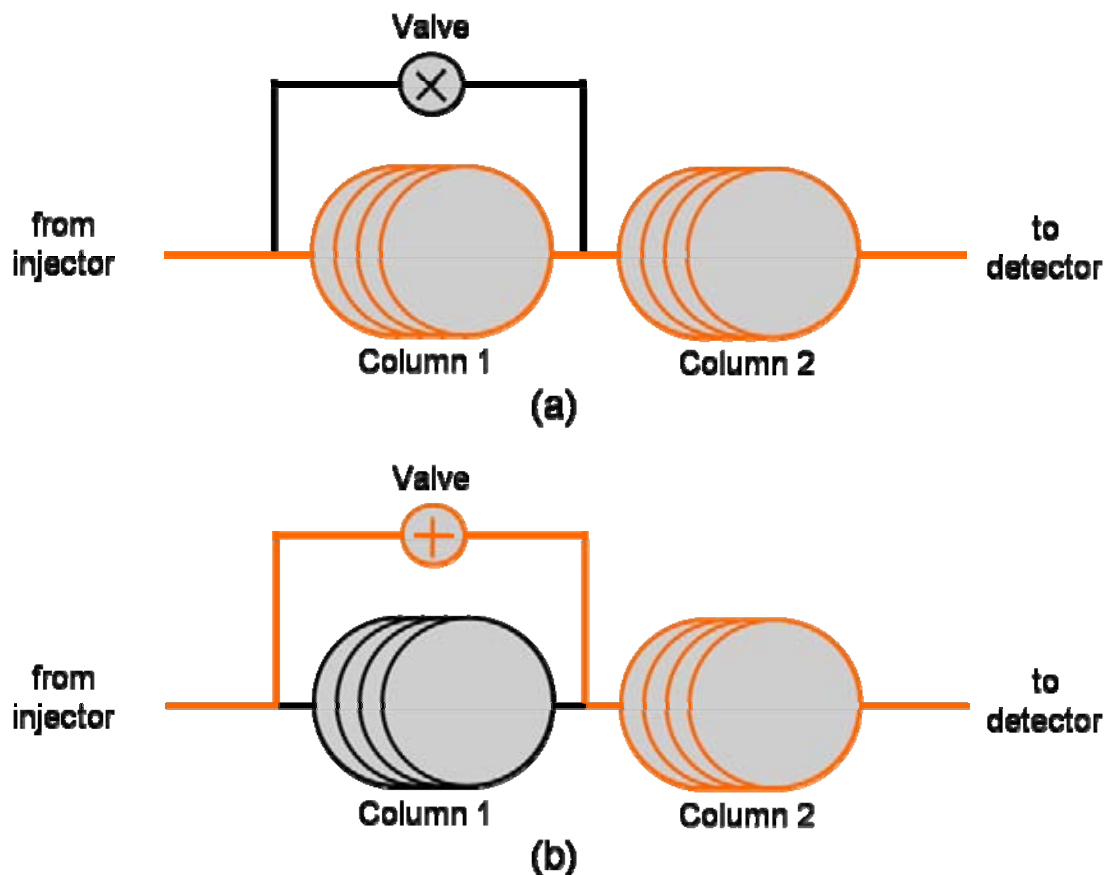


Figure 1.7: Diagram showing the concept of pressure programming. In (a), the valve is closed and flow passes through both columns. In (b), the valve is open, and flow is stopped in the first column and doubled in the second column.

During normal operation, this valve is closed (there is no flow through it) and flow passes through both columns to the detector. To achieve pressure programming, or tuning, the valve is opened. In this configuration, the pressure across the first column is zero and the pressure across the second column has doubled. This approach has been shown to improve the separation ability of a column using timed pressure pulses to separate components that otherwise overlap [25, 31-33].

In order to achieve a micromachined separation system that is capable of both pressure and temperature programming, two main components are needed: a column and valve. The column should be split into two parts, each of which are thermally isolated and individually temperature programmable. The valve is utilized to bypass the first column and achieve pressure programming. Finally, both components should be designed to be power efficient in order to minimize energy consumption.

1.5 Previous Microvalve Research

Most portable microfluidic analysis systems (with applications in health care, chemical and biological detection and DNA analysis) require a valving system with similar performance requirements. Specifically, a valve for such systems should consume very little power to accommodate the use of a battery, have a large clearance (high throw) to facilitate the passage of large biological or chemical samples, be able to remain closed in the face of a large hold off pressure, and have a low leak rate, low dead volume, and a fast response time. For the WIMS μ GC system, the valves should be very low power (to facilitate battery operation), have a large open flow (so that it does not load the micropump), be able to switch medium pressures (up to 0.5 atm), have a low leak rate (< 0.01 sccm), and have a medium response time (< 500 ms) to enable pressure programming of the columns.

Numerous valve designs have been explored in the past both in industry and academia, some of which are tabulated in Table 1.1. However, each type of valve actuation mechanism has its advantages and disadvantages. Specifically, electrostatic actuators are extremely low power and have fast response times, but are sensitive to

Table 1.1: A survey of microvalve technologies and performance from industry (top half) and academia (bottom half). Pdiff,max is defined as the maximum pressure that the valve can close under. Some of the data below is taken from [34]. Technology key: tpneu- thermopneumatic; EM - electromagnetic; ES - electrostatic; SMA - shape memory alloy; bimet - bimetallic; piezo - piezoelectric

Affiliation and Year	Technology	Open Flow (sccm @ psid)	Leak (sccm)	Power (mW)	Actuation Time (ms)	Pdiff,max (psid)	Comments
IC Sensors 4425 [35]	Bimet	125 @ 10	0.02	400	50 0-100-0%	15	Pdiff limited, high power
Redwood, 1997 [36]	Tpnue	1500 @ 20	0.02 @ 20psid	7500	1000	100	Very high power, slow
Hitachi [37]	ES	~10 ⁴ @ 24	???	~0	13 0-100%	24	Exotic material, hybrid structure
Deutsche Aerospace [38]	EM/ES	2 @ 1.45	0.01	50	0.4 0-100%	2.3	Pdiff limited, hybrid structure
MIT, 2004 [39]	ES	8.4 @ 10	0.00035@14.7	~0	???	12	<35V req'd, low flow, Pdiff limited
Univ. of Tsukuba [40]	SMA	1600 @ 17.4	???	450	17.4	2000	High power, hybrid structure
Cal. Inst. Of Tech., 2003 [41]	Piezo	52 @ 300	10 ⁻⁴ @ 800 psid	4	10	1000	Low flow, 30V req'd to fully open, hybrid design
GA Tech, 2000 [7]	EM	330 @ 0.9	???	0, 380 to close	38	???	Mechanically bistable
Cal. Inst. of Tech, 1999 [42]	Tpnue	3600 @ 30	???	650	1000	???	Lifetime in days, req. silicone rubber
UMich, 2003 [43]	Tpnue	400 @ 29	0.001 @ 15.5 psid	300	1500	>29	Some non-batch fab., high power, slow
UMich, 2006	Tpnue/ES	8 @ 0.1	0.001 @ 16.6 psid	60, 250 to close	430	>17	Current work

particulates and have low clearance and low open flow. Electromagnetic valves can achieve good performance, but the forces scale unfavorably for devices with small volume and hybrid steps are typically required in the fabrication. Piezoelectric actuators have displayed large actuation forces and fast response times, but have low throw and require large voltages and hybrid assembly. Sol-gel based valves have achieved large volumetric displacement, but usually require liquid for actuation. Thermopneumatic valves are robust and have high force and large throw, but require continuous power to remain actuated and require non-batch fabricated assembly steps. A complete overview of the different actuation mechanisms and published examples are given in [44].

Recently, attempts have been made to combine multiple actuation principles in hybrid or sometimes bistable designs. These attempts are targeted at utilizing the advantages of each actuation principle and, at the same time, alleviating their disadvantages. For instance, in 1996 Wagner, et. al., investigated a valve based on two pneumatically coupled membranes and electrostatic actuation. When one electrode is pulled down electrostatically, the other is forced upward pneumatically. The valve structure is shown in Fig. 1.8, however, no valving data was reported [6]. In 1993,

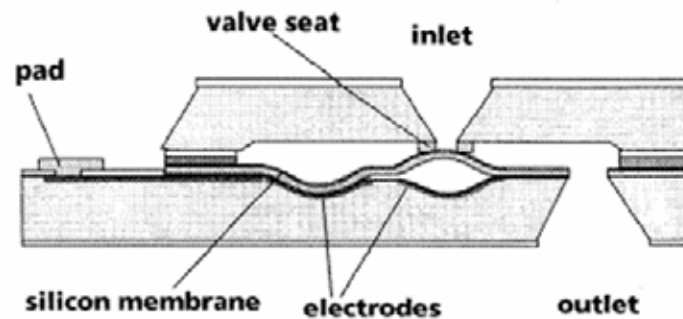


Figure 1.8: A bistable valve with pneumatically coupled membranes and electrostatic actuation [6].

Deutsche Aerospace developed a hybrid electromagnetic and electrostatic actuator. The valve consumed 50 mW of power when actuated, had a 0.4 ms response time and a leak rate of 0.01 sccm, but could only switch low differential pressures and required hybrid fabrication steps [38]. In 2000, Capanu, et. al., at Georgia Tech presented an electromagnetically-actuated valve with mechanical bistability [7]. The microvalve had a high flow conductance, required 380 mW to transition between states and had a response time of 38 ms. However, the device structure, shown in Fig. 1.9, was complex and the fabrication required hybrid steps. In 2004, Frank and Pisano reported a mechanically bistable valve with electrolysis actuation [45]. The valve required less than

1 mW to transition between states, had a leak rate of approximately 0.002 sccm at 14.7 psi, but required 10 s to close and had a low open flow rate.

Chapter 4 of this dissertation presents a valve that contains a hybrid thermopneumatic and electrostatic actuator and enables pressure programmed separations and flow control in the μ GC system.

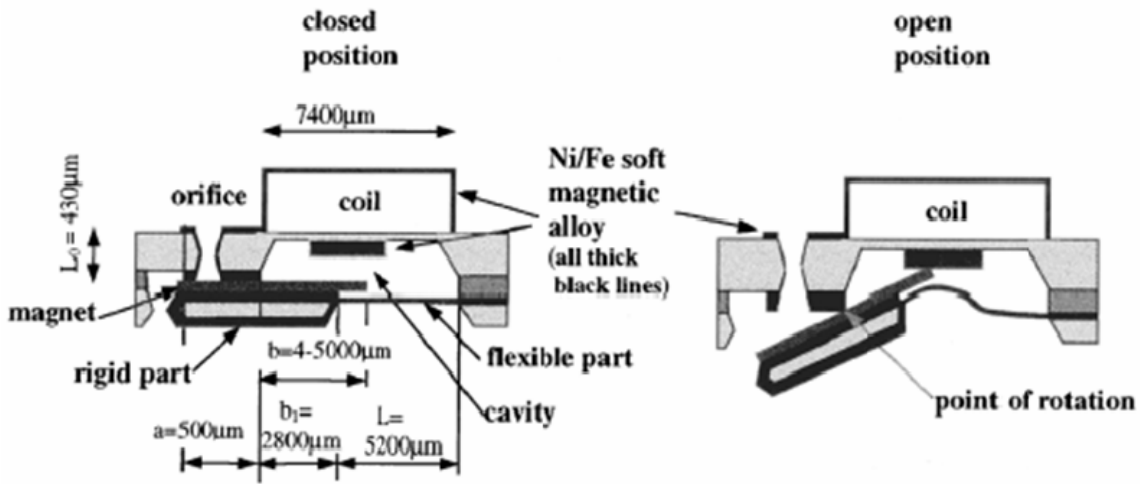


Figure 1.9: A mechanically bistable electromagnetically actuated microvalve [7].

1.6 WIMS μ GC System Overview

The research described herein forms the heart of a μ GC intended for an environmental monitoring system that is currently under development as part of the National Science Foundation Engineering Research Center for Wireless Integrated Microsystems (NSF WIMS ERC). This microsystem, which will monitor temperature, pressure, humidity, and gas composition with part-per-billion sensitivity, is targeted at less than 5 cc with an average power of less than 10 mW. The finished system will analyze 30+ volatile organic compounds (VOC's) in less than 5 min. A conceptual view

of the fully integrated μ GC is shown in Fig. 1.10. It will consist of an inlet filter, internal standard, pre-concentrator [46, 47], separation columns [48-51], a chemiresistive sensing array [10, 52], a vacuum pump [53, 54], and integrated microvalves [55]. The columns in the final system will be suspended, thin-walled, and low mass, and they will be pressure and temperature programmable.

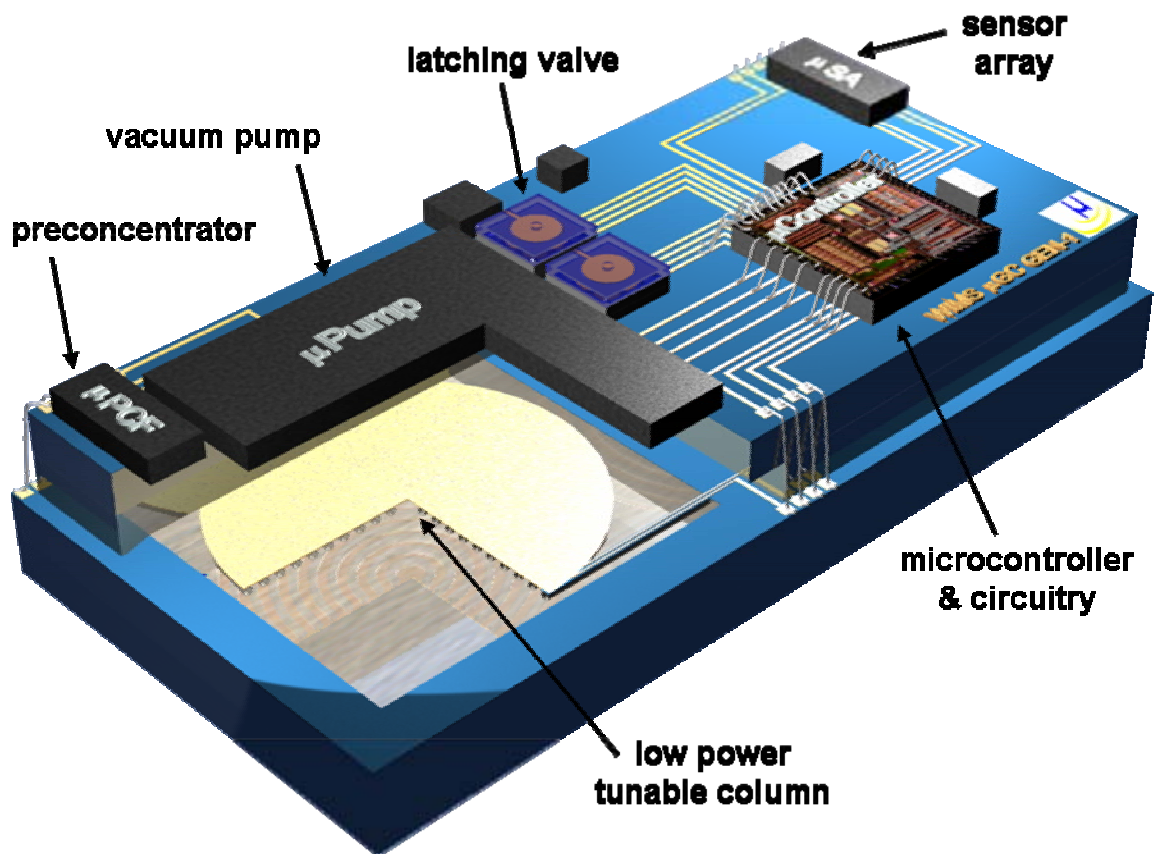


Figure 1.10: Conceptual drawing of the WIMS μ GC system.

1.7 Research Summary

The research objectives of this dissertation are all aimed at a specific goal: creating a functional pressure- and temperature-programmed separation column for the WIMS μ GC system. Thus, it deals with the design, fabrication and testing of two main components: a low-mass, low-power microcolumn with integrated heaters and temperature sensors, and a low power microvalve that enables pressure tuning and flow control in the μ GC.

Two approaches to column design are investigated here. In the first, the column is formed via a high-aspect-ratio (HAR) deep reactive ion etch (DRIE). The column mass is minimized and pressure sensors are formed at the inlet and outlet through boron diffusions and an etch-back step. In the second approach, a zero stress dielectric membrane is undercut using a dry etch to form the channel in silicon. This channel is then sealed and coated using zero-stress chemical vapor deposited (CVD) dielectrics. The silicon is then etched away in order to release the structure. The former approach is simple to fabricate and is used to verify theoretical models and experimentally test coating and column programming, while the latter is the key to low power and fast operation.

For the valve, a hybrid thermopneumatic and electrostatic microvalve is investigated. Thermopneumatic drive provides a large force and large throw, while the electrostatic latch is used to reduce or eliminate standby hold power. Thus, the valve ideally only consumes power when transitioning from the open to the closed state. In addition, a thermally isolated actuation cavity is used to further reduce power.

Chapter 2 discusses the theory, fabrication, test and integration of the glass-bonded column. Chapter 3 reviews the development and testing of the Sion microcolumns. The microvalve theory, fabrication and results are discussed in Chapter 4 and Chapter 5 concludes the thesis.

Chapter 2

A Silicon-Glass Micro Gas Chromatography Column

This chapter presents the theory, fabrication, and experimental results for a microfabricated gas chromatography column capable of performing multi-component separations using air as a carrier gas and vacuum at the outlet. These features are necessary to the realization of a wristwatch-size gas chromatograph (μ GC), but pose significant challenges in the design of a high-performance column. Columns 0.9m and 3.0m long were fabricated using a deep reactive ion etch (DRIE) and were sealed with a glass cap. The 3.0 m-long non-polar column occupies 3.2 cm x 3.2 cm, has separated 30 gaseous components in under 6 minutes, and achieves over 4000 plates/m. The fabrication process has been extended to minimize the mass of the columns and facilitate low-power operation. Some of the work presented in the chapter and additional work on these columns were presented in [48], [49], [50] and [56].

2.1 System-Based Column Theory and Design

The performance of gas chromatography columns is conventionally measured in terms of the total number of theoretical plates (N), which is a measure of the resolving power of the column, and in terms of the height equivalent to a theoretical plate (H), which is a measure of the efficiency of the column. Golay performed the first analytical modeling of gas chromatography channels in 1958 [57]. When adapted to square

channels, which were chosen for their efficient use of die area and ease of fabrication, the H, as given in [58], is:

$$H = 2 \frac{D_g}{u} + \frac{1 + 9k + \frac{51}{2}k^2}{105(1+k)^2} \frac{uw^2}{D_g} + \frac{8h^2ku}{3D_l(1+k)^2}, \quad (2.1)$$

where D_g and D_l are the diffusion coefficients in the gas and liquid phases, respectively, k is the retention factor, h is the thickness of the liquid phase, and w is the channel width. The average carrier gas velocity, u , is given by Eq. 2.2, where u_o is the outlet gas velocity, f_2 is the Martin-James gas compression correction factor, p_o is the outlet pressure, p_i is the inlet pressure, η is the carrier gas viscosity, and L is the column length.

$$u = u_o f_2 = \frac{w^2 p_o \left(\left(\frac{p_i}{p_o} \right)^2 - 1 \right)}{96\eta L} f_2, \quad (2.2)$$

To determine the total resolving power of a column, the total number of plates, N , is calculated as

$$N = \frac{L}{H}, \quad (2.3)$$

where L is the total length of the column. Finally, the holdup time, t_m , is the time it takes for an unretained component to be injected into the system and travel through the column to the detector. It is calculated as in Eq. 2.4:

$$t_m = \frac{L}{u}, \quad (2.4)$$

For the μ GC under development, several factors constrained the design and performance of the system. Using vacuum at the outlet enables miniaturization through the integration of a MEMS vacuum pump. However, as the outlet pressure in Eq. 2.2

decreases, the flow rate saturates resulting in diminishing returns for large differential pressures. This is in contrast to conventional systems where inlet pressure can be adjusted freely to improve the column performance.

To eliminate the need for gas storage and enable further miniaturization, air was chosen as the carrier gas; however, because it has a higher viscosity than conventional carrier gases (such as hydrogen), the flow rate is diminished, hampering separation performance. Moreover, high flow rates are desirable to sweep the sample through the detector and reduce tailing of the peaks. Another disadvantage of using air as the carrier is that diffusion occurs more slowly in air (smaller D_g than helium or hydrogen), further reducing H in Eq. 2.1.

Finally, the analysis time was limited to less than 10 minutes to meet the goals of the system, and the initial channel depth was limited to 500 μm (the wafer thickness), although this was subsequently reduced to minimize power requirements, process time, reduce die area, and decrease device costs.

Given these constraints, Eqns. 2.1-2.4 were to predict the optimum channel width, depth, and length. Although, the fabricated channels were rectangular and not square, Eq. 2.1 still provides a good approximation. In collaboration with the Richard Sacks' laboratory in the Department of Chemistry at the University of Michigan, the contour plots in Figs. 2.1 and 2.2 were generated using these equations and show the tradeoff

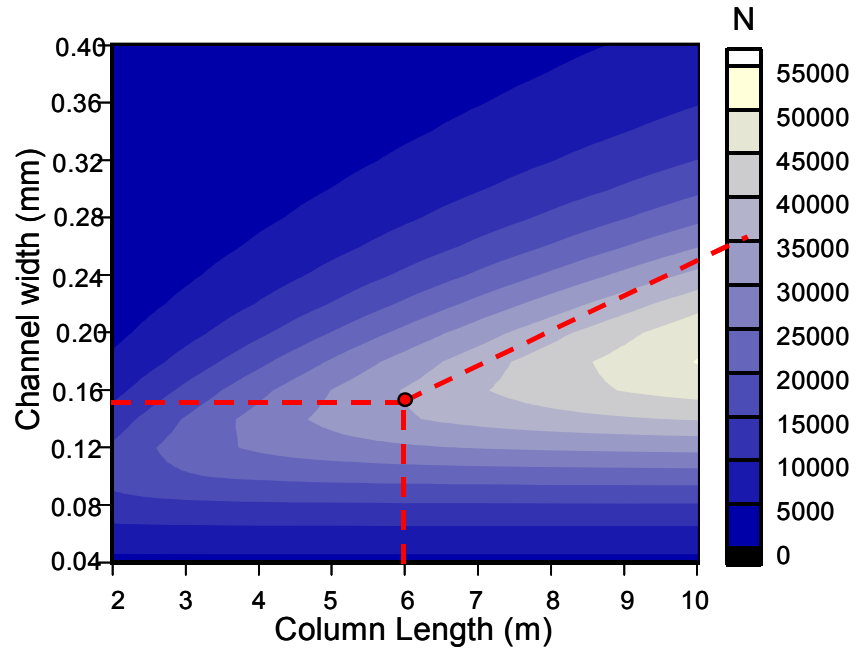


Figure 2.1: Contour plot of the number of theoretical plates, N , as a function of the column width and column length [59]. The column depth and differential pressure are fixed at 250 μm and 0.4 atm, respectively.

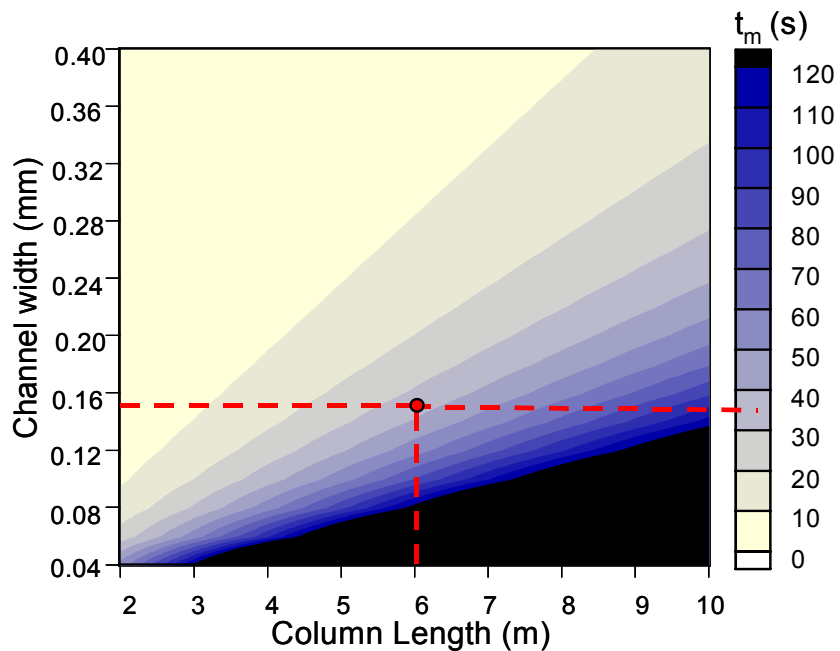


Figure 2.2: Contour plot of the hold-up time, t_m , as a function of the column width and column length [59]. The column depth and differential pressure are fixed at 250 μm and 0.4 atm, respectively.

between resolving power and analysis time for a 250 μm -deep rectangular channel. In both plots, it is more desirable to operate in the lighter regions; the red circles indicate the chosen operating point. This operating point results in a channel width of 150 μm and a total length of 6 m, giving roughly 35,000 theoretical plates of resolving power and a hold up time of approximately 35 seconds. Assuming maximum retention factors to be less than 10 and isothermal operation, analysis times of 6 minutes or less for all 30 targeted components is expected. For some applications, the column length can be shortened to achieve to achieve higher speed separations.

2.2 Pressure Sensor Design and Simulation

The pressure sensors were designed targeting a proven technology based on a released shallow boron membrane [60]. In this technology, one plate of the capacitive sensor is fixed on a glass substrate and the other is formed from a 4 μm -deep shallow boron diffusion, which deflects with changes in the differential pressure across it. In order to prohibit shorting of the two electrodes, a 2000 \AA -thick low temperature oxide (LTO) is deposited on top of the shallow boron membrane. The structure is show in Fig. 2.3 with an optional rigid central region (or boss) in the diaphragm.

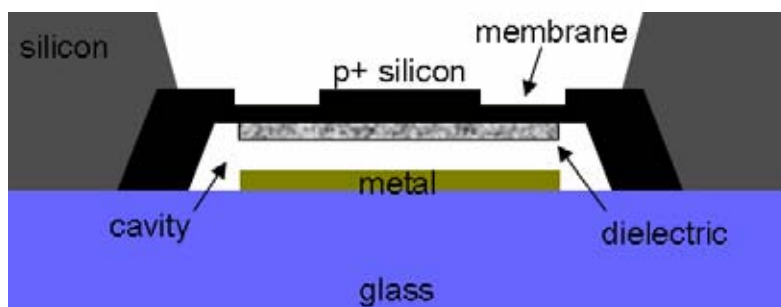


Figure 2.3: Diagram of the pressure sensor structure.

The equation governing the deflection of the center of a bossed, circular diaphragm is estimated in [61] and [62]. In addition, [61] gives the central deflection of a square diaphragm as approximately 28% greater than a circular diaphragm (when its diameter is equal to the side length of the square diaphragm). Thus, Eqn. 2.5 estimates the central deflection of a square, bossed diaphragm from the analysis in [62] and [61] as:

$$\frac{Pa^4}{Eh^4} = \frac{y}{1.28 \times A_p h} + \frac{B_p y^3}{1.28 h^3}, \quad (2.5)$$

where, y is the center deflection of the diaphragm, ν is the Poisson's ratio of the diaphragm, E is the Young's modulus of the diaphragm material, h is the thickness of the diaphragm, P is the differential pressure applied to the diaphragm, and a is the length of a side of the diaphragm. A_p and B_p are functions of the Poisson's ratio, side length and side length of the boss and are given in [61]. The equation is valid for stress free diaphragms, although a term may be added to the right side of Eqn. 2.5, as in [61] to account for stress.

The total capacitance of the pressure sensor is determined as a series combination of the capacitance of the air (which is a function of pressure) and the capacitance of the isolation dielectric (which is constant). Both capacitances may be determined as:

$$C = \frac{\epsilon A}{d}, \quad (2.6)$$

where, C is the capacitance, ϵ is the permittivity, A is the capacitor area, and d is the gap distance. Figure 2.4 displays the result of combining Eqns. 2.5 and 2.6 for several diaphragm side lengths. Assuming a shallow boron diaphragm thickness of 4 μm , a gap of 12 μm , and a side length of 1.1 mm (limited by die area), the constants A_p and B_p evaluate to 0.14 and 5.9, respectively. With these values, the model predicts a sensitivity

of 5.1 fF/torr over the required pressure range. Given the appropriate circuitry, this is sufficient for the several torr pressure accuracy required for device operation and repeatability; that is, a run-to-run repeatability of several torr in the differential pressure results in a 1% run-to-run hold-up time repeatability. It should also be noted that the diaphragm thickness has a large impact on the device sensitivity. Decreasing the thickness from 4 μm to 3.5 μm increases the sensitivity from 5.1 to 10.6 fF/torr.

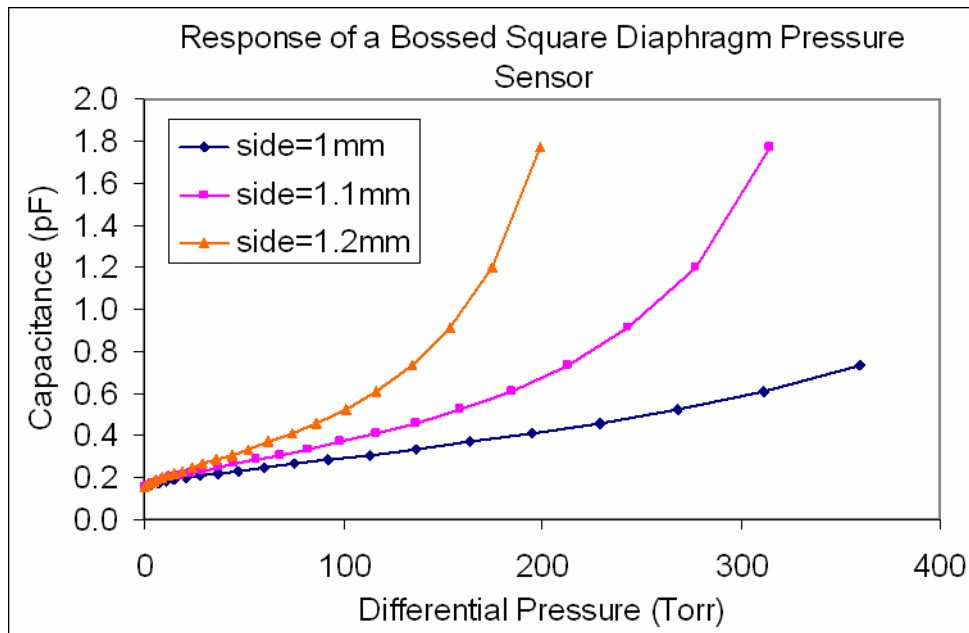


Figure 2.4: Theoretical pressure sensor response for different side lengths.

2.3 Fabrication

Initially, a simple column fabrication process was used for rapid device design and testing. This process utilized a deep reactive-ion etch (DRIE) process, which involved etching a 150 μm -wide, 260 μm -deep recessed groove into a silicon wafer. The wafer was then anodically bonded to a glass plate to close the channel. Columns lengths

of 0.9 m (2 cm x 2 cm die) and 3 m (3.2 cm x 3.2 cm die) were formed using this approach and were sent to Restek Corporation for coating with appropriate polar and non-polar stationary phases. Pictures of the 0.9 m and 3.0 m columns are shown in Fig. 2.5. Chromatograms achieved using these columns are described in the next section.

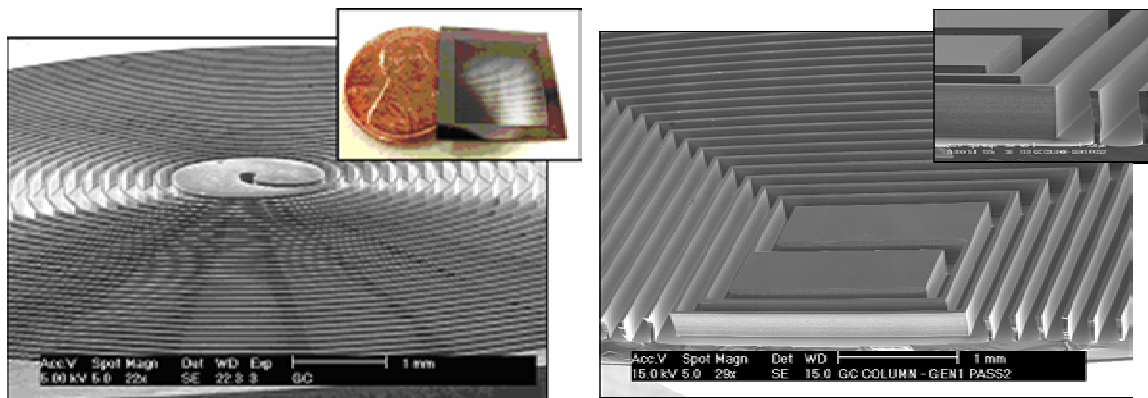


Figure 2.5: The non-etched back 1 m (left) and 3 m (right) columns.

Since the columns must be thermally efficient yet very fast and must contain integrated pressure sensors, the fabrication process was extended as shown in Fig. 2.6. First, a 10 μm dry isotropic etch was performed to form the recess for the pressure sensors. Next, a 1.2 μm -thick thermal oxide was grown on a p-type $\langle 100 \rangle$ silicon wafer, which served as a diffusion mask in later steps. The oxide was patterned using buffered HF and subsequently photoresist PR9260 was spun to a thickness of approximately 12 μm . The PR9260 provided a mask for DRIE, which was performed next, and resulted in a channel 150 μm wide and 260 μm deep. After the resist was stripped, boron was diffused at 1100 $^{\circ}\text{C}$ to form a p⁺⁺ etch stop about 10 μm deep. The oxide diffusion barrier oxide was then stripped and a 4 μm deep shallow boron deposition was performed to form the diaphragm of the pressure sensor. A Pyrex 7740 wafer with patterned

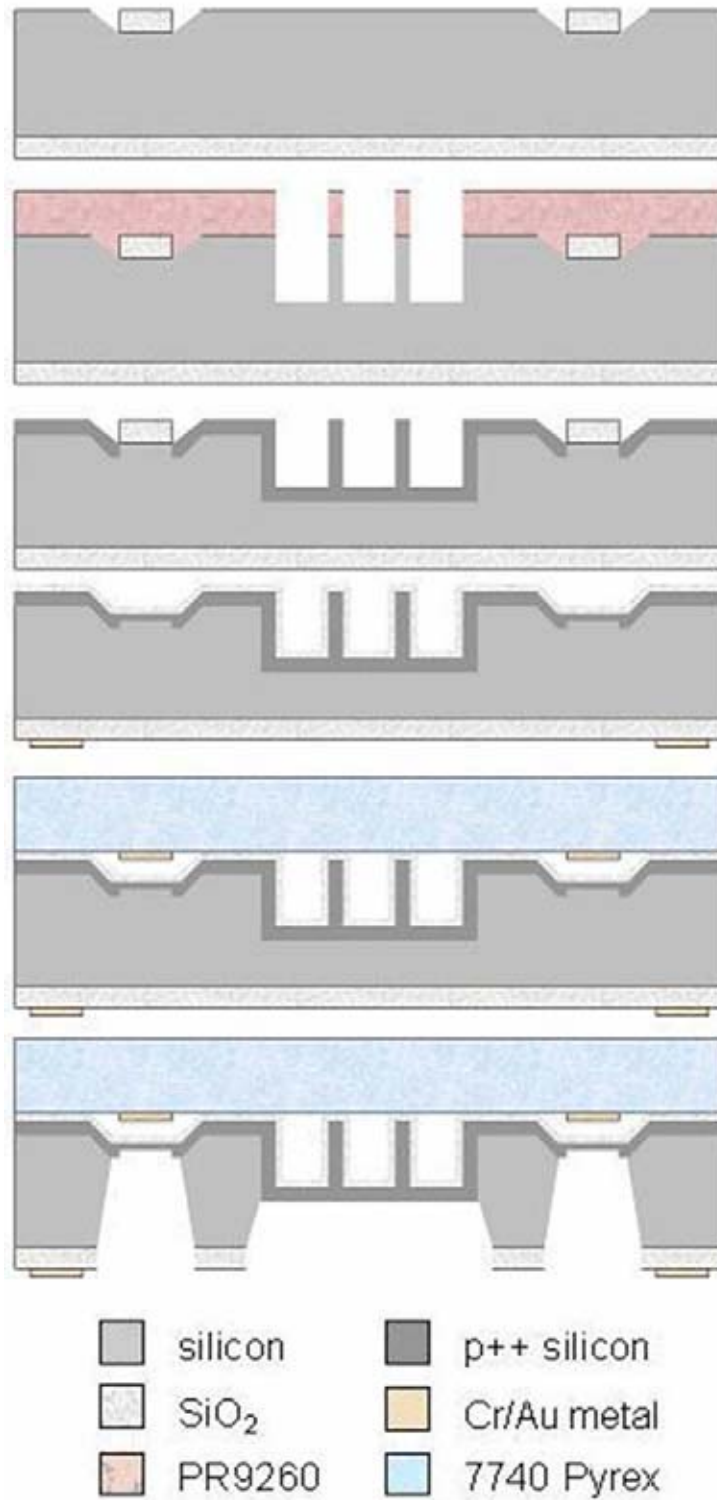


Figure 2.6: The complete silicon-glass column process flow, including integrated pressure sensors.

chromium-gold electrodes was then anodically bonded to the silicon substrate at 1000 V, 400 °C, and 200 N to cap the channel. Finally, the backside oxide was patterned and the device was etched back in ethylene diamine pyrocatechol (EDP) in order to release the channel and pressure sensors. The wafer was then diced to separate the die and open up the entry and exit ports. By boron doping the channel walls and then etching away the excess silicon, the mass of the column is minimized, reducing its thermal capacitance and facilitating rapid heating of the device. Pictures of the etched-back 0.9 m and 3.0 m columns are shown in Fig. 2.7. An etched back 3m column with integrated pressure sensors is shown in Fig. 2.8.

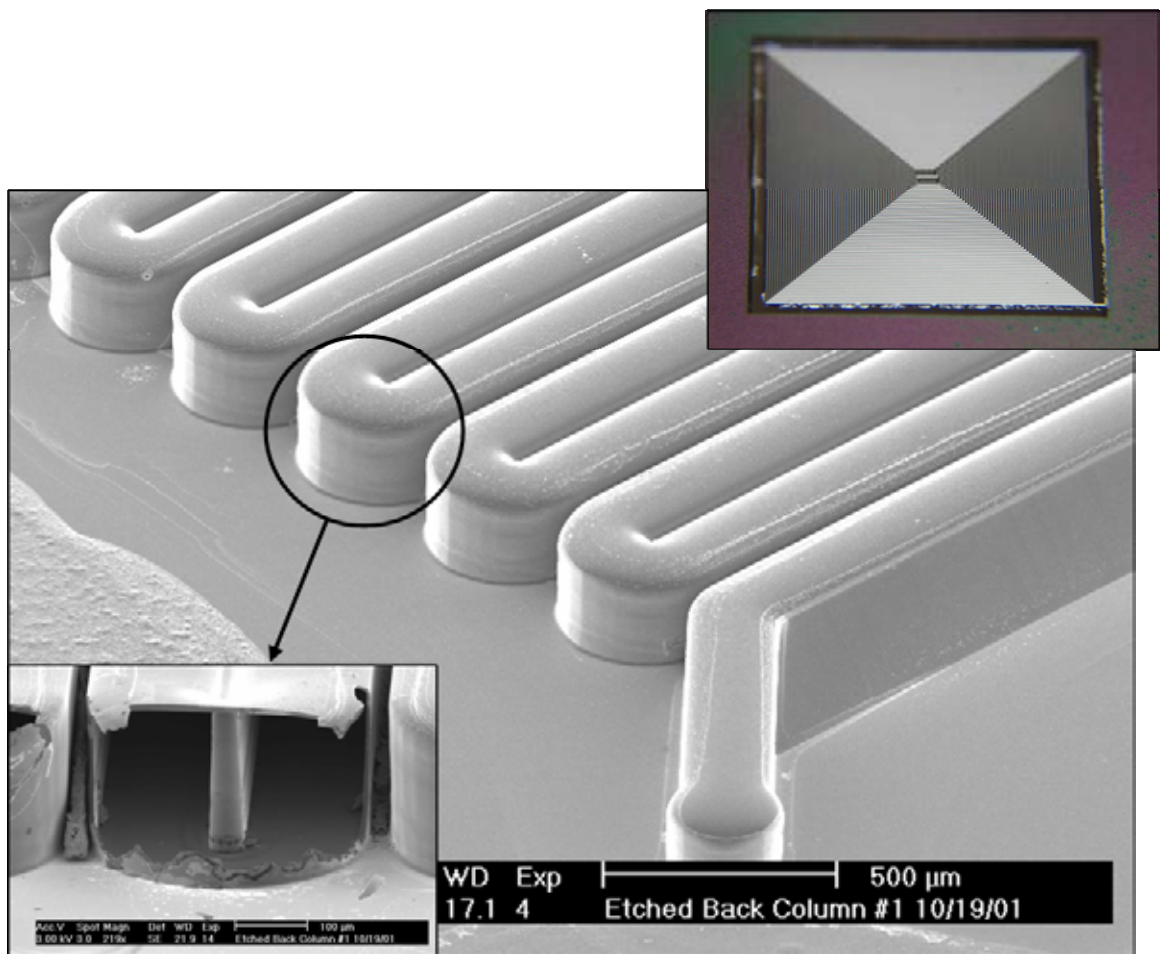


Figure 2.7: 0.9 and 3m columns (upper right) etched back to reduce their thermal mass. The inset on the left is a channel that was broken to inspect the wall thickness.

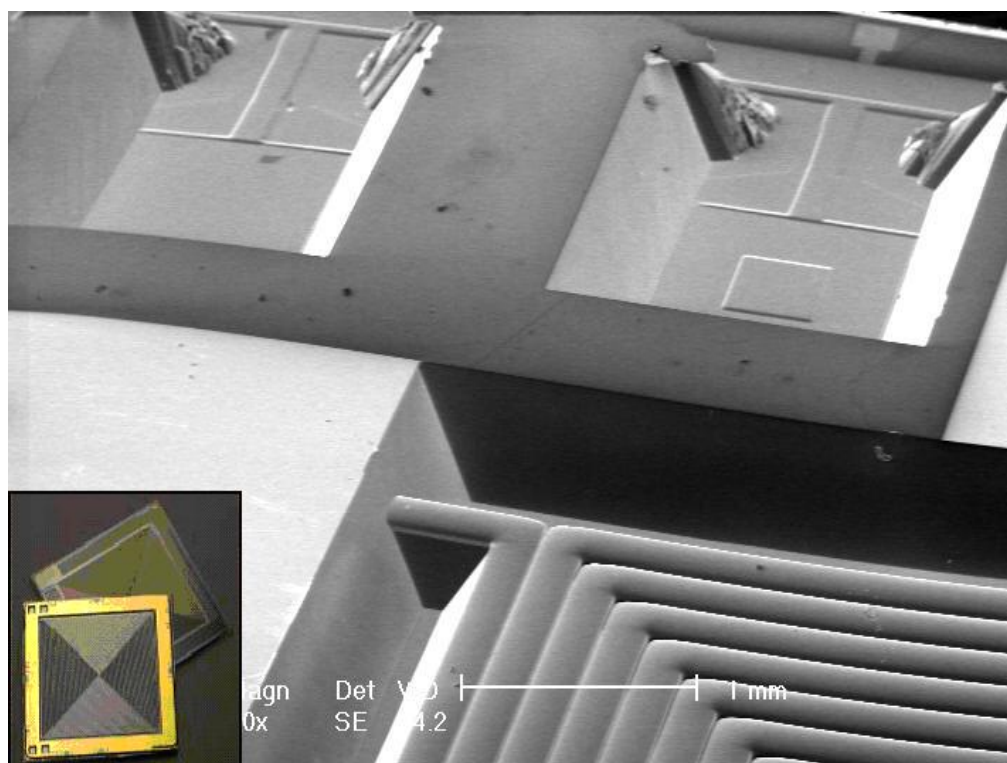


Figure 2.8: A SEM of the integrated pressure sensors and etched back column and a picture of the front and back of a 3m silicon-glass column die (inset)

2.4 Testing and Results

After fabrication, a burst pressure test was performed on the column to test the strength of the bond and durability of the walls between the channels. The column was tested for pressures up to 60 psi (this entire pressure exists across the column wall) and remained undamaged. Subsequently, the flow rates of the columns were tested and found to be within 10% of the theoretical values, giving a first-order verification of the modeling results. The flow rates were approximately 1.9 standard cm^3/min (sccm) and 0.6 sccm for the 0.9 m and 3.0 m columns, respectively, for a differential pressure of 0.4 atm (304 torr).

Next, the thermal characteristics of the etched-back 0.9 m column were tested. For this test, electrical contacts were made directly to the column and the p⁺⁺ silicon of the channel walls was used as the heater and had a resistance of 5 Ω . The average temperature and temperature gradient were measured using a thermal imaging infrared camera. When 450 mW of power was applied to the device, its temperature increased over 30 °C in less than 7 minutes. The temperature of the column was extremely uniform (within 2 °C across the column) except for some localized heating near the contacts. The high thermal conductivity of the p⁺⁺ silicon served to equilibrate the temperature across the device.

In collaboration with the Professor Richard Sacks' group in the Department of Chemistry at the University of Michigan, initial separations were achieved using a stepper motor injection system that allows for injection plug widths from a few milliseconds to several seconds as needed. Reproducible sample injection plug widths allow for accurate column studies. Air was used as a carrier gas and a miniature commercial vacuum pump was used to generate the differential pressure. Detection was achieved with a commercial photo-ionization detector (PID). Separations of a four-sample mixture of acetone, benzene, toluene and m-xylene were achieved in less than 15 s using the 0.9 m column. To further facilitate coating and testing, 3 m-long columns were designed and fabricated as described in the previous section.

The 3 m columns were coated with polar and non-polar stationary phases and characterized using the system described above. Initially, crude temperature control of the columns was added through the use of a non-integrated resistive heating strip from Watlow Corporation. On more recent devices, integrated heaters and temperature sensors

located on the backside of the silicon wafer have been used to provide better uniformity and repeatability. Because the target compounds cover a wide range of volatilities, temperature programming provides a powerful tool to reduce the total analysis time of the component mixture. Figure 2.9 shows a chromatogram obtained using a single non-polar, polydimethylsiloxane-coated, 3m column. A temperature program of 58 °C to 74 °C at a rate of 9 °C/min was used in the process of separating the 16-component mixture. This reduced the separation time from 150 s (isothermal operation) to less than 75 s.

From experimental data, the number of plates, N , can be calculated as given in the following equation:

$$N = 5.545 \left(\frac{t_R}{w_{1/2}} \right)^2, \quad (2.7)$$

where $w_{1/2}$ is the width of the peak at half height and t_R is the retention time, which is the amount of time that it takes a component to travel through the channel from injection to

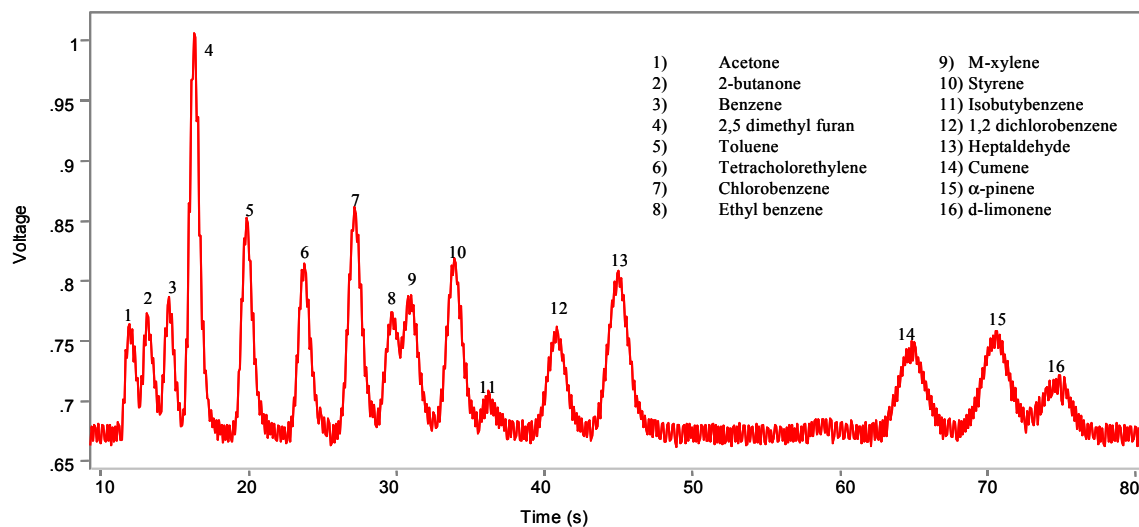


Figure 2.9: Chromatogram achieved using the 3 m column coated with a non-polar stationary phase. The injection pulse was 250 ms wide, the differential pressure was 0.5 atm, and the temperature of the column was ramped from 58 °C to 74 °C at 9 °C/min [48].

detection. Plate numbers were calculated using cumene from an isothermal separation using the same column, which yielded approximately 4900 plates for the 3m column.

More recently, through continued collaboration with Professor Richard Sacks' group, the 3m columns have achieved a world record of over 4000 plates/m and have successfully separated 30 gaseous components in less than 6 minutes as shown in Fig. 2.10 [56]. Based on the quality of the achieved separations, when a 3 m polar column is added to the system, the dual-column ensemble should have adequate resolution to separate over 40 compounds in under 10 minutes.

The fabricated pressure sensors, consisting of a 4 μm shallow boron diaphragm coated with a 2000 \AA -thick low temperature oxide layer (LTO), were tested using a DH

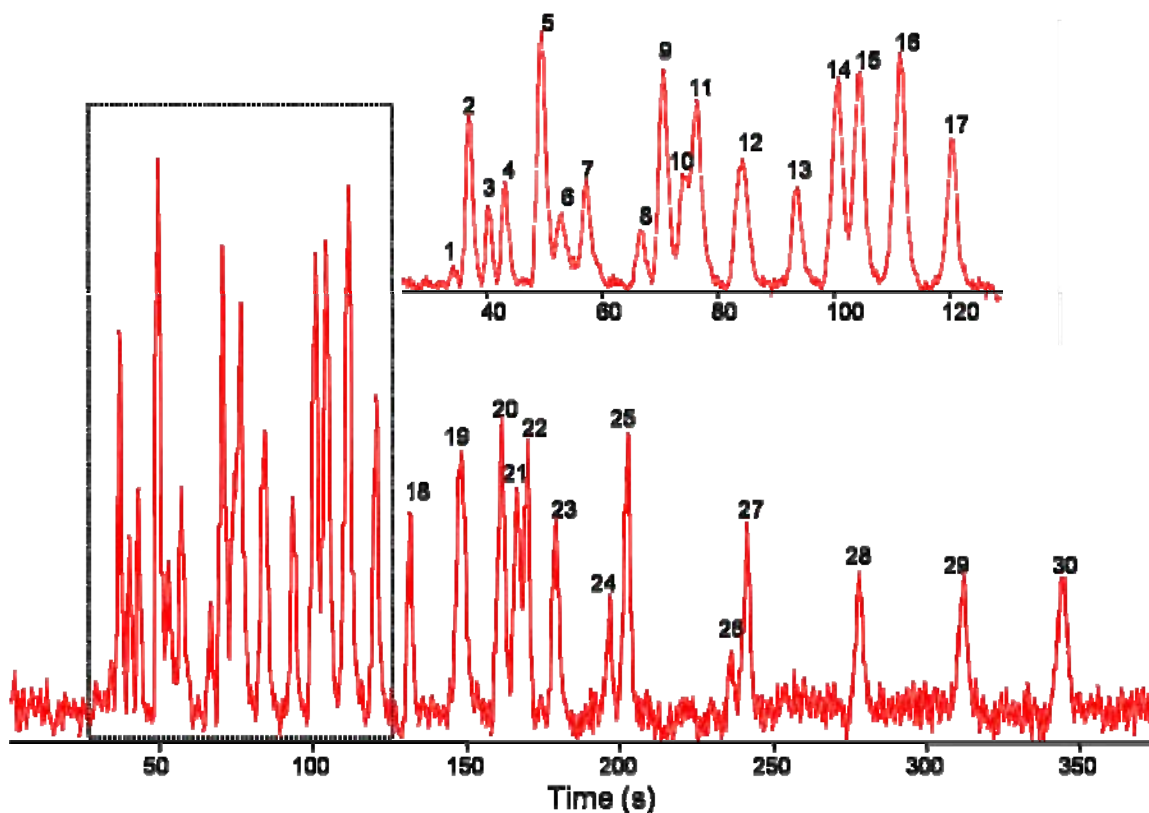


Figure 2.10: A 30 component separation achieved using the 3m column in under 6 minutes [56].

Instruments pressure controller, an HP 4284 LCR Meter and LabView®. The exterior of the sensor was subject to room pressure, and the interior was subject to pressures down to 380 torr in order to accurately simulate operating conditions. Two pressure sensor designs were tested, a bossed and unbossed version, as shown in Fig. 2.11. The unbossed version was found to be highly unstable and not accurate enough for practical use. The instability is believed to be due to the combination of stresses due to the square diaphragm and the stress gradient in the diaphragm due to the LTO and highly boron-doped silicon layers. Utilizing a low stress insulator, such as PECVD silicon oxynitride, should remedy this problem.

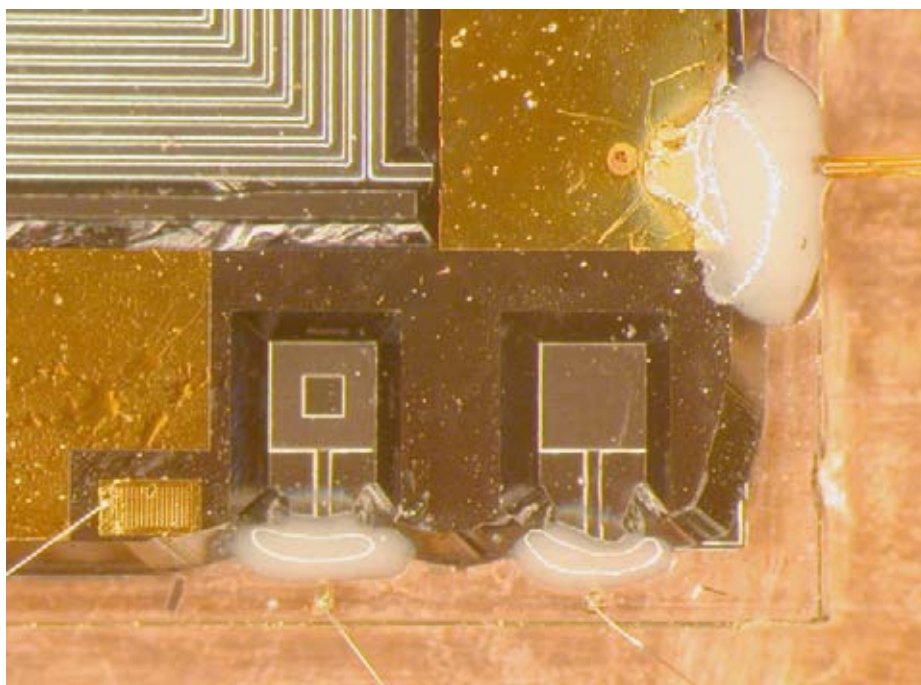


Figure 2.11: Photograph of the pressure sensors and column in the test setup.

The bossed pressure sensor performed more reliably as shown in the measured plots of capacitance versus pressure in Fig. 2.12, for the inlet and midpoint of the column, and Fig. 2.13, for the outlet. The responses in Fig. 2.12 and 2.13 have sensitivities of 7.3

fF/torr and 9.4 fF/torr, respectively. This slight deviation from the theory of Section 2.2 is most likely due to a variation in the expected diaphragm thickness. By reducing the

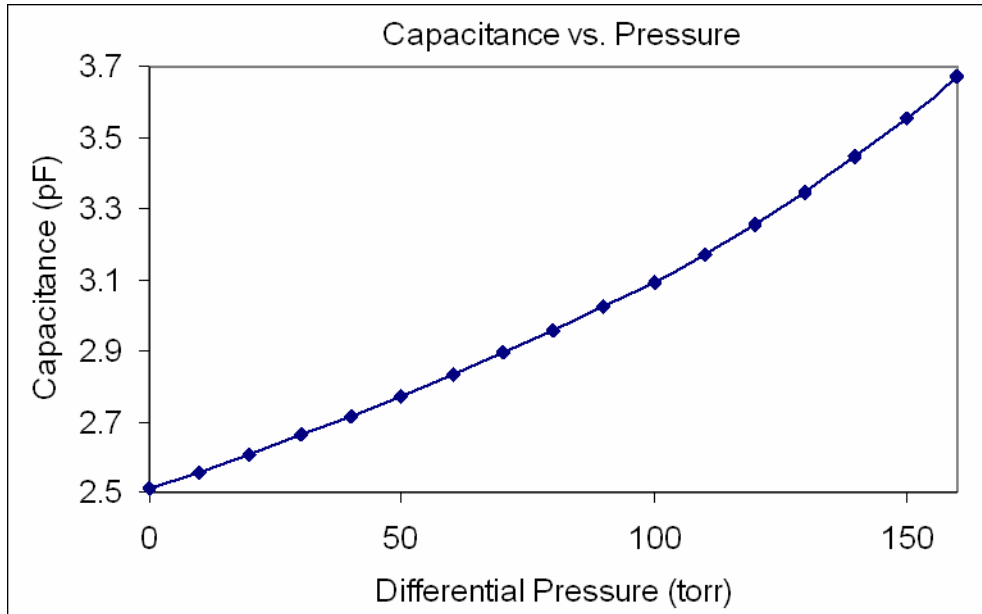


Figure 2.12: Measured capacitance versus differential pressure for the bossed pressure sensor at the inlet and midpoint of the column.

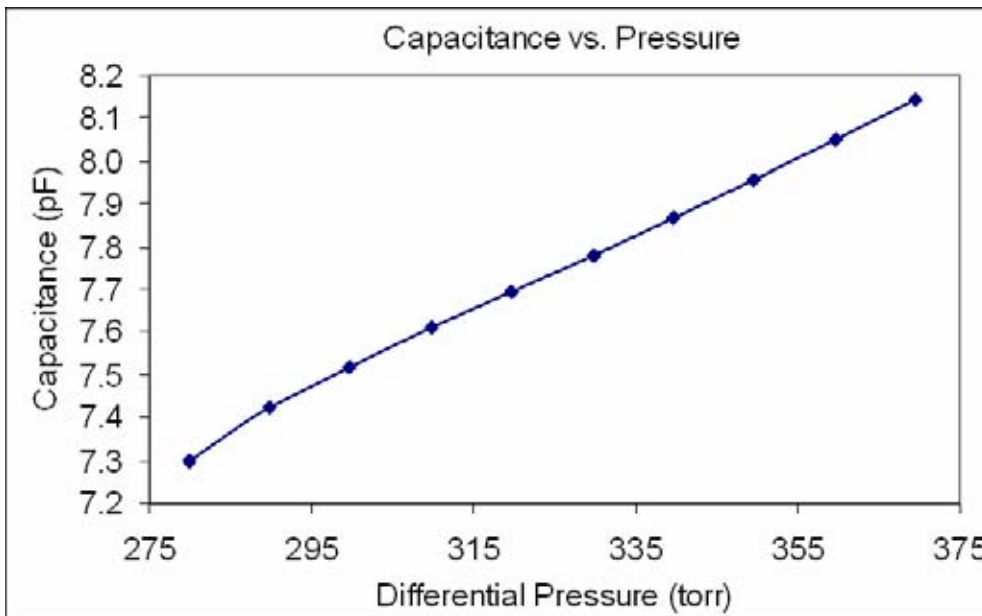


Figure 2.13: Measured capacitance versus differential pressure for the bossed pressure sensor at the outlet of the column.

theoretical thickness from 4 μm to 3.5 μm increases the sensitivity from 5.1 to 10.6 fF/torr. The age of the boron sources used for the shallow boron diffusion and/or over etching the diaphragm in EDP are possible causes for a thinner diaphragm than expected.

2.5 Integration into the Environmental Monitor

In an effort to develop a prototype version of the μGC , the 3 m column was integrated with the preconcentrator and chemiresistor sensor array, along with other non-MEMS components, on a silicon and glass electrical and fluidic substrate. This work was done in collaboration with many other WIMS faculty, staff and students and was by no means the work of the author alone. As shown in Fig. 2.14, the column was suspended to reduce power consumption, and fluidic connections were made via milled right angle

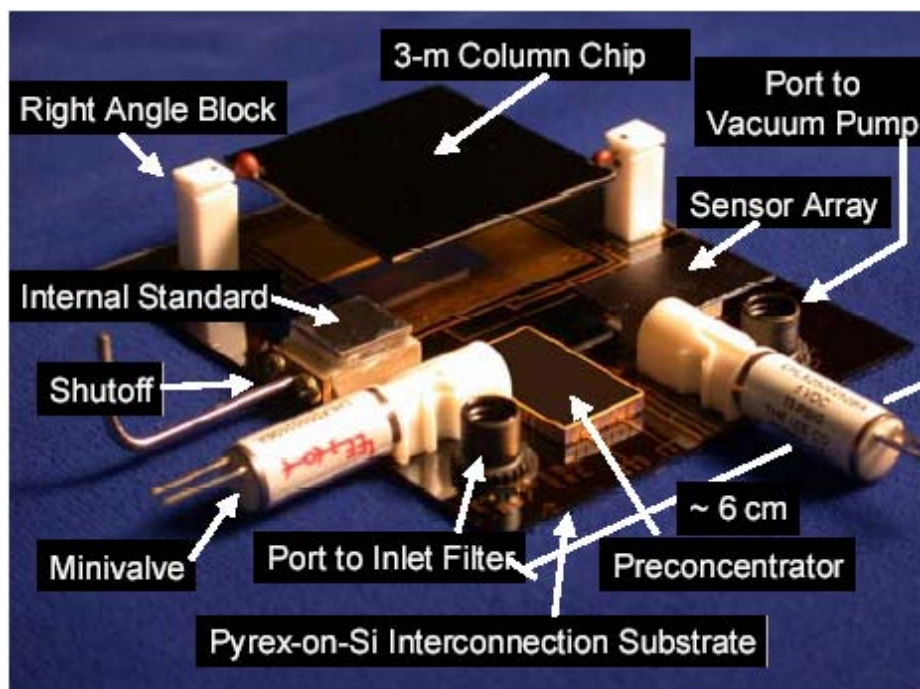


Figure 2.14: An early μGC prototype [photo courtesy of E. Gamble]

blocks. The slightly simpler version of the system (assembled and tested by Lu, et. al. [63]) was capable of separating 7 VOCs in under 35 s, as shown in Fig. 2.15. The four plots correspond to the four chemiresistor sensors in the array. The prototype, although large (~ 6 cm x 8 cm) and not fully integrated, was an important step towards the fully integrated WIMS μ GC system.

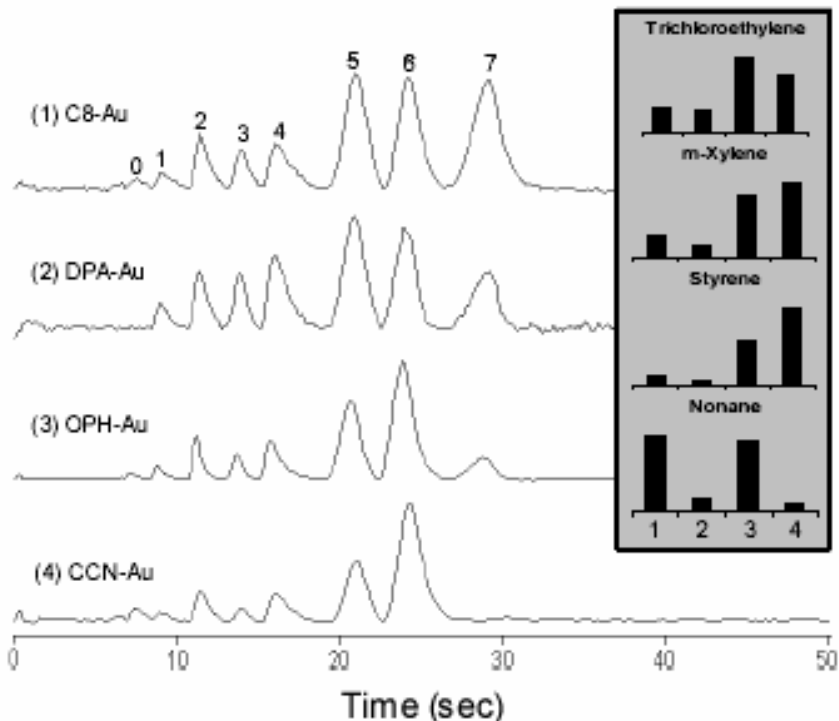


Figure 2.15: The separation of a 7-vapor mixture achieved using an early μ GC prototype [63]. The analysis was performed at 25 °C and split flow injection was employed to decrease the peak width exiting the preconcentrator. Compounds in the mixture: 0 water; 1 trichloroethylene; 2 toluene; 3 perchloroethylene; 4 n-butyl acetate; 5 m-xylene; 6 styrene; 7 n-nonane

Chapter 3

A Low Mass Silicon Micro Gas Chromatography Column

This chapter presents the theory, fabrication and results for the fastest, lowest power gas chromatography column to date. The column requires only 11 mW to raise its temperature by 100 °C in 10.4s. In addition, the column has achieved the high quality separations of 10 VOCs in 52s and four chemical warfare agent simulants and an explosive simulant in 60s. Furthermore, the column is divided into two independently temperature-programmable sections. The work in this chapter was partially presented in [51].

3.1 Motivation and Background

The silicon-glass column is robust, has a high chromatographic performance, has been thoroughly tested and experimentally verified, and has a relatively simple fabrication process. However, it is lacking in several areas. First, the structure has a large thermal mass due mainly to the glass cover plate, requiring a long time and large power to heat the device. Clearly, in a battery powered system, this is unacceptable. Although there are means to thin the glass cover plate and reduce the required power, the improvement probably does not justify the increased complexity. Second, columns with a rectangular cross section, as in the silicon-on-glass column, are inferior to columns with a circular cross section. In rectangular columns, pooling of the stationary phase may

occur in the corners resulting in increased tailing during separations and overall reduced chromatographic performance. In circular cross section columns, however, the stationary phase may not pool at all, improving performance. In addition, rectangular columns have a particular flow rate where they perform best [50]. Circular columns, however, perform well over a larger range of flow, permitting more flexibility in other system design constraints.

The silicon oxynitride (Sion) microcolumn discussed in this chapter implements improvements to provide lower power and faster operation, improved chromatographic performance, and increased system flexibility. Similar channel types have been explored in the past [64]; however, the current work is unique in that it exclusively targets and is optimized for gas chromatography, has a different column formation and structure, and is completely etched back to achieve minimum mass.

The structure of the column is shown in Figs. 3.1 and 3.2. As shown, the column will be suspended and vacuum sealed to reduce conductive and convective heat losses, etched back to improve the thermal response time, and coated with metal to decrease radiation losses and improve temperature uniformity across the column. Integrated heaters and temperature sensors are positioned in the corners of the columns to offset steady state thermal losses and in the middle of the column to improve the transient response of the device. The column structure actually consists of two individually suspended and heated columns such that the first column may be bypassed (in order to

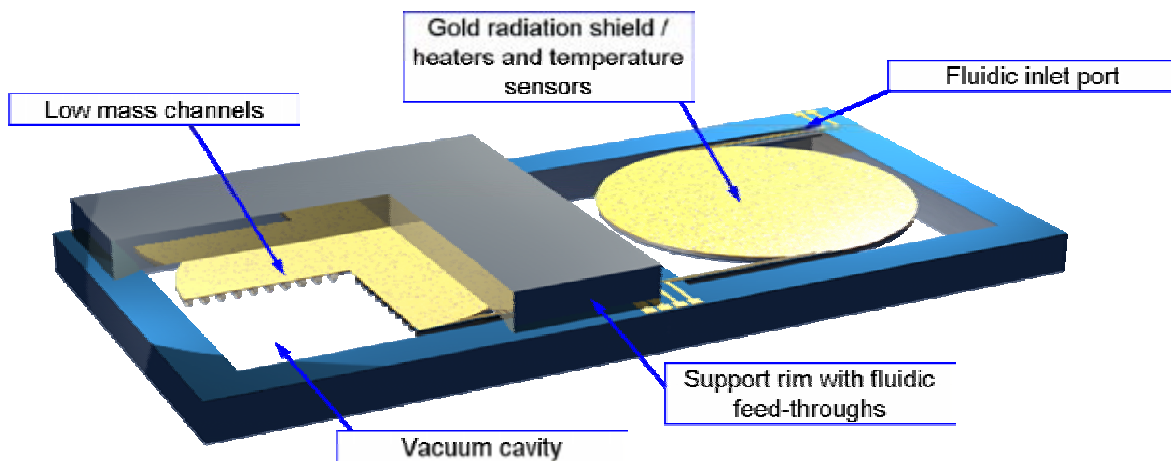


Figure 3.1: Drawing of the Sion column structure.

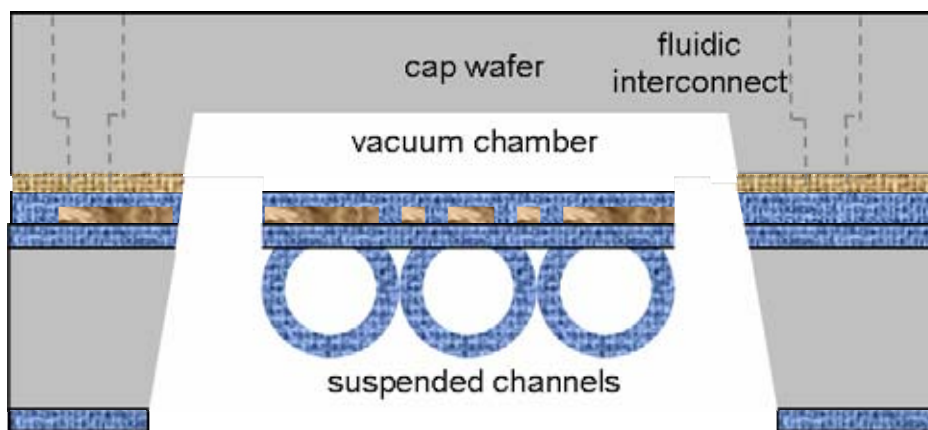


Figure 3.2: Simplified cross section of the Sion microcolumn.

increase flow in the second column) using integrated microvalves. Thus, the column has two zones that are both temperature and pressure programmable.

The remaining sections in this chapter discuss the theory, fabrication, and results of the Sion column.

3.2 System-Based Column Theory and Design

As discussed in Section 2.1 for rectangular channels, the resolving power of gas chromatography columns is measured in terms of the total number of theoretical plates (N), and their efficiency is measure by the height equivalent to a theoretical plate (H). The H of a column with a circular cross section is given by [57]:

$$H = 2 \frac{D_g}{u} + \frac{1 + 6k + 11k^2}{96(1+k)^2} \frac{ud^2}{D_g} + \frac{2h^2ku}{3D_l(1+k)^2}, \quad (3.1)$$

where D_g and D_l are the diffusion coefficients in the gas and liquid phases, respectively, k is the retention factor, h is the thickness of the liquid phase, and d is the channel diameter. The average carrier gas velocity, u , is given by Eq. 3.2 [57], where u_o is the outlet gas velocity, f_2 is the Martin-James gas compression correction factor, given in Eq. 3.3, p_o is the outlet pressure, p_i is the inlet pressure, and L is the column length.

$$u = u_o f_2 = \frac{d^2 p_o \left(\left(\frac{p_i}{p_o} \right)^2 - 1 \right)}{64\eta L} f_2 \quad (3.2)$$

$$f_2 = \frac{3 \left(\left(\frac{p_i}{p_o} \right)^2 - 1 \right)}{2 \left(\left(\frac{p_i}{p_o} \right)^3 - 1 \right)} \quad (3.3)$$

To determine the total resolving power of a column, the total number of plates, N, is calculated as

$$N = \frac{L}{H}, \quad (3.4)$$

where L is the total length of the column. Finally, the holdup time, t_m , is the time it takes for an unretained component to be injected into the system and travel through the column to the detector. It is calculated as in Eq. 3.5:

$$t_m = \frac{L}{u} \quad (3.5)$$

For the μ GC system under development, many of the same factors constrain the design of the Sion columns as did the silicon-glass columns discussed in Section 2.1. For example, an integrated MEMS vacuum pump [54] facilitates miniaturization and low power operation, but hinders the ability to increase the performance of the column by increasing the inlet pressure, as is conventionally done. In addition, using air as a carrier gas eliminates the need for gas storage, but hinders the gas flow rate and, thus, the separation. However, a low flow rate relaxes the demand on the MEMS vacuum pump, and a high flow rate is favorable in order to quickly sweep the sample off the MEMS preconcentrator. It should be noted that techniques can also be applied, such as split flow injection to improve the gas flow rate over the preconcentrator and detector. In addition, the total analysis time was limited to less than 5 min, and because of fabrication and power issues, the diameter of the low mass columns was constrained to be between 50 μm and 120 μm .

The plots shown in Figs. 3.3-3.5 were generated using Eqs. 3.1-3.5 and show the tradeoff between various design parameters. For these plots, p_i , p_o , η , k , and D_g were chosen for benzene at 50 °C and assumed to be 1 atm, 0.5 atm, 1.73×10^{-5} Ns/m², 2, and 8.0×10^{-6} m²/s, respectively. Figure 3.3 shows the column flow rate for various channel

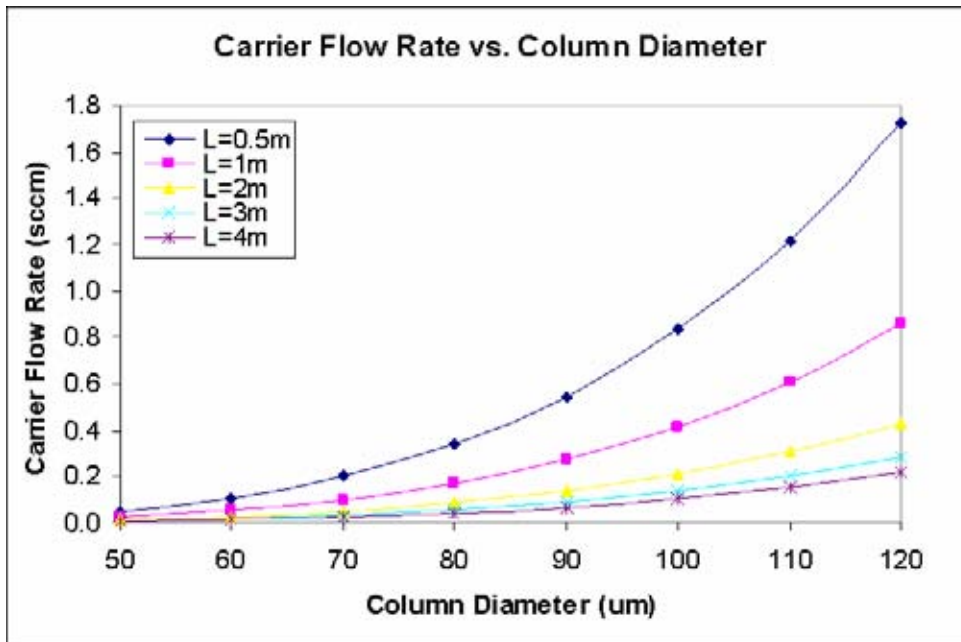


Figure 3.3: Average carrier flow rate for different column lengths versus the column diameter. An inlet and outlet pressure of 1 atm and 0.5 atm (380 torr), respectively, were assumed.

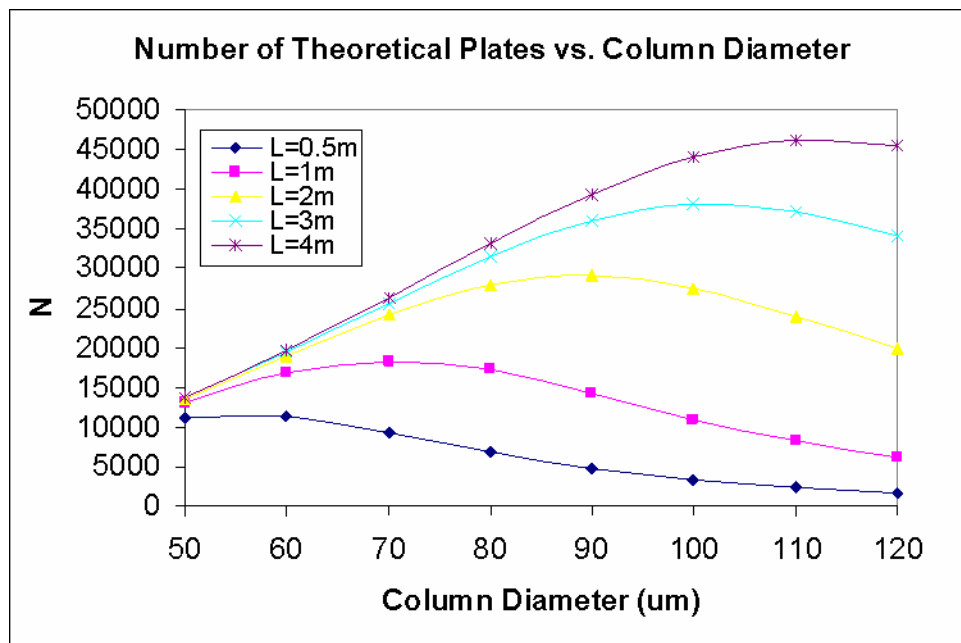


Figure 3.4: The number of theoretical plates for different column lengths versus the column diameter. An inlet and outlet pressure of 1 atm and 0.5 atm (380 torr), respectively, were assumed.

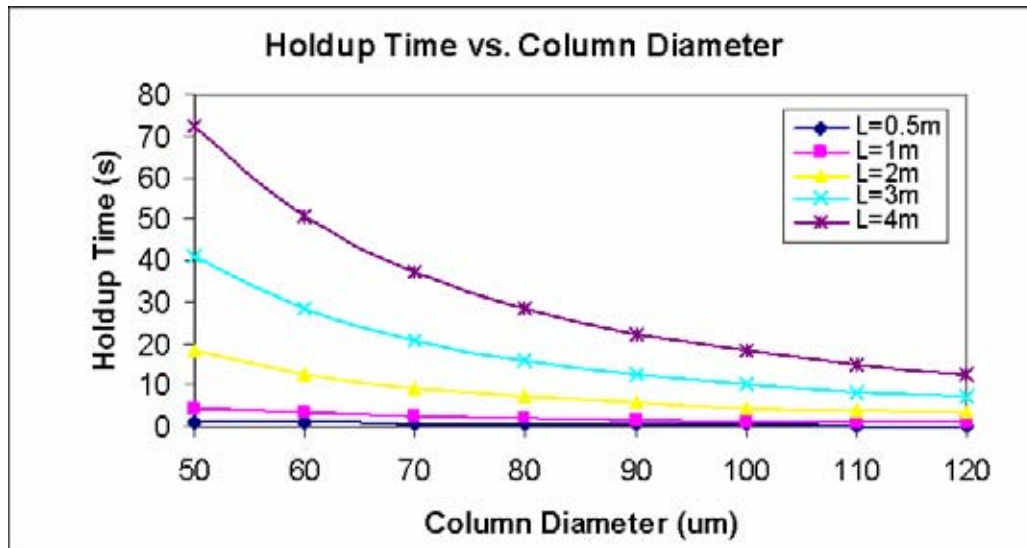


Figure 3.5: Holdup time for different column lengths versus the column diameter. An inlet and outlet pressure of 1 atm and 0.5 atm (380 torr), respectively, were assumed.

dimensions. Based on the considerations above, flow should be maximized while remaining within the requirements of the vacuum pump.

Figure 3.4 displays the relationship between the resolving power of the column and the column diameter and length. When calculating the values in this plot, the third term on the right of Eqn. 3.1 is usually small relative to the other terms and was neglected for simplicity. As can be seen in the figure, there is an optimal column diameter for each column length (for a fixed differential pressure). Based on fabrication and power considerations, it is desirable to keep the column diameter and length small. However, a high resolving power is required to be able to separation all of the components in a complex mixture of 30+ VOCs. Finally, as can be seen in Fig. 3.5, nearly all of the data points of interest correspond to a total analysis time of less than 5 min, assuming a maximum retention factor of 10. Thus, a column diameter of 80 μm and a length of 1m

were chosen as a compromise among all of the system requirements giving 16,000 theoretical plates, a flow rate of 0.2 sccm, and a holdup time of 2s.

3.3 Thermal Modeling

A thermal model of the device was developed to optimize the device speed and power and predict its behavior. The model in Fig. 3.6 and 3.7 considers the effects of conduction (through the supports and air), convection and radiation. Conduction occurs

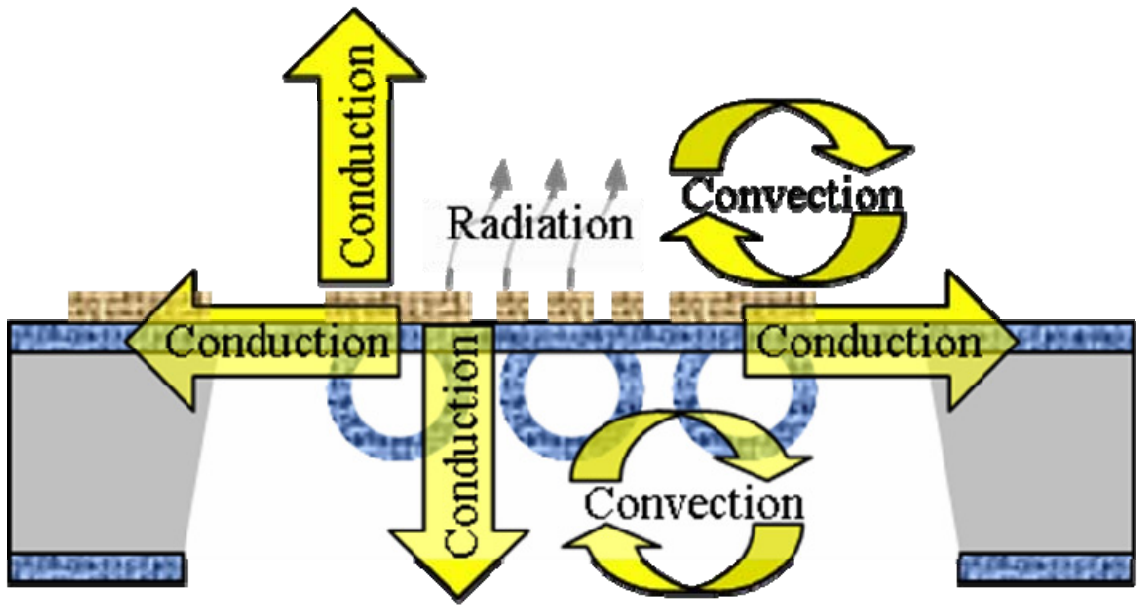


Figure 3.6: Model for thermal losses of the suspended dielectric column.

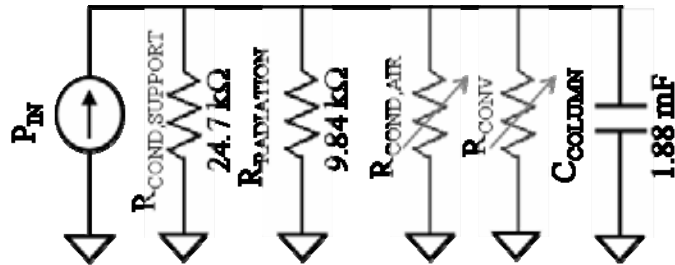


Figure 3.7: Equivalent circuit for thermal model of the suspended dielectric column. The numbers represent the values at 100 °C in vacuum; thus, losses through the surrounding air are negligible.

Table 3.1: Thermal properties of the column materials.

	Thermal Conductivity (W/m*K)	Heat Capacity (J/kg*K)	Emissivity
Oxynitride	1.4	703	-
Ti	22	523	0.12
Pt	72	130	0.05

both through the oxynitride supports and through the air above and below the column. The material thermal properties used in the theoretical calculations are shown in Table 3.1. The thermal conductivity of air between two enclosed plates is a function of pressure, approximated in [65] by:

$$k_{air} = k_{air,0} \times \frac{1}{1 + \frac{7.6 \times 10^{-5}}{P \times d / T}}, \quad (3.6)$$

where $k_{air,0}$ is the thermal conductivity of air at room temperature and pressure (0.0284 W/mK), P is the pressure, d is the distance between the plates and T is the average temperature of the plates.

Due to the transparency of the dielectric column, radiation occurs from both the column top and bottom in an enclosed space. In both cases, heat loss can be modeled as [66]:

$$Q_{rad} = \frac{\sigma_{SB} A (T_{S1}^4 - T_{S2}^4)}{\epsilon_{S1}^{-1} + \epsilon_{S2}^{-1} - 1}, \quad (3.7)$$

where σ_{SB} is the Boltzmann constant, A is the area, and T_{S1} and T_{S2} and ϵ_{S1} and ϵ_{S2} are the temperatures and emissivities of the two surfaces, respectively. In Eqn. 3.7, it is apparent that only two variables can be adjusted to reduce the power loss due to radiation at a given temperature rise. First, the area may be reduced, but this equates to reducing the column length, which the application may not permit. Second, the materials of the two surfaces can be chosen so that they minimize the radiation loss. Metals such as platinum, gold and aluminum have very low emissivities and can be used for this purpose. Also, since Eqn. 3.7 has a strong dependence on the temperature, the heat loss from the column at high temperatures will be dominated by radiation. Finally, due to the small size of the cavity, viscous forces in the air are much larger than buoyancy forces and no fluid motion occurs. Thus, the Rayleigh number is very small and convection can be neglected [67].

The plot in Fig. 3.8 was generated using Eqns. 3.6 and 3.7 and Fig. 3.7. It predicts the heat loss as a function of pressure for the column. At higher pressures, the heat loss is dominated by conduction losses through the air above and below the column. As the pressure is reduced below 5 mTorr, the heat loss of the air becomes negligible and conduction through the supports and radiation dominate. In vacuum, the model predicts a heat loss of 14 mW at a temperature rise of 100 °C and a time constant of 13s. To reduce heat loss further, the length of the supports may be increased; however, this may result in the degradation of the mechanical stability of the column. Another option is to coat the sealing cap with a low emissivity metal, such as gold, in order to minimize radiation loss. In the current work, only the column was coated with a low emissivity metal (platinum).

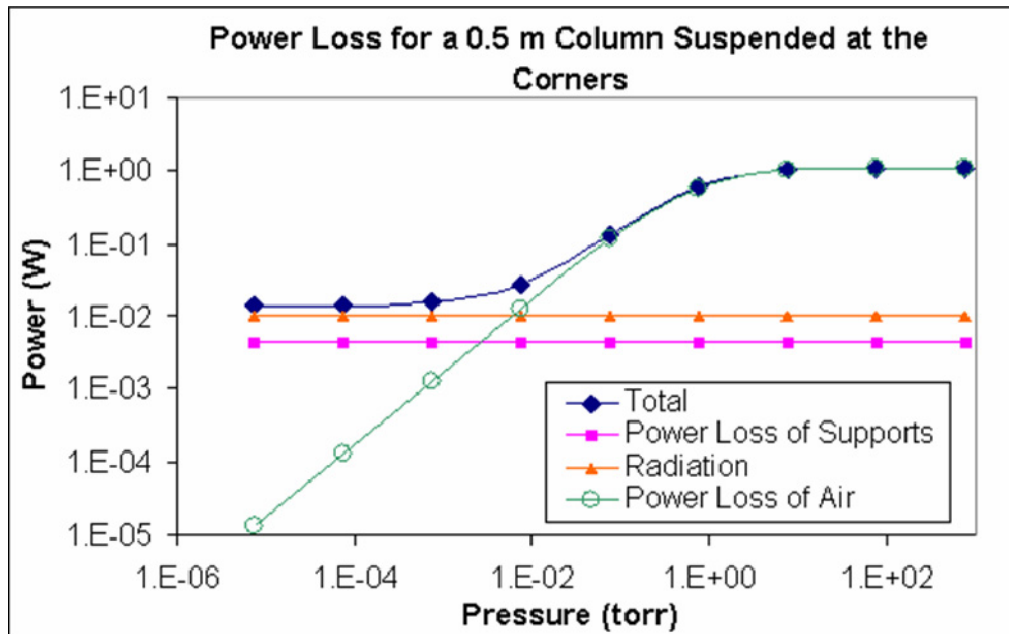


Figure 3.8: Theoretical power loss (at a 100 °C temperature rise) as a function of pressure for a 0.5 m column suspended at 2 points using the model in Fig. 3.7. The model predicts a power consumption of 14 mW in vacuum.

According to the model, this improvement would decrease radiation losses by 7 mW at 100 °C, reducing the total required power to 7 mW.

3.4 Sion Column Fabrication

Fabrication of the column (Fig. 3.9) requires 6 masks. First, a grid is anisotropically etched in a 2 μm-thick PECVD oxynitride dielectric layer using dry oxide etch at a pressure of 15 mTorr in a PlasmaTherm RIE tool. A vertical sidewall is necessary in order to prevent voids when the channel is later sealed and, thus, improve the strength of the column; thus, the etch was performed at a low pressure. The grid is then undercut using a 25 minute-long dry isotropic etch and sealed using a 12 μm-thick PECVD oxynitride layer (Fig. 3.10). Both oxynitride layers are designed to be stress

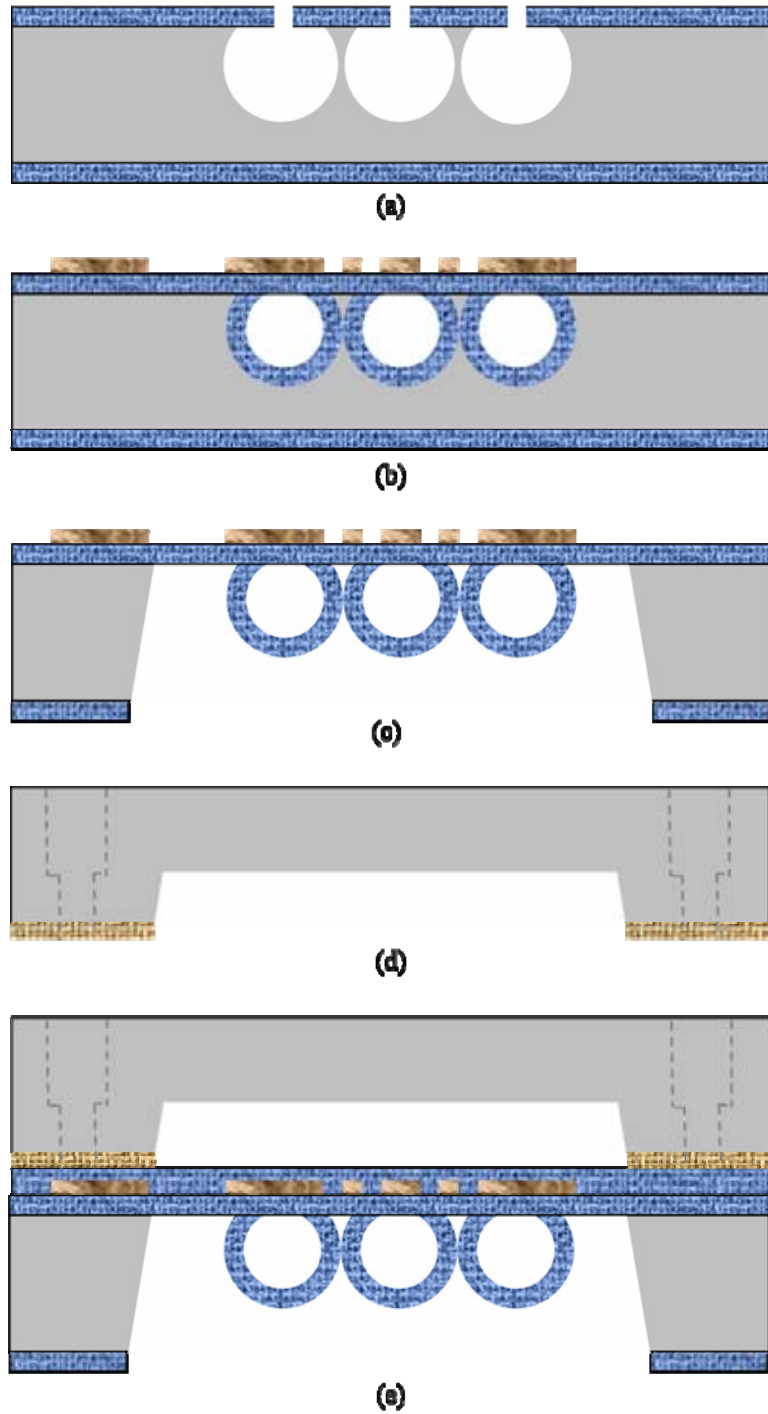


Figure 3.9: Process flow for the low mass microcolumns. The column is formed from a released stress free PECVD dielectric layer with Ti/Pt heaters. Stress minimization of both the dielectric layer and the metal layer is critical for release. Au-Si eutectic formation bonds the two wafers together.

free and require less than 15 min for deposition. Process parameters for the oxynitride film and dry etch are shown in Tables 2 and 3.

Next, a 200/200 Å Ti/Pt metal layer is deposited and patterned to form the heaters and temperature sensors. The Ti/Pt layer is also used to reduce radiation losses and increase temperature uniformity across the column. Next, the Ti/Pt layer is protected with another 2µm-thick oxynitride layer and then the oxynitride is wet etched in BHF for device isolation and to open metal contacts. Finally, a 300/1000/5000Å Ti/Pt/Au bonding ring is deposited via evaporation. The intermediate platinum layer serves as a diffusion barrier during the later bonding step.

The cap wafer requires 3 additional masks. Two DRIE etches form a recess and

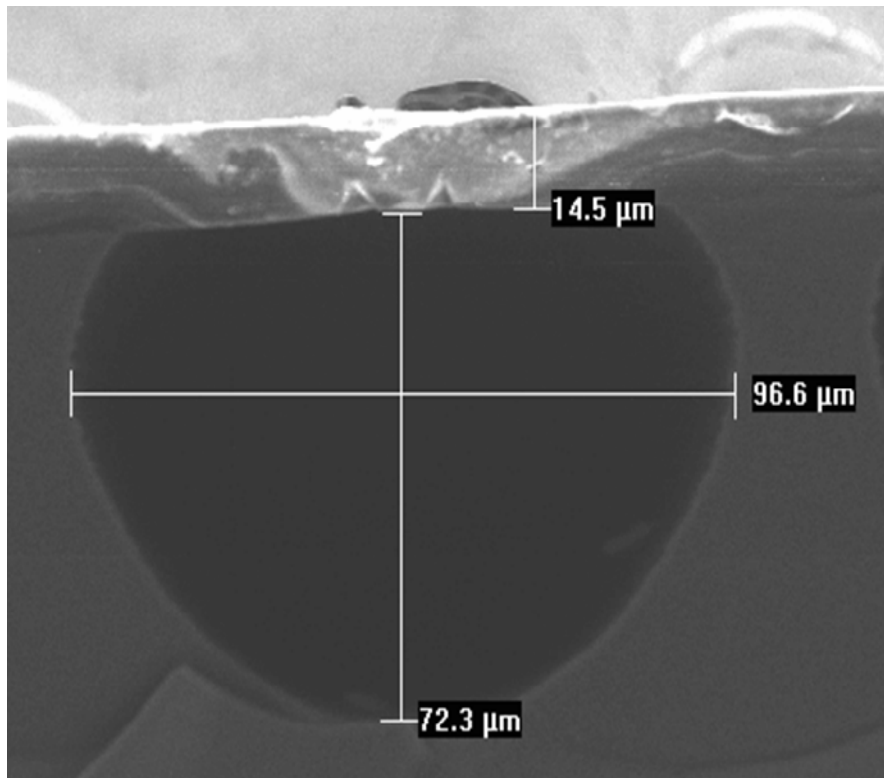


Figure 3.10: Cross section of a sealed buried channel with a height of 72µm, width of 97µm, and ceiling thickness of 15µm.

Table 3.2: GSI PECVD process parameters for the stress free oxynitride structural film.

Parameter	Value
N ₂ :SiH ₄ :NH ₃ :N ₂ O (sccm)	0:45:10:1980
HF:LF Power (W)	300:0
Temperature (°C)	400
Pressure (torr)	3
Deposition Rate (Å/min)	9200
Stress (MPa)	~ 0
BHF Etch Rate (Å/min)	3900
Refractive Index	1.50

Table 3.3: STS ICP Etcher process parameters for the dry, isotropic channel etch.

Parameter	Value
SF ₆ :Ar:CF ₄ (sccm)	260:5:0
Coil:Platen Power (W)	800:60
Aperture (%)	50
Oxynitride Etch Rate (Å/min)	~200

low-dead-volume fluidic connectors, and a 300Å/4µm Cr/Au bond ring is plated. Finally, the two wafers are bonded together utilizing Si/Au eutectic formation, and a dry STS etch is used to release the device. Figure 3.11 shows the column just before release. Figures 3.12, 3.13, and 3.14 display SEMs and photographs of the released column. Stress minimization of both the metal and oxynitride films is critical to device release. In addition, low-dead-volume fluidic interconnects are crucial in preventing band broadening. It should be noted that the structure in Fig. 3.9(e) contains a dielectric layer

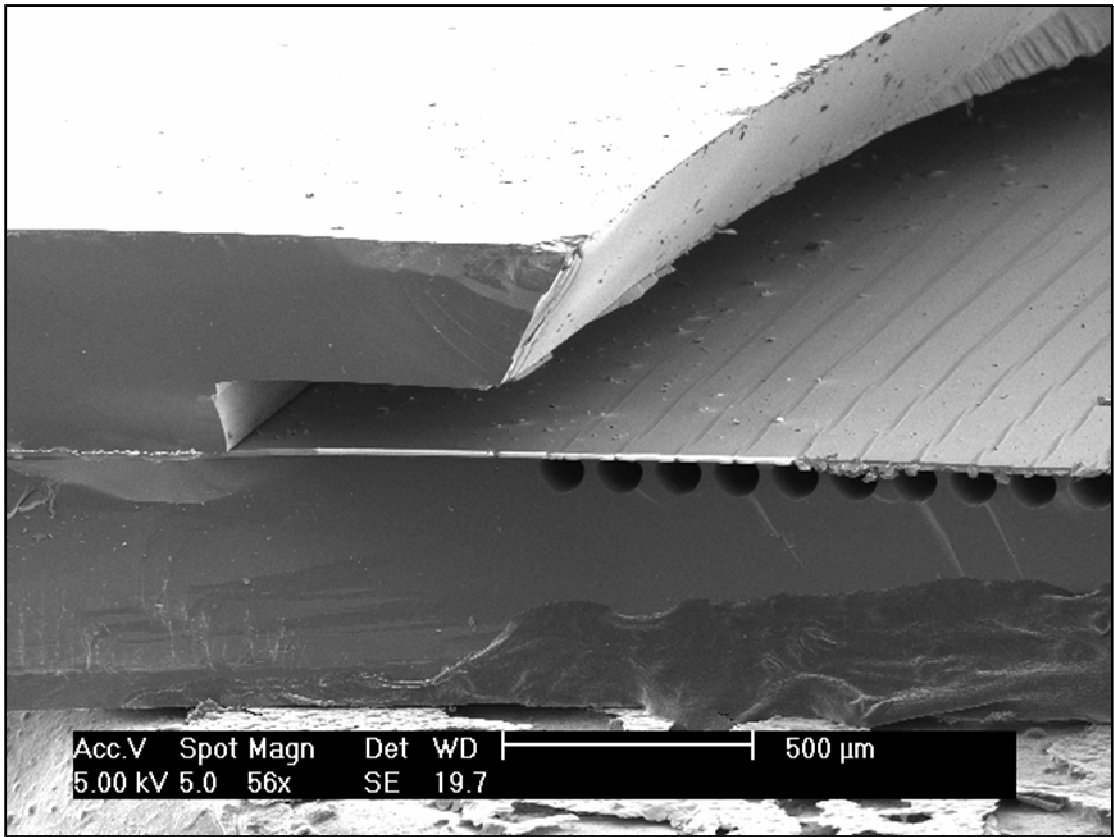


Figure 3.11: SEM of a side view of the broken column just before release. The Au-Si eutectic bond is visible in the middle left of the picture, where the two wafers come into contact.

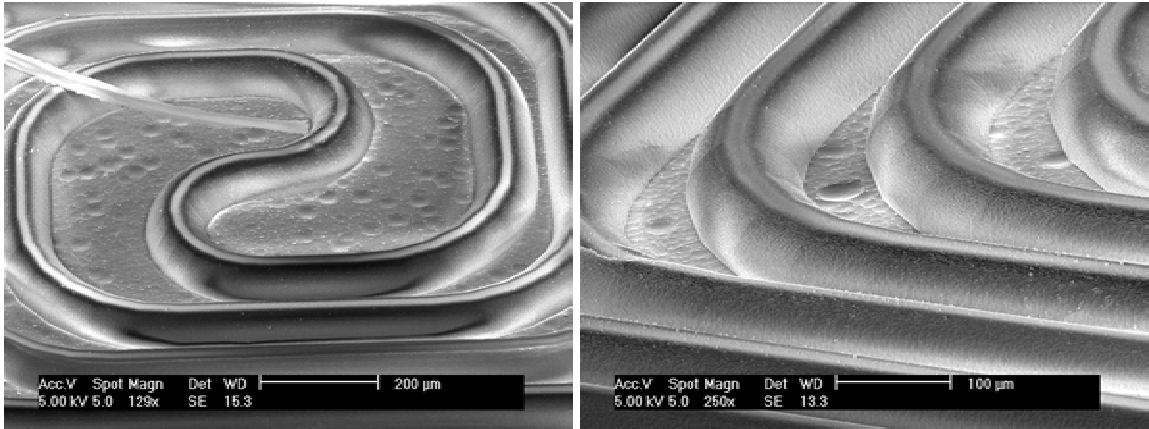


Figure 3.12: SEMs of the bottom side of the released dielectric column.

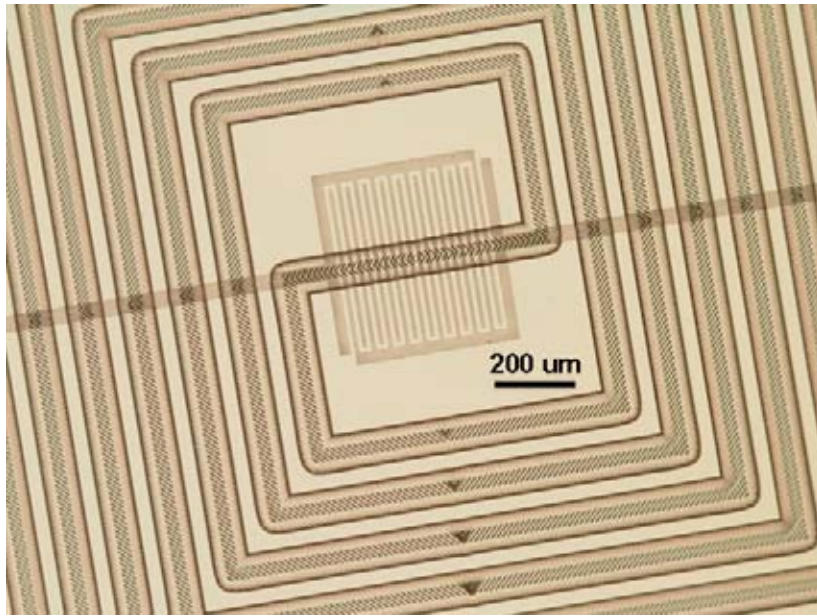


Figure 3.13: Picture of the center heater and channels, looking through the bottom side of the transparent column.

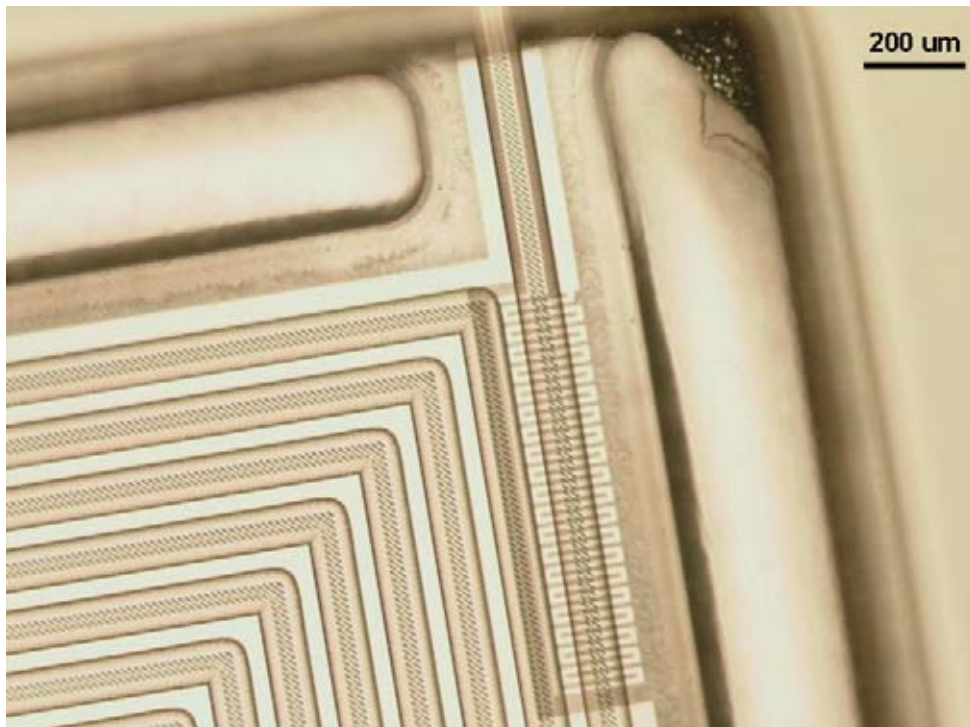


Figure 3.14: Picture of the side heater and suspended inlet, looking through the bottom side of the transparent column.

connecting the column to the substrate. This layer is used for structural support; however, it may optionally be etched away to fully suspend the device and reduce its power consumption as was done in this work. The process can also be extended by bonding a second cap wafer to the bottom of the device, thus, vacuum encapsulating the column.

3.5 Sion Column Testing and Results

A fabricated 1m (2 x 0.5m) column is shown in Fig. 3.15. The three low-dead-volume fluidic interconnections are visible on the top substrate and permit individual

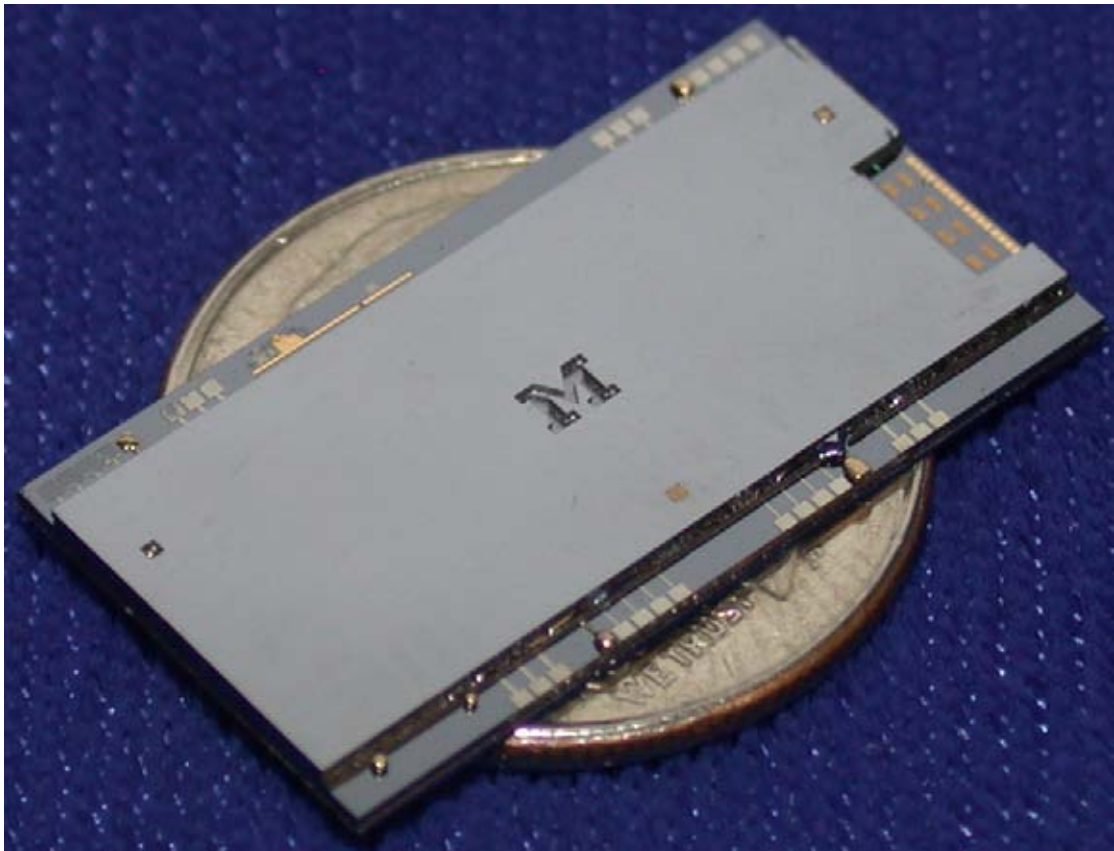


Figure 3.15: Picture of the finished column on a dime. The three ports can be seen in the upper left, bottom middle and upper right of the die. The integrated sensor array is on the right.

coating of the two column segments and pressure programming. The electrical interconnects can be seen on the shelf along the bottom of the column and provide contacts to the heaters, temperature sensors and substrate.

After fabrication, initial tests were done to examine the strength of the eutectic bond and its hermeticity. First, a gross bond strength test was completed by prying apart the two wafers using a razor blade. The bond area was extremely hard to break, and when it did, the breaking occurred in the substrate and not along the bond interface. Next, capillary tubing was epoxied into the fluidic connectors and fluidic pressure of up to 0.5atm was applied to the input. The device was immersed in acetone and no leaks were visible, verifying the gross hermeticity of the bond and viability of the fluidic interconnections. Complete characterization of a similar bond technology can be found elsewhere [68]. The current bond technology differs from [68] in that it utilizes metal feedthroughs and a PECVD isolation layer.

Next, the device was placed in an environmental oven and the temperature was varied from 25 °C to 125 °C. The resistances of the temperature sensors were found to have a mean resistance of 16.8 k Ω and a TCR of 431 ppm/°C. The devices were then placed in a custom pressure-control chamber capable of pressures between atmosphere and 10 μ Torr. Power was applied to a single heater in a fully suspended column and the curve in Fig. 3.16 was obtained. Less than 6 mW was required to raise the local column temperature by 100°C. Next, the pressure in the chamber was varied and the power required to achieve a 100°C temperature rise was measured as shown in Fig. 3.17. The power required in vacuum and the pressure where the power begins to increase (\sim 5 mTorr) closely match that of the theoretical graph of Fig. 3.8. The variation between the

theoretical graph and measured graph is due to temperature non-uniformity at higher pressures. That is, the theoretical calculations assume a uniform temperature across the

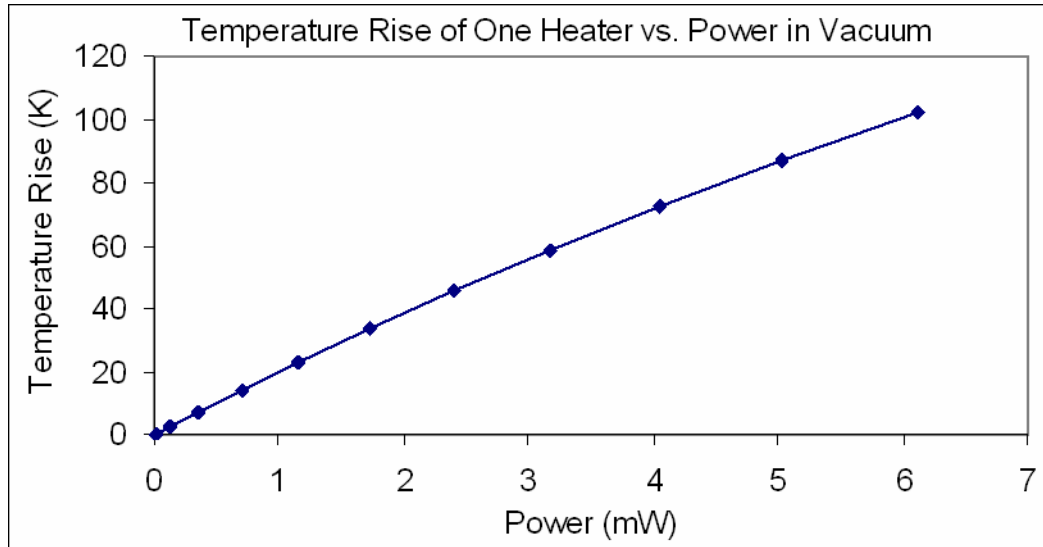


Figure 3.16: Measured steady-state temperature versus power data for a single heater in the suspended column.

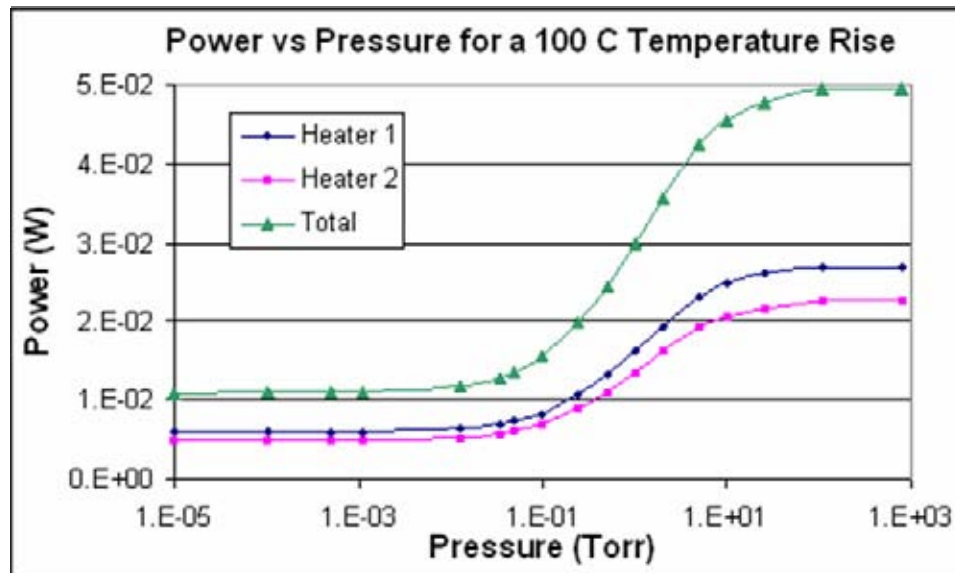


Figure 3.17: Measured power loss of the column versus pressure. The deviation from the theoretical graph is due to temperature non-uniformity at higher pressures. The power required in vacuum represents over a 5X improvement in power over previously published devices.

column at high pressures, but the current column was designed only to be uniform at low pressures.

Next, the transient response of the column was measured as shown in Fig. 3.18 and Table 3.44. The local column temperature requires a rise and fall time of 2.6 and 2.8 seconds, while the column center requires 10.4 and 11.8 s (while energizing both corner heaters). This results in a natural temperature ramp rate of 580 °C/min. It should be noted that better uniformity and a faster response may be achieved by activating the center heater in addition to the corners. Using this approach, temperature ramp rates of at

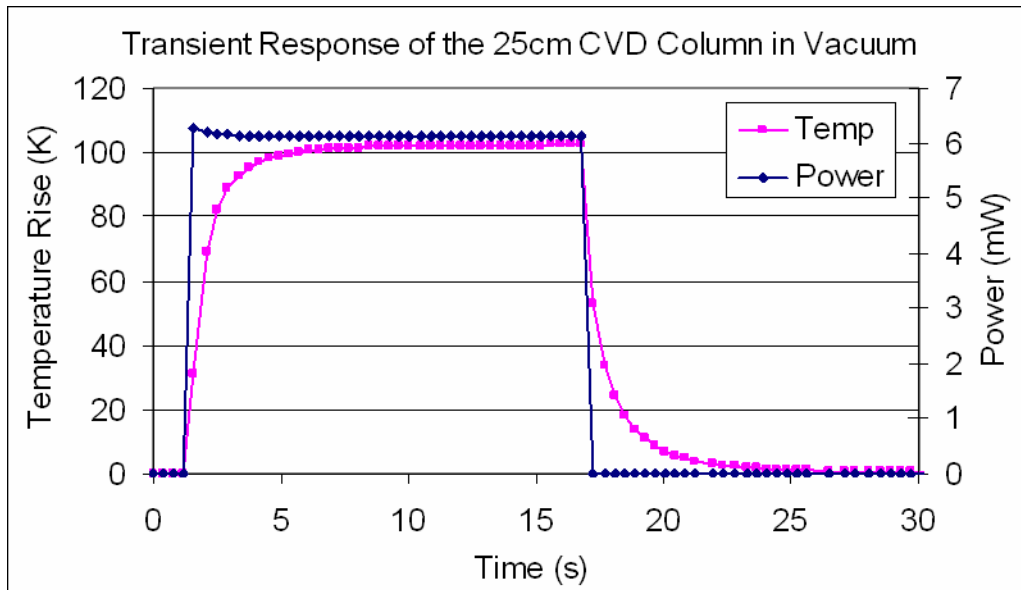


Figure 3.18: Measured transient response of one of the heaters in the column.

Table 3.4: Measured response time of the corner and center of the column while actuating the corner heaters. This represents a 4X improvement in speed over previously published devices.

	Column Corner	Column Center
Rise Time (s)	2.6	10.4
Fall Time (s)	2.8	11.8

least 5800 °C/min should be possible with a short power pulse of 55 mW followed by operation at 11 mW.

The devices were then coated with a PDMS stationary phase. During coating, the devices withstand an inlet pressure of 25 psi without damage. Next, the device was hooked up to an injection system and flame ionization detector (FID). The separation of 10 alkanes in 52s is shown in Fig. 3.19. The separation of four chemical warfare agent simulants and an explosive simulant in 60s is shown in Fig. 3.20. Both separations utilized a temperature ramp from of 30 to 100 °C at 50 °C/min and demonstrate the high chromatographic performance of the column as well as its versatility.

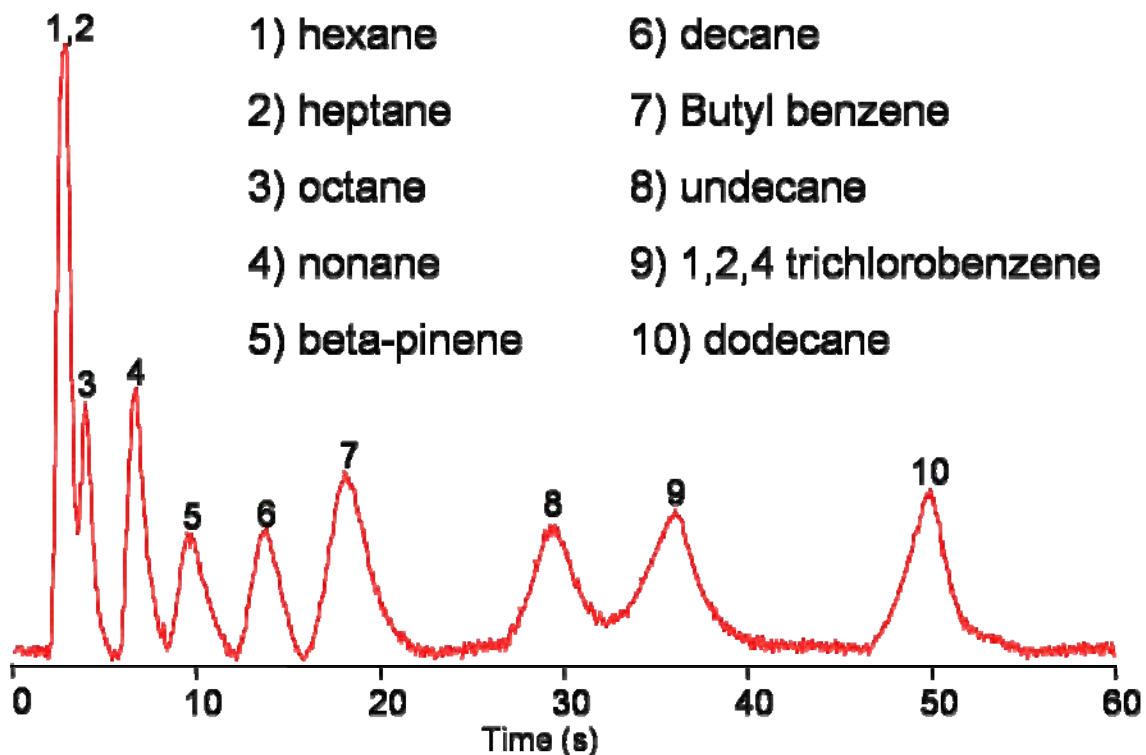


Figure 3.19: Separation 10 components in 52s using the 1 m column. A temperature program of 30-100 °C at 50 °C/min was used in conjunction with a flame ionization detector.

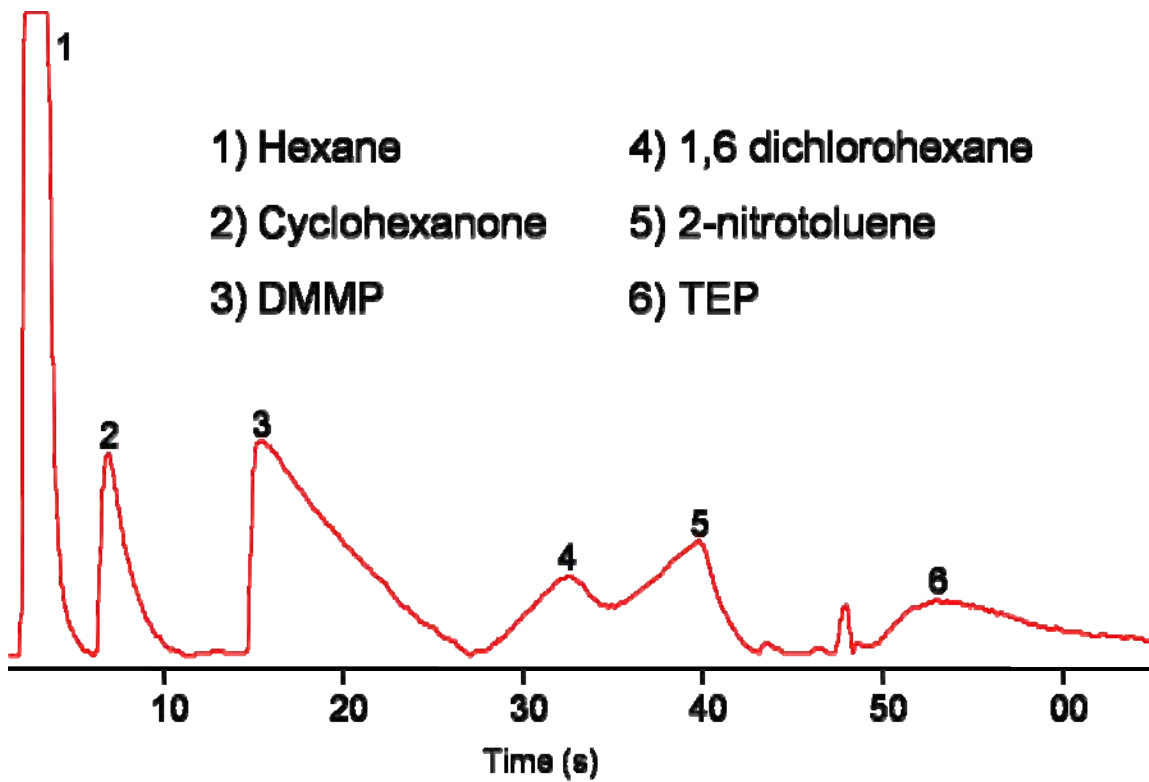


Figure 3.20: Separation of four CWA simulants and an explosive simulant in 60s utilizing the 1 m column. A temperature program of 30-100 °C at 50 °C/min was used in conjunction with a flame ionization detector.

Chapter 4

A Hybrid Thermopneumatic and Electrostatic Microvalve with Closed-Loop Position Sensing

This chapter presents a low power, hybrid thermopneumatic and electrostatic microvalve that enables pressure programming of the columns; it is believed to be the first device of its kind. The 7.5 mm x 10.3 mm valve has an open flow rate of 8 sccm at 4.6 torr, a leak rate of 1.3×10^{-3} sccm at 860 torr, a closed-to-open fluidic resistance ratio greater than one million, an actuation time of 430 ms, a required hold power of 60 mW while closed. In addition, the valve requires no power to open, 108 mJ to close, and has a built in position sensor with a sensitivity of 1.3 fF/torr. With minor improvements, the valve requires 35 mJ to close in 140 ms, a hold power of 6 mW without the electrostatic latch, and no hold power with an electrostatic voltage of 180V. The work presented in this chapter was partially presented in [55]. The following sections present the design, theory, fabrication and results for the microvalve. The background was presented in Section 1.5.

4.1 Device Concept

Using a hybrid thermopneumatic and electrostatic actuation scheme, the high force and large throw characteristics of thermopneumatic actuators are preserved, while the electrostatic hold reduces the power/energy requirement of the device. Furthermore, this combination may solve the problem of particulate contamination of electrostatic devices since the device is already closed when the electrostatic voltage is applied. It will also be shown that this combination significantly improves the response time compared to a stand alone thermopneumatic actuator. This work builds on previous work at Michigan on electrostatic actuators [69] and phase-change actuation [70]. The structure of the normally-open valve improves on the power and speed performance of a previous microvalve [43]. It is being developed to enable pressure tuning of the columns and flow control in the WIMS μ GC system.

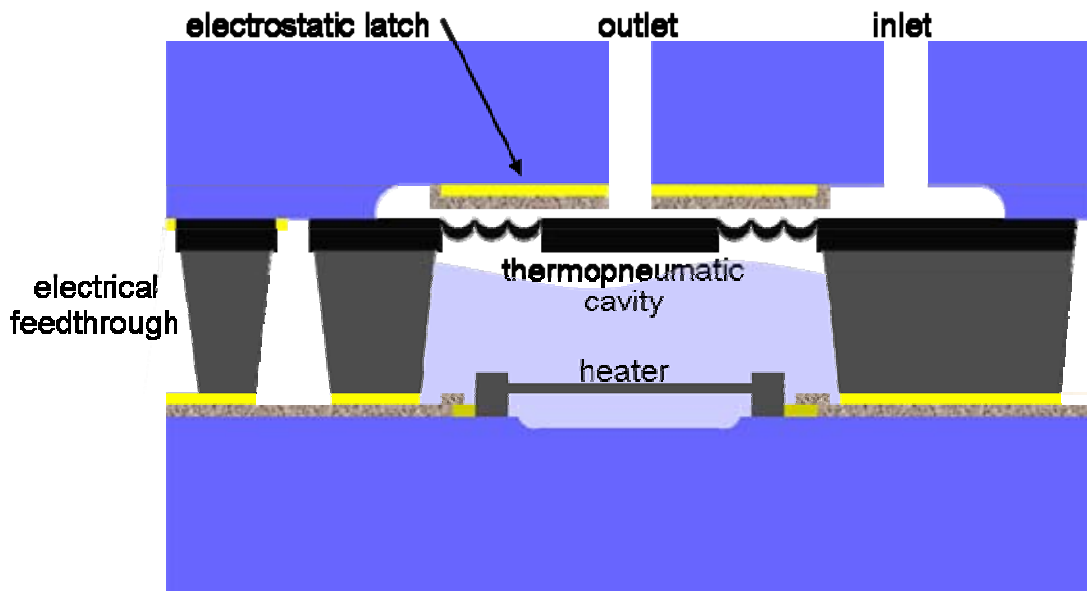


Figure 4.1: Drawing which displays the main components of the microvalve.

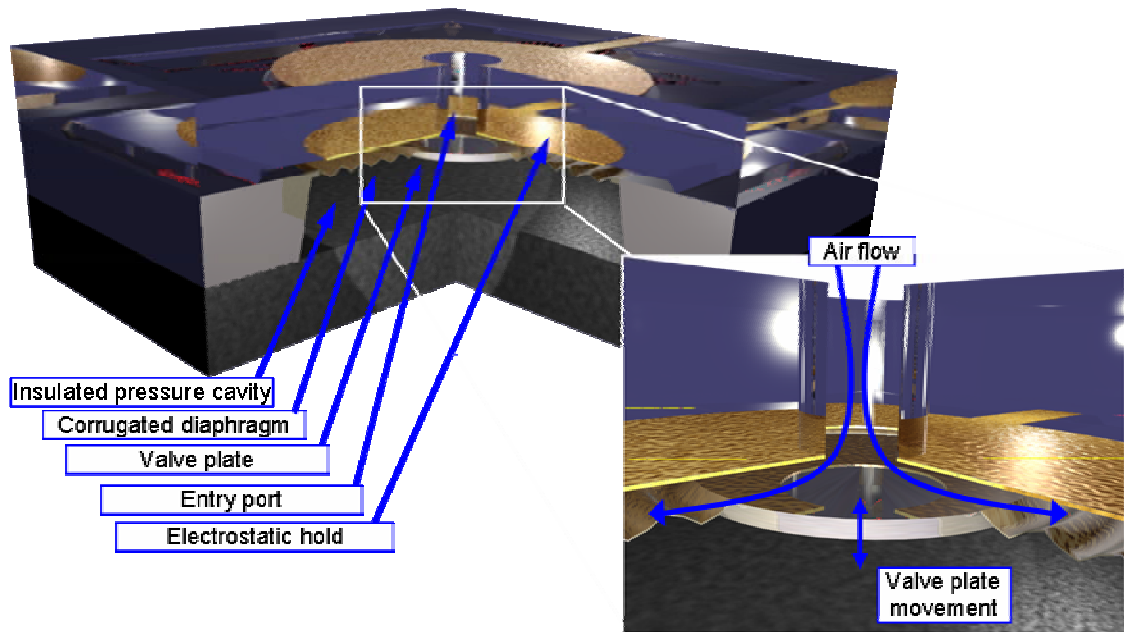


Figure 4.2: 3D drawing of the microvalve.

The overall structure of the normally open valve is shown in Figs. 4.1 and 4.2. To close the device, an elevated heater grid energizes a working fluid, raising the pressure in the cavity and deflecting the corrugated diaphragm and valve seat. The heater is suspended in order to increase its heating efficiency and the corrugations serve to decrease the spring constant of the diaphragm, permitting valve travel greater than 30 μm . The capacitive pressure sensor reads out the cavity pressure and valve seat position and provides feedback to determine when to enable the electrostatic actuator. Once latched, the power to the heater can be reduced or eliminated and, thus, ideally, the valve only requires power to transition from open to closed and consumes no static power. In addition, hybrid actuation may help alleviate the particulate problem common to electrostatic actuators because, in this case, the electrostatic voltage is only applied after the device is closed and thus charged particles are not likely to be trapped on the sealing surface.

4.2 Design and Analysis

For the current valve which will be integrated into the WIMS μ GC system, there are several important performance metrics and requirements, including the speed, power, clearance, leak rate and open flow rate. Tradeoffs exist among many of them as discussed in the rest of this section.

4.2.1 Diaphragm Deflection Theory

The diaphragm and valve plate are the moving components of the valve and their position determines the flow rate through the valve and the valve state (open or closed). Thus, the design of the diaphragm is important to the overall performance of the device. For the current device, an etched back p++ silicon layer was chosen as the diaphragm structural material due to its robustness and proven performance. In addition, the diaphragm was corrugated in order to reduce its spring constant. The equation governing the deflection of bossed, corrugated diaphragms was estimated in [71], [72], and [73] and an approximation is given in Eqn. 4.1.

$$\frac{PR^4}{E'h^4} = A_P N_P \frac{y}{h} + B_P N_P \frac{y^3}{h^3} \quad (4.1)$$

In this equation, P is the pressure, R is the diaphragm radius, y is the deflection of the valve plate and h is the thickness of the diaphragm. E' , A_P , B_P , N_P are defined as:

$$E' = \frac{E}{1-\nu^2}, \quad (4.2)$$

$$A_p = \frac{2(q+3)(q+1)}{3\left(1 - \frac{v^2}{q^2}\right)}, \quad (4.3)$$

$$B_p = \frac{165(q+1)^3(q+3)}{q^2(q+4)(q+11)(2q+1)(3q+5)}, \quad (4.4)$$

$$\frac{1}{N_p} = (1-r^4) \left(1 - \frac{8qr^4(1-r^{q-1})(1-r^{q-3})}{(q-1)(q-3)(1-r^{2q})} \right), \quad (4.5)$$

where E and ν are the Young's Modulus and Poisson's Ratio of the diaphragm material. q is the corrugation quality factor and for shallow, sinusoidal profiles is given by:

$$q = 1 + 1.5 \frac{H^2}{h^2}, \quad (4.6)$$

where H is the corrugation depth. In these equations, the initial stress of the diaphragm is ignored, but can be added as a term to the right side of Eqn. 4.1 [71]. Equations 4.1 through 4.6 were combined to yield the graph in Fig. 4.3. An outer radius of 750 μm , boss radius of 475 μm , and 4.2 μm corrugation depth were chosen for the device dimensions based on previous research and process issues. Also, a Young's Modulus and Poisson's ratio of 125 GPa and 0.17, respectively, were assumed for boron-doped silicon [74].

From Fig. 4.3, it is apparent that there is an initial period where a small increase in differential pressure yields a large deflection. For valves with low flow rate requirements, it would be advantageous to operate in this regime. After the initial period, each increase in deflection requires a larger increase in differential pressure. Figure 4.3 also shows the large impact that the diaphragm thickness has on its response. By decreasing the thickness from 4.2 to 3 μm , the required pressure to achieve a 38 μm

deflection is reduced from 1570 torr to 770 torr. This difference in the spring constant of the device will impact the rest of the valve, especially its thermopneumatic actuator.

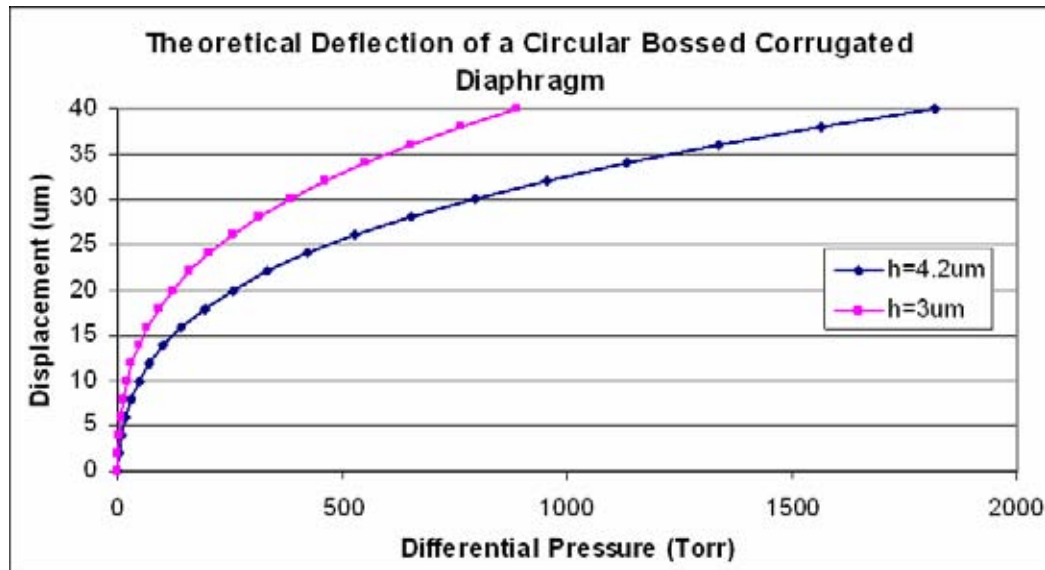


Figure 4.3: The theoretical deflection of the valve diaphragm. The two curves show the impact of the diaphragm thickness on the diaphragm's response.

4.2.2 Thermopneumatic Theory

At the heart of the microvalve is the thermopneumatic drive; its design impacts the rest of the valve. Using previous experimental data [43], a first order thermal model of the actuation cavity was derived as shown in Fig. 4.4. R_L and C_L are the thermal resistance and capacitance of the working fluid and R_S and C_S are the thermal resistance and capacitance of the silicon and glass substrates, in addition to the surface the valve is mounted on. This model makes several assumptions, all of which have been shown to be valid in [43]. First, the model assumes efficient heating; the heat lost through the support posts of the heater is negligible and that all of the energy is generated in the grid itself. The former can be accomplished by minimizing the cross-sectional area

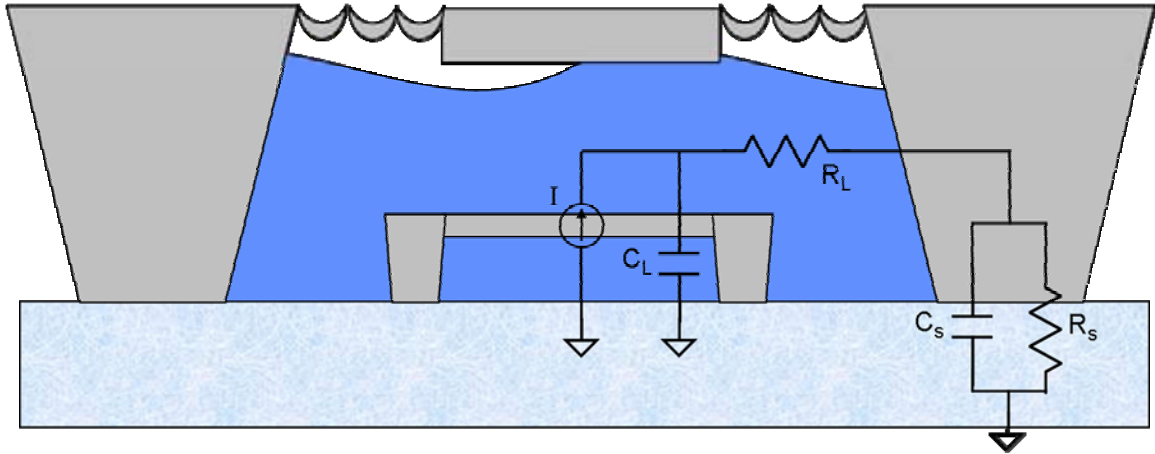


Figure 4.4: First order thermal circuit for thermopneumatic actuator.

Table 4.1: Thermal properties of the relevant valve materials.

	σ (W/m*K)	c (J/kg*K)	ρ (kg/m ³)
Working Fluid (Pentane)	0.112	2309	626
Silicon	148	712	2230
Pyrex	1.4	835	2250
FR4 PCB	0.3	-	-

of the heater and the latter through the use of low resistance leads. Second, the model assumes that conduction is the main source for heat loss in the system. Thus, the effects of convection and radiation have been ignored, as justified in the experimental data in [43].

Table 4.2 lists the thermal properties of the relevant materials and the thermal resistances were calculated using Eqns. 4.7 and 4.8. L , A , and V are the length, area and the volume of the material and are given in the direction of heat transfer. σ is the thermal conductivity of the material, c is its heat capacity and ρ is its density.

$$R_{TH} = \frac{L}{A \times \sigma}, \quad (4.7)$$

$$C_{TH} = c \times V \times \rho, \quad (4.8)$$

The calculations result in $R_L=158$ K/W, $C_L=5.7 \times 10^{-4}$ J/K, $R_S=71$ K/W, and $C_S=0.16$ J/K. R_L was calculated assuming that the working fluid fills 20% of the actuation cavity; it is dominated by losses through the working fluid directly below the heater grid. R_S includes the resistance of the substrate in addition to the resistance of the PCB board that the device is mounted on.

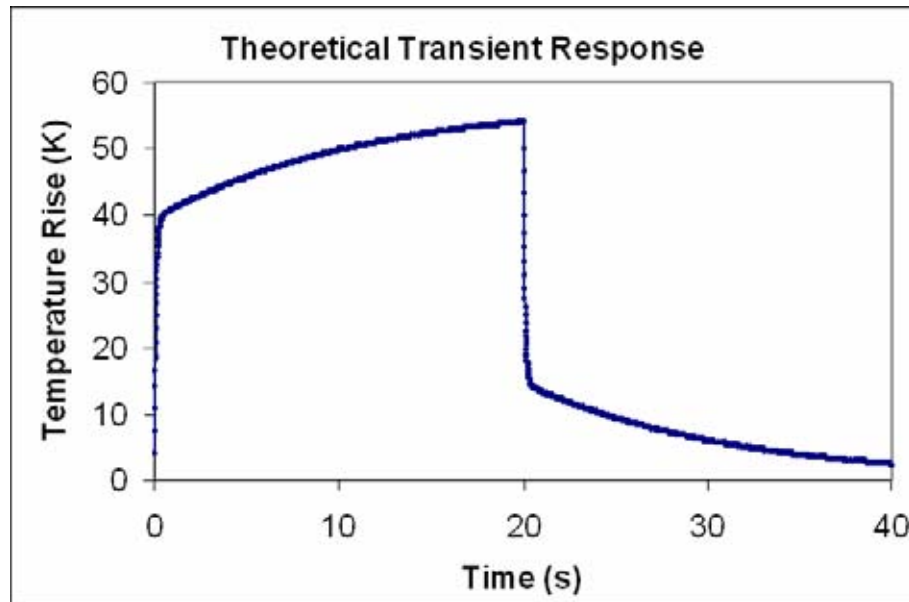


Figure 4.5: Simulated transient response for the energized thermopneumatic actuator, without latching. The input power of 250 mW was applied at 0s and removed at 20s.

The circuit in Fig. 4.4 was simulated in HSpice assuming a 50 μm recess below the heater and an input power of 250 mW. The power was applied at 0s and removed at 20s. The simulation results are shown in Fig. 4.5 and display two distinct regimes of heating. In the first, the cavity temperature increases rapidly with little required energy. In the second, much more energy is consumed as the rest of the valve slowly heats up.

Thus, to fully maximize the performance and minimize the energy requirements of the valve, the device should be designed such that the temperature rise in the first heating regime is sufficient to close the valve. The valve will then be latched (after the first heating regime), and operation in the second regime will be completely avoided saving energy and improving the closing speed. In addition, if the second heating regime is avoided, less thermal energy will need to be dissipated from the device in order to cool down the fluid and open the valve again. Thus, the hybrid actuator may greatly increase the speed of response of the device during both transitions (open-to-closed and closed-to-open). A capacitive sensor is used to monitor the valve seat position to determine the state of the valve and when to latch in order to minimize energy consumption. As shown in Fig. 4.5, the simple thermal model predicts a temperature rise of 39 K in 400 ms while consuming 100 mJ of energy (for a 50 μm recess). If the recess under the heater is increased to 100 μm , according to the model, the same temperature rise can be achieved in 230 ms.

A second thermal model was developed to investigate the temperature gradient across the heater grid and to determine the effect of heat losses through the heater. A top view of the heater grid is shown in Fig. 4.6; the black lines represent the boron-doped silicon beams and the large grey rectangles anchor the heater to the substrate. In addition the heater grid is elevated 50 μm above the substrate. The vertical beams serve to strengthen the horizontal beams and provide more surface area for heat to be transferred to the fluid when the heater is energized. Note that they do not affect the electrical resistance of the heater, as they connect points of equal electrical potential.

This heater grid design is in contrast to the grid by Bergstrom, et. al., in [70], where diamond-shaped grids were used to promote wetting by the fluid and heat transfer to the fluid; their grid was designed for low fill fractions of the working fluid. In this work, larger fill fractions are assumed and the grid in Fig. 4.6 was chosen to increase the resistance of the heater (and increase heating efficiency), to increase the area of heat transfer to the fluid, and to increase the structural integrity of the heater. In [70], additional anchors were used throughout the grid to improve its mechanical stability; however, this also reduces the thermal isolation of the heater. The current grid does not require additional anchors.

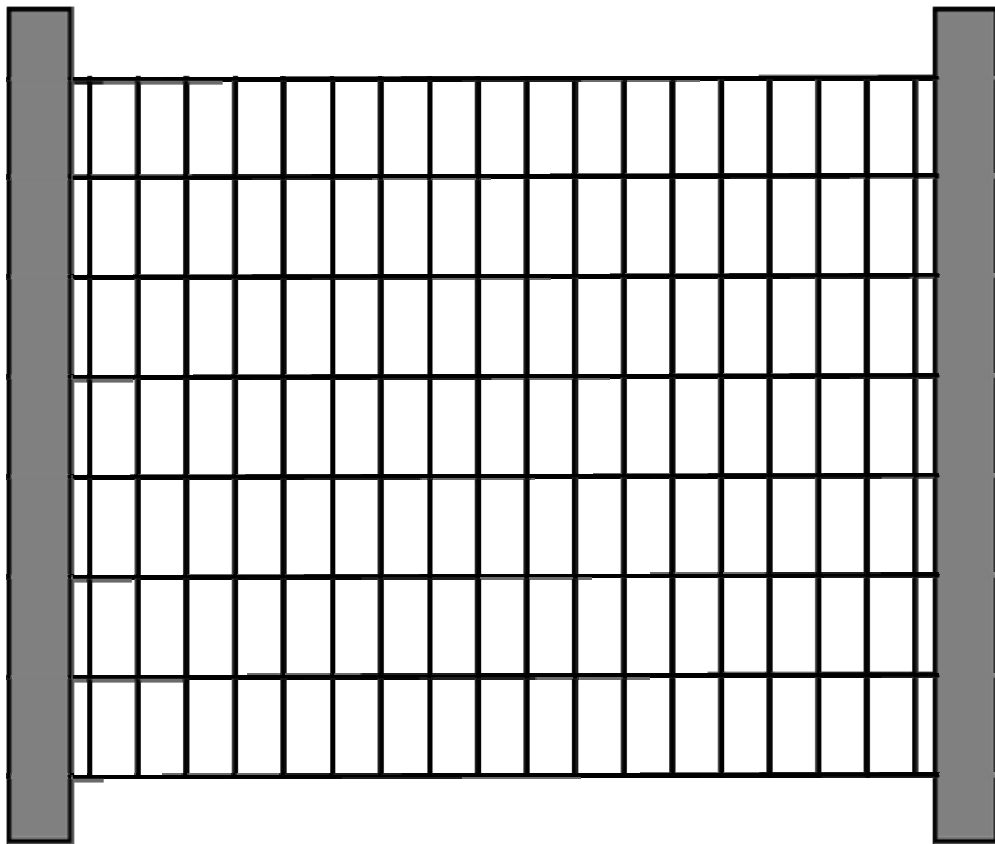


Figure 4.6: A top view drawing of the heater grid. The black lines represent the individual p++ silicon beams and the grey rectangles are the anchors.

In this second model, the heater and surrounding fluid is modeled as a distributed network of resistances and capacitances. Thus, each segment of the grid in Fig. 4.6 is modeled as shown in Fig. 4.7. $R_{Si,n}$ and $C_{Si,n}$ are the resistance and capacitance for the n^{th} boron-doped silicon segment in the grid. $R_{TL,n}$ and $C_{TL,n}$ model the liquid above the heater and $R_{BL,n}$ and $C_{BL,n}$ represent the liquid below the heater. The values were calculated using Eqns. 4.7 and 4.8 and Table 4.2 and are shown in the figure.

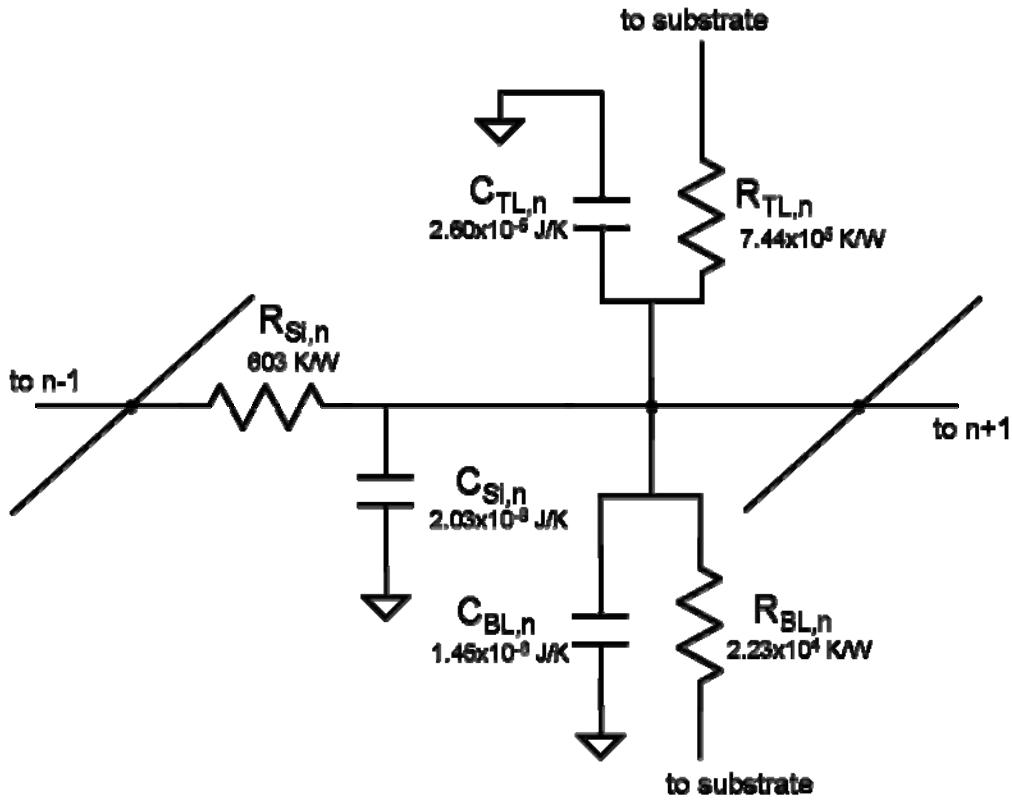


Figure 4.7: The n^{th} node in the distributed thermal model of the heater.

Each segment was connected together and modeled in HSpice and the 250 mW input power was distributed equally among each node in the grid. The transient response of the center of the heater was nearly identical to the response from the simple model in Fig. 4.5. However, the model differed from the simple model in two aspects. First, the

temperature rise of the center of the heater was slightly lower (37 K versus 39 K) due to the losses through the p++ silicon beams. Second, the temperature distribution along the heater grid was not uniform using the distributed model, but instead was more parabolic. Figure 4.8 plots the temperature for all the nodes in the distributed model after applying 250 mW for 400 ms. Figure 4.9 shows a side view of one of the rows. These differences between the simple model and distributed model could be reduced or eliminated by using a heater material with a lower thermal conductivity or by reducing the cross-section of the beams in the heater. In addition, as the recess under the heater is increased greater than 50 μ m, the simple model becomes less accurate because the heat loss through the silicon beams is no longer insignificant relevant to the heat lost through the working fluid. Nevertheless, for its simplicity, the simple model is accurate and provides an

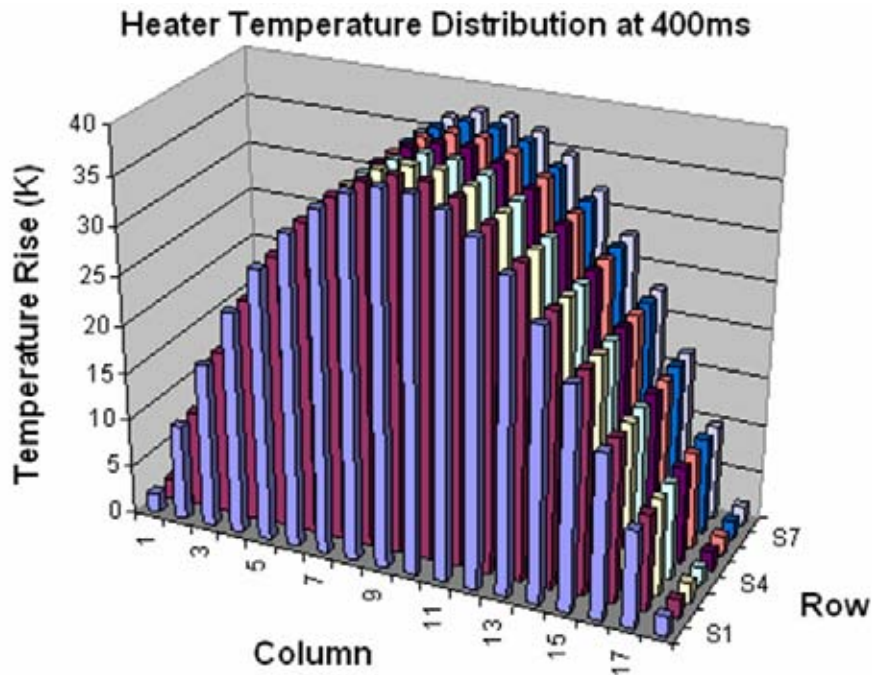


Figure 4.8: Theoretical temperature distribution of all the nodes in the heater grid after applying 250 mW for 400 ms.

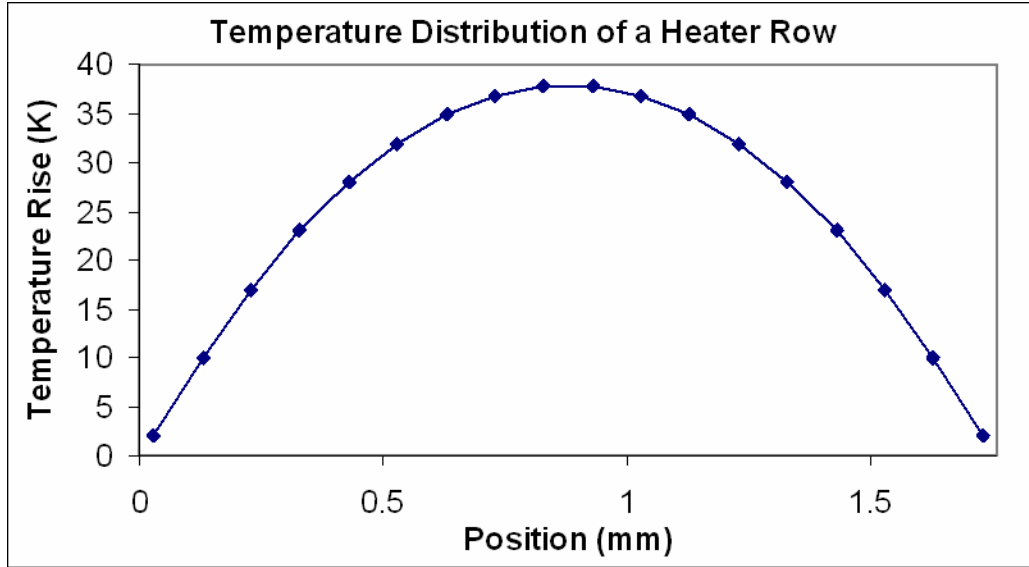


Figure 4.9: Theoretical temperature distribution of one row of the heater grid after applying 250 mW for 400 ms.

understanding of the thermal design of the valve.

Utilizing the temperature of the cavity as predicted using the simple model, the pressure generated by the thermopneumatic actuator can be calculated using the Clausius-Clapeyron relation [43], given in Eqn. 4.9:

$$p_g = p_{g,o} \times \exp \left\{ - \frac{M \Delta h_{lg}}{R_g} \left(\frac{1}{T_{lg}} - \frac{1}{T_{lg,o}} \right) \right\}, \quad (4.9)$$

where p_g and T_{lg} are the pressure and temperature (in K) of the cavity, $p_{g,o}$ and $T_{lg,o}$ are the initial pressure and temperature of the working fluid and gas in the cavity, M is its molecular mass, Δh_{lg} is the heat of vaporization, and R_g is the universal gas constant. This relation gives the pressure of the working fluid as a function of temperature (which is determined from the thermal model) in a closed cavity, but the pressure of the residual air in the cavity must also be taken into account and can be calculated using the ideal gas law and the law of partial pressures, as given in Eqs. 4.10 and 4.11, where p_{air} and $p_{air,o}$,

are the current and initial pressure of the residual air, and p_g is the pressure of the working fluid as given in Eq. 4.9 above.

$$P_{air} = P_{air,o} \frac{T_{lg}}{T_{lg,o}} \quad (4.10)$$

$$P_{tot} = P_{air} + P_g \quad (4.11)$$

Figure 4.10 was generated using Eqs 4.9-4.11 and Table 4.3, and plots the cavity pressure rise versus temperature rise for working fluids with boiling points ranging from 24 to 100 °C. An initial temperature and initial cavity pressure of 20 °C and 748 torr were assumed in the calculations; these values were estimated in order to account for the cooling that occurs as some of the working fluid evaporates during filling. In general, the lower the boiling point of the substance, the larger the pressure it generates for a given temperature. For the current work, pentane was chosen as the working fluid for its low boiling point, ease of handling and availability.

Table 4.2: Properties of various possible working fluids for the thermopneumatic actuator.

	T _{lg} (°C)	Δh _{lg} (J/g)	M (g/mol)
Freon-11	24	180	137.4
Pentane	36	357	72.2
Acetone	56	508	58.1
Methanol	65	1104	32.0
Hexane	69	335	86.2
Benzene	80	394	78.1
TCE	87	261	131.4
Propanol	97	696	60.1
H ₂ O	100	225	18.0

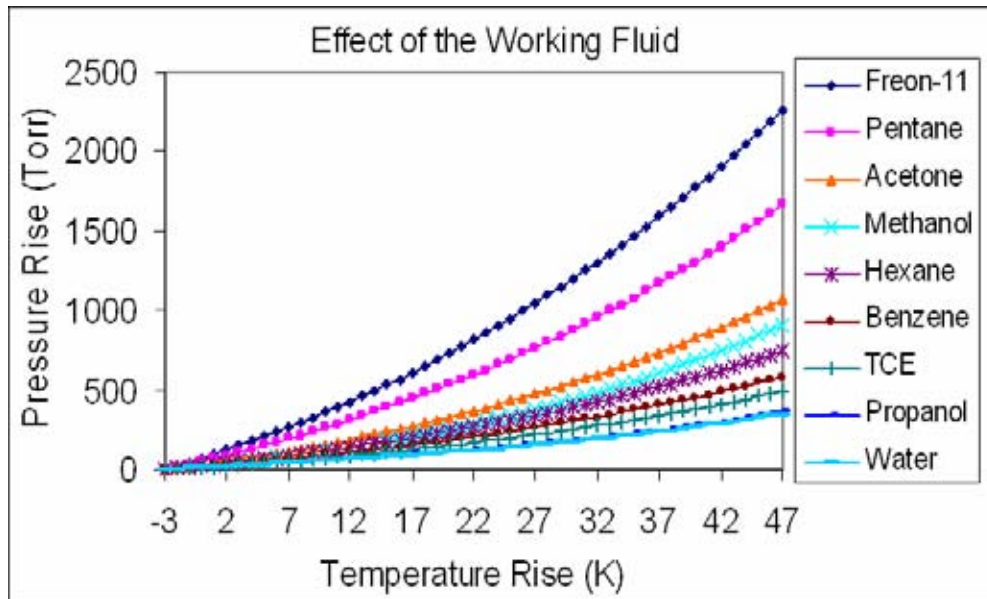


Figure 4.10: A plot of the actuation cavity pressure versus temperature based on the Clausius-Clapeyron relation. Pentane was used in the current devices.

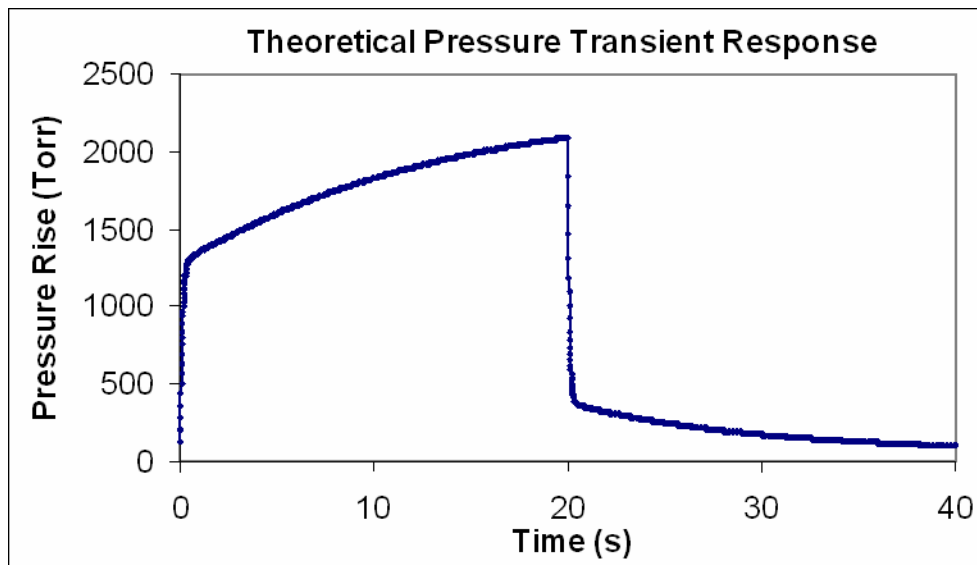


Figure 4.11: Theoretical pressure transient response utilizing the simple thermal model and the Clausius-Clapeyron equation.

Next, the results of the simple thermal model and Eqn. 4.6 were combined to provide the pressure response of the system versus time. The result is shown in Fig. 4.11 and predicts a pressure rise of 1300 torr in 400 ms and 2100 torr in 20s.

4.2.3 Flow Rate Analysis

Because the valve is being developed as part of the μ GC system, it is critical that it have a low pressure drop in order to reduce its impact on the rest of the system. That is, if the valve requires a large pressure drop, it will reduce the flow rate during all stages of operation and negatively impact the system's performance. Thus, it is advantageous to minimize the pressure drop or, equivalently, to maximize the flow rate for the valve. The flow rate can be calculated from standard fluid flow theory as:

$$Q = \frac{P_{DIFF}}{R_{FLUID}} = \frac{P_{DIFF}}{\left(\frac{12\eta L}{Wh^3}\right)}, \quad (4.11)$$

where P_{DIFF} is the differential pressure across the flow channel, R_{FLUID} is the fluidic resistance of the channel, η is the viscosity of the fluid, L is the length of the channel, W is the channel width and h is the height of the channel. This equation is valid for two parallel plates and incompressible flow. Figure 4.12 was generated using equation 4.11 and shows the tradeoff between the flow rate and the channel length and height. A viscosity of 1.8×10^{-5} Ns/m² was assumed for air and the differential pressure and channel width are fixed at 5 torr and 2.35 mm. For the application at hand, a length of 3mm was chosen for ease of testing and interfacing and a height of 38 μ m was chosen to maximize

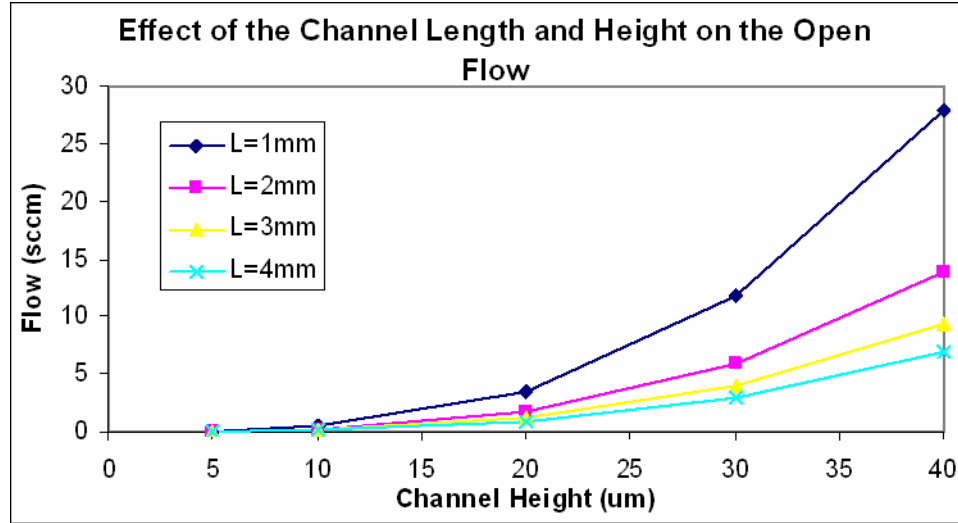


Figure 4.12: Theoretical open flow rate for a differential pressure of 5 torr showing the effect of the channel length and height.

flow rate. With these dimensions, the model predicts a flow rate of 8 sccm for a differential pressure of 5 torr. It should be noted that a larger height requires that the valve plate travel a larger distance to close. This increases the required actuation pressure and thus power required to close the device.

The flow rate of the valve when the valve plate is deflected may be estimated by considering the channel as two fluid resistors in series: the first resistor has the length of the valve plate radius and a height equal to the total gap minus the valve plate deflection and the second consists of the remainder of the channel. Figure 4.13 shows the theoretical flow rate versus valve plate position. The plot assumes a differential pressure of 5 torr and a total gap height of 38 μm .

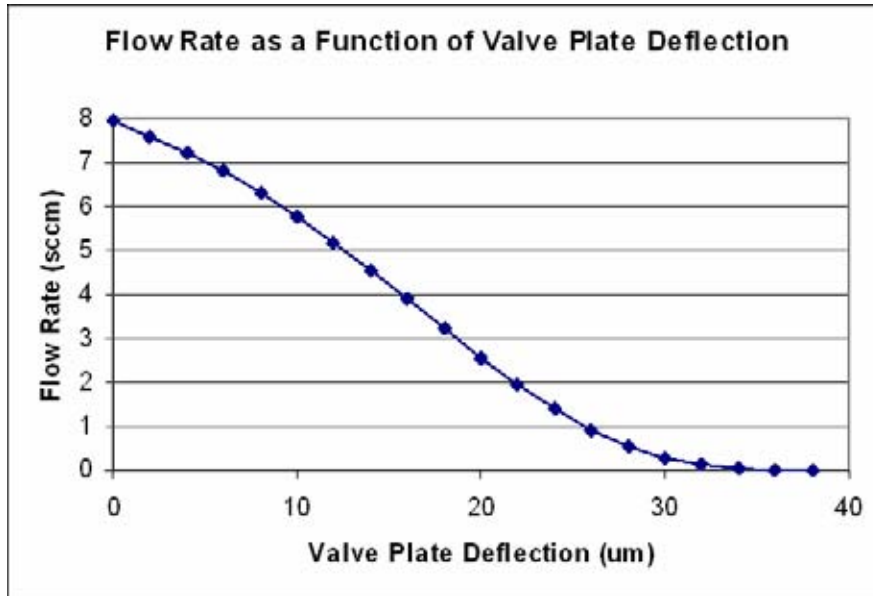


Figure 4.13: Theoretical valve flow rate as a function of valve plate deflection.

4.2.4 Position Sensor Theory

The position sensor in the valve is capacitive and is based on the variation of capacitance with distance.

$$C = \frac{\epsilon A}{d} \tag{4.12}$$

In Eqn. 4.12, C is the capacitance, ϵ is the permittivity of the dielectric material, A is the area of the electrodes and d is the distance between the electrodes. For the current valve, the total capacitance is determined by three separate capacitances: the capacitance of the air between the valve plates, the capacitance of the insulating dielectric on the top electrode, and parasitic capacitance. Note that only the capacitance of the air changes. The total capacitance of the pressure sensor (neglecting parasitics) can be written as the series combination of the two capacitances:

$$\frac{1}{C_T} = \frac{1}{\left(\frac{1}{C_{AIR}} + \frac{1}{C_{INS}} \right)}, \quad (4.13)$$

where C_T is the total capacitance, and C_{AIR} and C_{INS} are the capacitance of the air and insulator, respectively. Both capacitances are determined using Eqn. 4.12. For C_{AIR} , d is calculated as the initial gap distance minus the deflection of the diaphragm. Figure 4.14 was generated using Eqns. 4.12 and 4.13 and assumed a capacitor area of $4.26 \times 10^{-7} \text{ m}^2$, insulator and air relative permittivities of 3.9 and 1.0, respectively, an insulator thickness of $2.3 \text{ } \mu\text{m}$, an initial air gap of $38 \text{ } \mu\text{m}$, and a series parasitic capacitance of 3.8 pF .

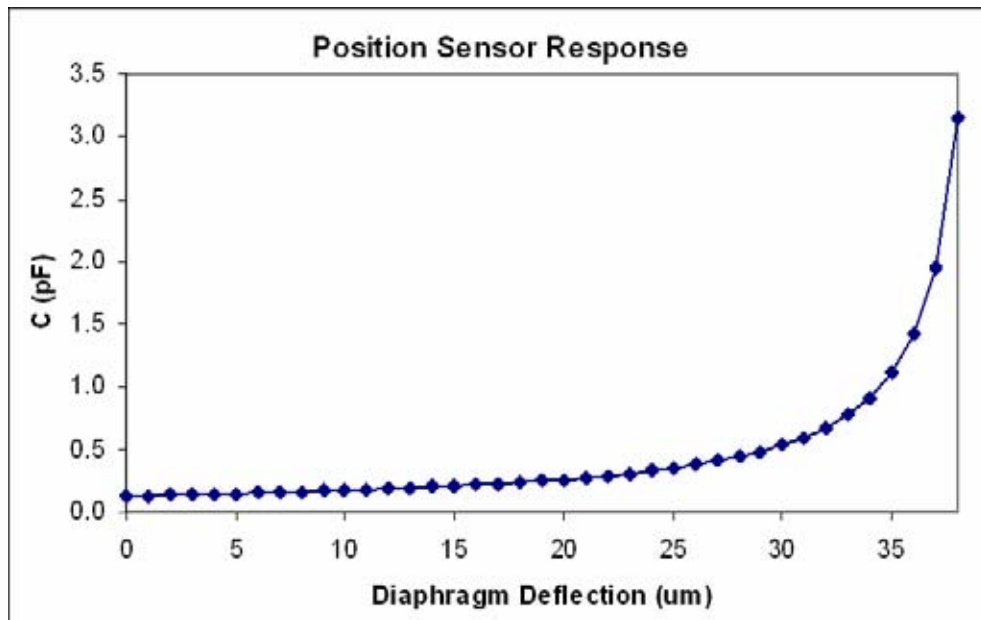


Figure 4.14: The theoretical response of the position sensor.

Next, Fig. 4.15 was generated by combining the equations and theory of Section 4.2.1 and Eqns. 4.10 and 4.11. In this case, it was assumed that the capacitance stops changing for pressures greater than the pressure required to close the valve.

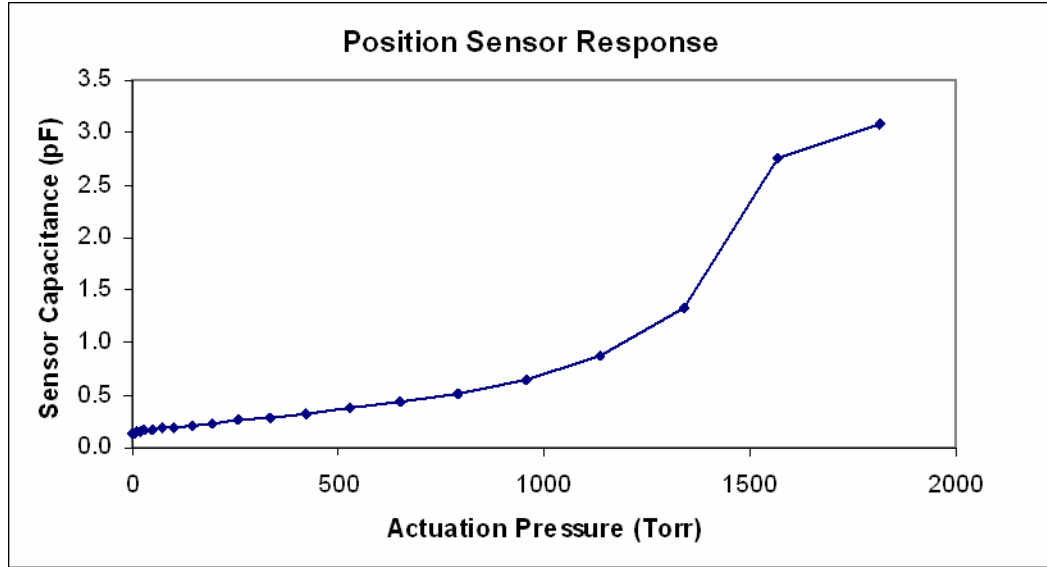


Figure 4.15: Theoretical response of the position sensor as a function of actuation pressure.

4.2.5 Electrostatic Latch Theory

The spring constant of the diaphragm (as determined in 4.3.1) has a large impact on the theoretical voltage required to completely latch the valve in the closed position.

The force of an electrostatic actuator is given by

$$F_E = \frac{A_E V^2 \epsilon}{2t^2}, \quad (4.14)$$

where A_E is the area of the electrostatic actuator, V is the electrostatic voltage, ϵ is the permittivity of the dielectric, and t is the dielectric thickness. In order for the valve to completely latch, the electrostatic actuator must generate a force that is equal or greater than the pneumatic or thermopneumatic force required to close the valve. An estimate of this force may be determined by multiplying the pressure of the pneumatic actuator by the effective area of the diaphragm. Once this force is known, Eqn. 4.14 may be solved for the required latching voltage. Figure 4.16 plots the required electrostatic voltage

versus the pressure required to close the valve. The electrostatic electrode area, relative permittivity of the dielectric and dielectric thickness were assumed to be $4.26 \times 10^{-7} \text{ m}^2$, 3.9 and $2.3 \text{ }\mu\text{m}$, respectively. The pressure required to close the valve is equivalent to the force required for the valve plate to travel the complete gap distance and, thus, can also be thought of as the spring constant of the diaphragm. According to the theory of Section 4.2.1, a pressure of 1570 torr is required to close the valve, giving an estimated latching voltage of 260V. This large voltage is due to the stiff diaphragm and small effective electrode area. It should be noted that voltages less than this voltage will not completely latch the device, but will reduce the required hold power of the thermopneumatic actuator as discussed more in the next section.

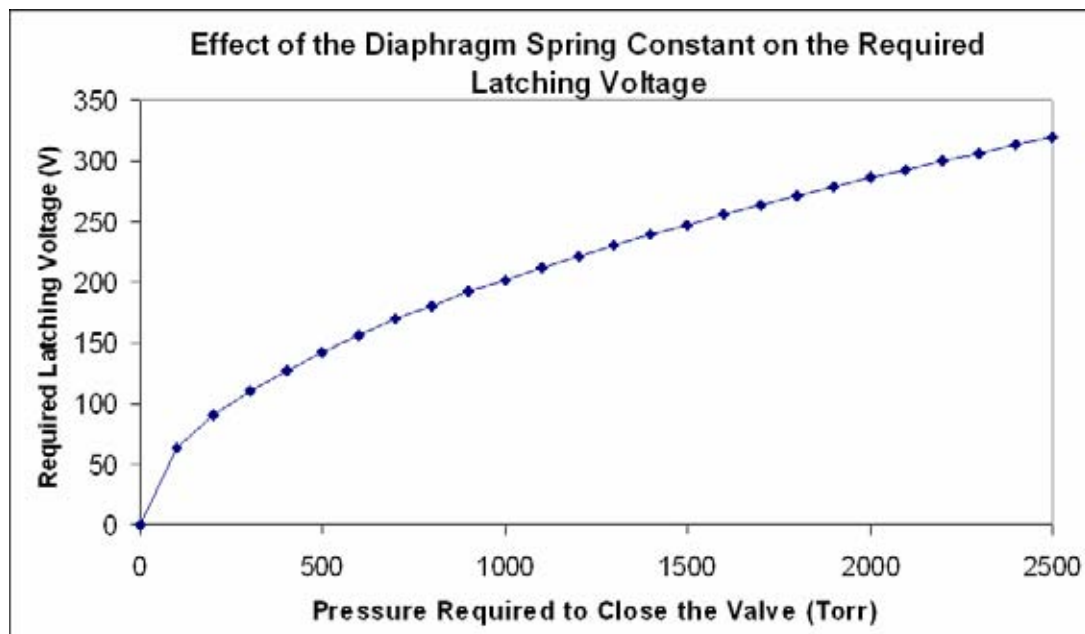


Figure 4.16: Theoretical effect of the spring constant of the diaphragm on the electrostatic hold voltage.

4.2.6 Analysis of Closure

The valve will close and remain closed when the force due to the actuator, F_A , overcomes the combination of the force due to the spring constant of the diaphragm, F_k , and the force due to the differential pressure of the valved fluid, F_{GAS} , as given in Eqs. 4.15 and 4.16.

$$F_A \geq F_k + F_{GAS} \quad (4.15)$$

$$F_A \geq kD + P_{GAS} A_{INLET} \quad (4.16)$$

In Eq. 4.16, k is the spring constant of the diaphragm, D is gap distance or distance of valve seal travel, P_{GAS} is the differential pressure of the valved fluid, and A_{INLET} is the area of the fluidic inlet. For the application at hand, the spring constant should be minimized (while still preserving robustness) in order to increase the effectiveness of the actuator in remaining closed against the fluidic pressure.

Once closed, voltage is applied to the electrostatic latch and power is reduced or removed from the thermopneumatic actuator. In order to remain closed, the force due to the electrostatic latch, F_E , given in Eq. 4.14, and the force of the thermopneumatic actuator, F_T , must overcome the restoring force of the diaphragm and the force due to the differential pressure of the valved fluid. Substituting the $F_E + F_T$ for F_A in Eq. 4.16 and solving for V gives:

$$V \geq \sqrt{\frac{2t^2 (kD + P_{GAS} A_{INLET} - F_T)}{A_E \epsilon}} \quad (4.17)$$

Equation 4.17 gives the minimum required voltage for the valve to remain closed at a given fluid differential pressure. If the differential pressure increases such that the

electrostatic force is overcome, i.e., such that a small gap is created between the valve plate and seat, the valve will quickly transition from closed to open due to the rapid decrease in electrostatic force with distance.

Ideally, the electrostatic latch should be sufficient to hold the valve closed so that power to the thermopneumatic actuator may be removed. However, by substituting in $F_E + F_T$ for F_A in Eq. 4.5, it is apparent that, at a minimum, the electrostatic latch may be used to reduce the power required by the thermopneumatic actuator.

4.2.7 Design Tradeoffs

Table 4.4 summarizes the various tradeoffs in the design of the valve by investigating the effect that increasing each design variable has on the performance metrics. For the current application, low energy consumption, high open flow rate, and decent response time are high priorities

Table 4.3: Tradeoffs in the valve design. A_E is the area of the electrostatic hold, t this the dielectric thickness for the electrostatic hold, h is the diaphragm thickness, and d is the heater recess depth. \uparrow signifies an increase, \downarrow signifies a decrease, and $-$ signifies no change.

Metric	$D \uparrow$	$A_{INLET} \uparrow$	$A_D \uparrow = A_E \uparrow$	$t \uparrow$	$h \uparrow$	$d \uparrow$
Energy	\uparrow	\uparrow	\downarrow	$-$	\uparrow	\downarrow
Open flow	\uparrow	\uparrow	\downarrow	$-$	$-$	$-$
Voltage	\uparrow	\uparrow	\downarrow	\uparrow	\uparrow	$-$
Spring Constant	$-$	$-$	\downarrow	\uparrow	\uparrow	$-$
$P_{GAS,MAX}$	\downarrow	\downarrow	\uparrow	\downarrow	\downarrow	\uparrow
Size	$-$	$-$	\uparrow	$-$	$-$	$-$
Response Time	\uparrow	\uparrow	\downarrow	$-$	\downarrow	\uparrow
Complexity	$-$	$-$	$-$	$-$	$-$	$-$
Robustness	\downarrow	$-$	$-$	\uparrow	$-$	$-$

4.3 Fabrication

The fabrication of the valve, shown in Figs. 4.17 and 4.18, begins with a deep boron diffusion ($\sim 10\ \mu\text{m}$) to define the valve body on a silicon wafer. Next, a shallow isotropic etch is performed to define the corrugations of the valve diaphragm. This etch also serves to recess the portion of the wafer that will not be anodically bonded later. Subsequently, a shallow boron diffusion ($\sim 3\ \mu\text{m}$) defines the valve diaphragm and Cr/Au metallization is patterned on the top of the wafer; this serves to form a substrate contact during the anodic bond. Next, Cr/Au metallization is patterned on the bottom of the wafer. This later will later serve to form a Si/Au eutectic bond with the heater wafer. Separately, a $40\ \mu\text{m}$ recess is wet etched using HF in a Pyrex wafer. This recess forms the fluidic flow channel and accommodates valve plate movement. Next, a Ti/Pt/Au layer is deposited and patterned to form the top electrode of the electrostatic latch and position sensor; the bottom electrode is the substrate of the silicon wafer. Then, a PECVD oxynitride film is deposited and patterned to insulate the top electrode. This insulator only exists in the recessed area and thus does not affect the anodic bond. Fluidic ports are wet etched in the glass wafer using a NaOH electrochemical etch and the two wafers are anodically bonded together. Finally, an EDP etch is done to release the valve seat and diaphragm (shown in Fig. 4.19) and separate individual valve bodies. The top and bottom of the released valve body wafer are shown in Fig. 4.20 and 4.21. In addition, it should be noted that the EDP etch form pillars that will later serve as lead transfers of electrical signals between the top and bottom wafer.

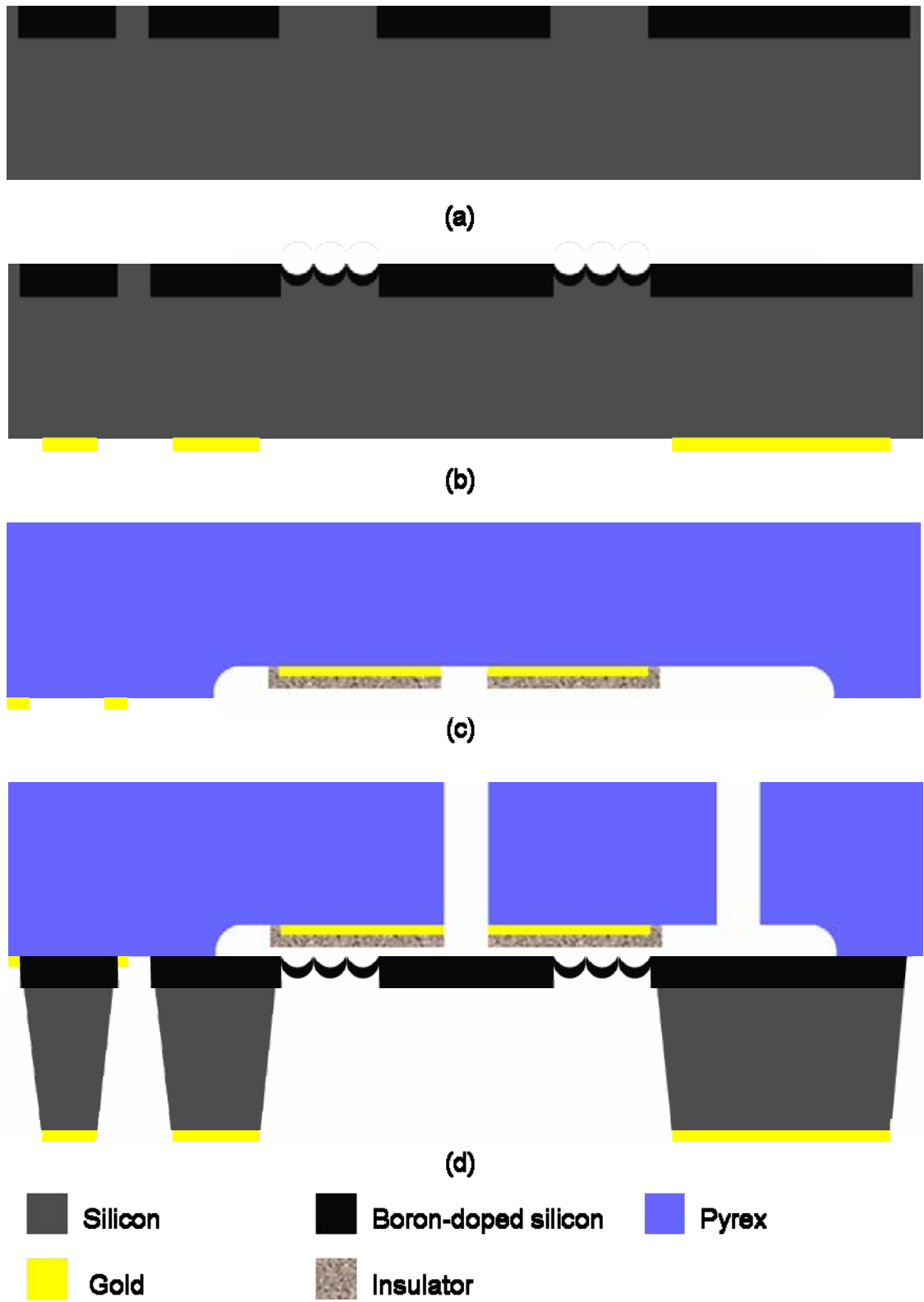


Figure 4.17: The fabrication process for the top half of the microvalve.

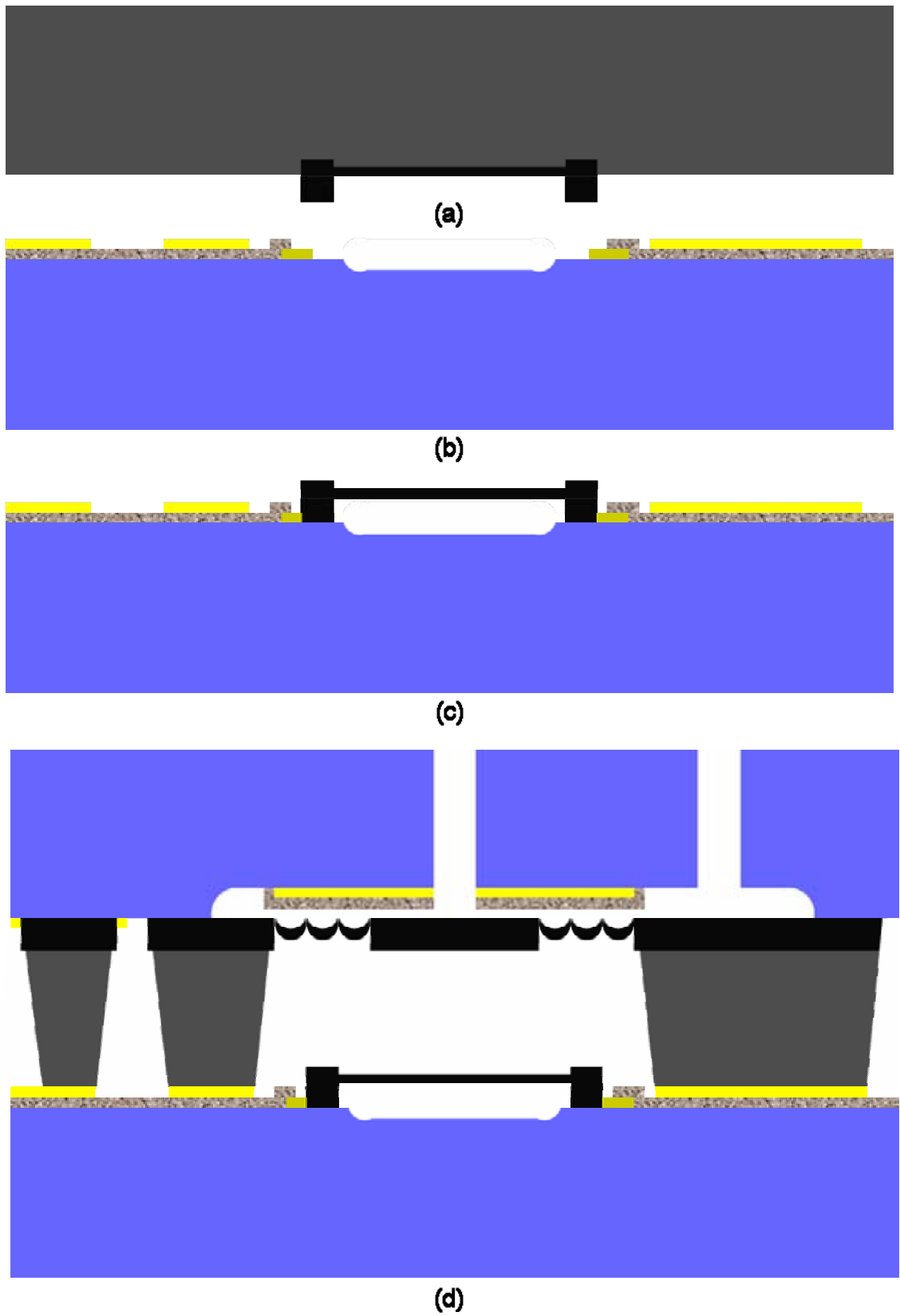


Figure 4.18: The remainder of the fabrication process for the microvalve.

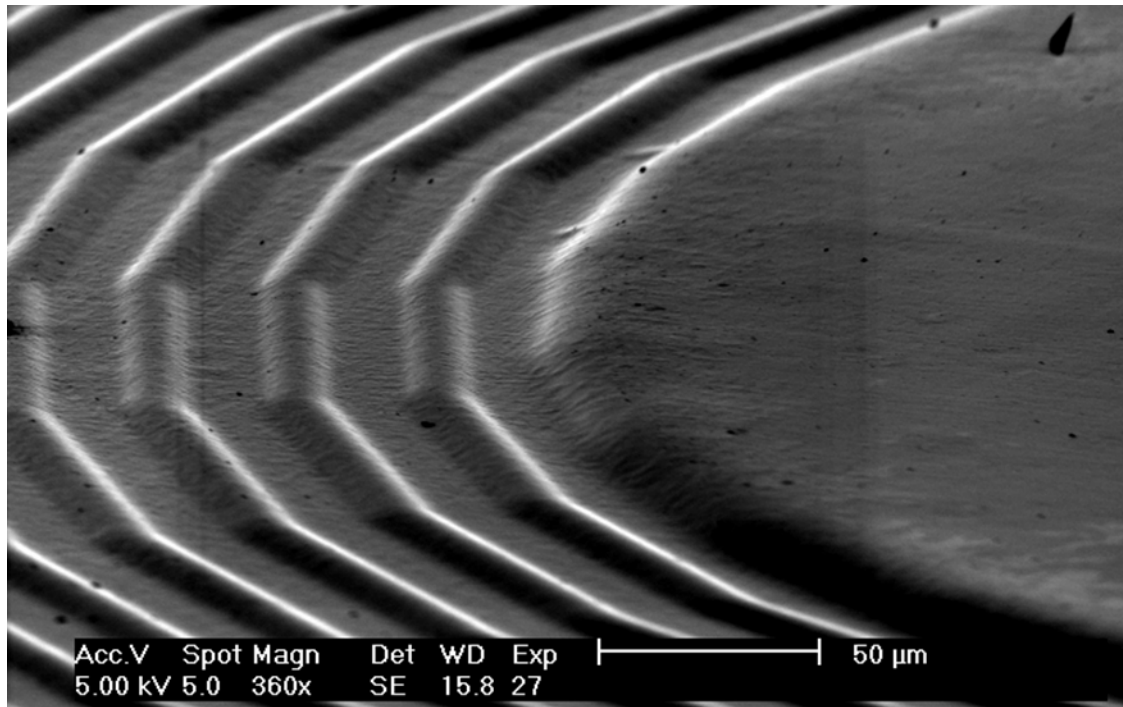


Figure 4.19: A SEM of the bottom side of the valve diaphragm showing the corrugations and valve plate.

The elevated heater is formed in an analogous manner to the process described above, and, in fact, the two wafers can be processed in parallel. The fabrication begins with a short isotropic etch (to elevate the heater) on the silicon wafer, then follows with patterned deep and shallow boron diffusions, and contact metallization. On a separate Pyrex wafer, a Ti/Pt/Au metal layer is deposited and patterned to form the electrical leads, a PECVD oxynitride is deposited and patterned to insulated the leads, a Ti/Pt/Au layer is plated to form a bond ring (for the final Au/Si eutectic bond [68]), and fluidic ports are etched through the glass wafer. These ports are later used to fill the device with the working fluid. An electrostatic bond is then performed and an EDP etch is utilized to release the heater. SEMs of a finished heater are shown in Fig. 4.22 and 4.23. Finally, the valve body wafer and the heater wafer are bonded together utilizing a Si/Au eutectic

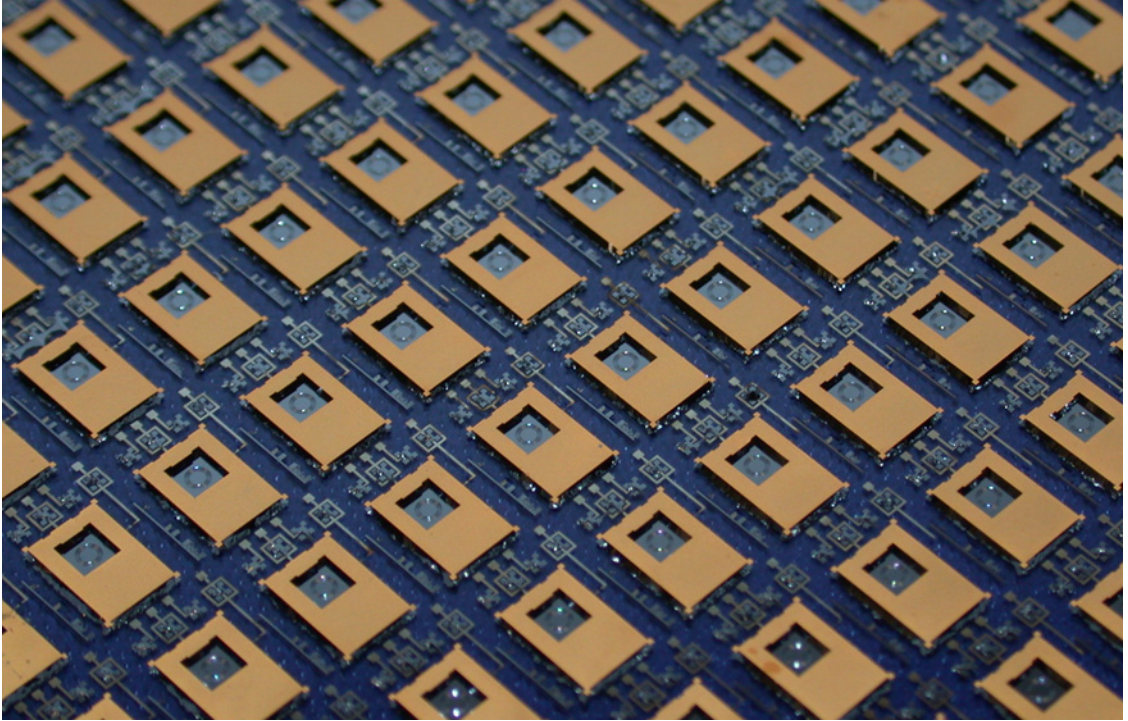


Figure 4.20: Picture of the bottom of the finished valve body wafer.

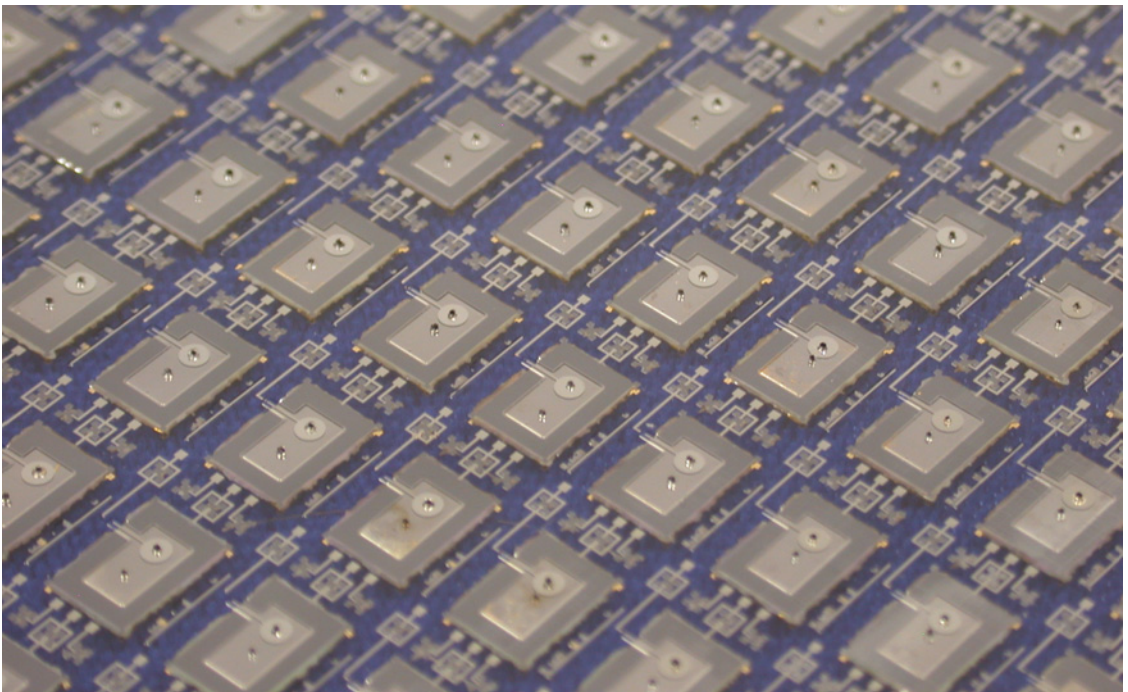


Figure 4.21: Picture of the top of the finished valve body wafer.

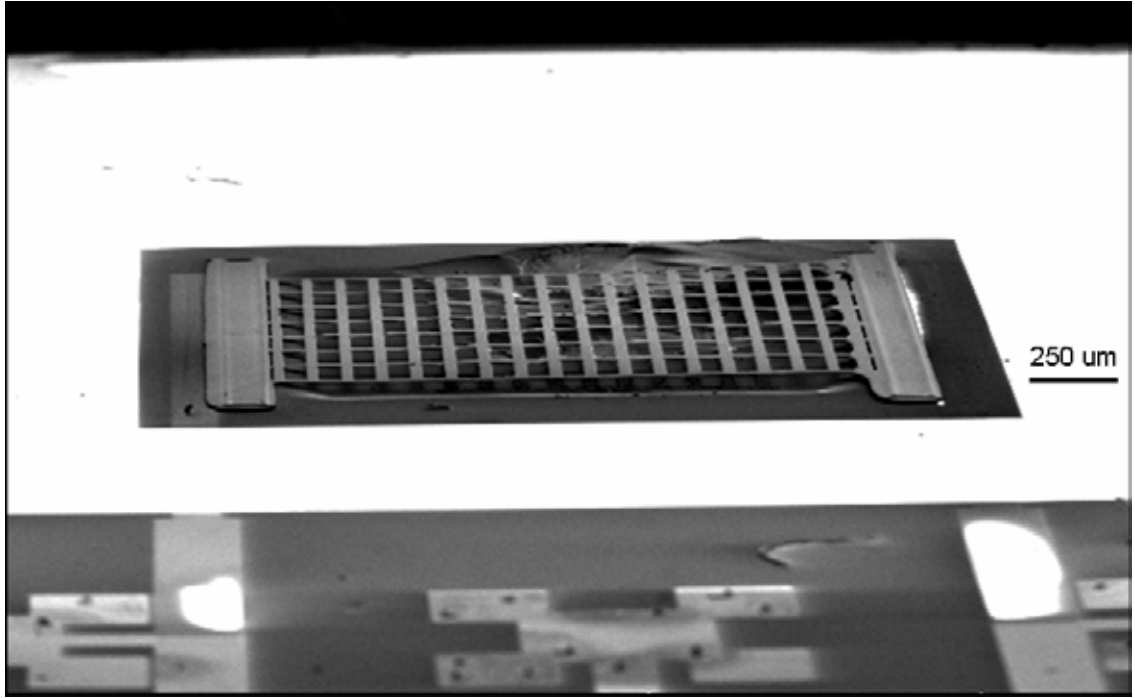


Figure 4.22: SEM of the full heater die. The bond ring surrounds the heater and the electrical leads can be seen at the bottom of the picture.

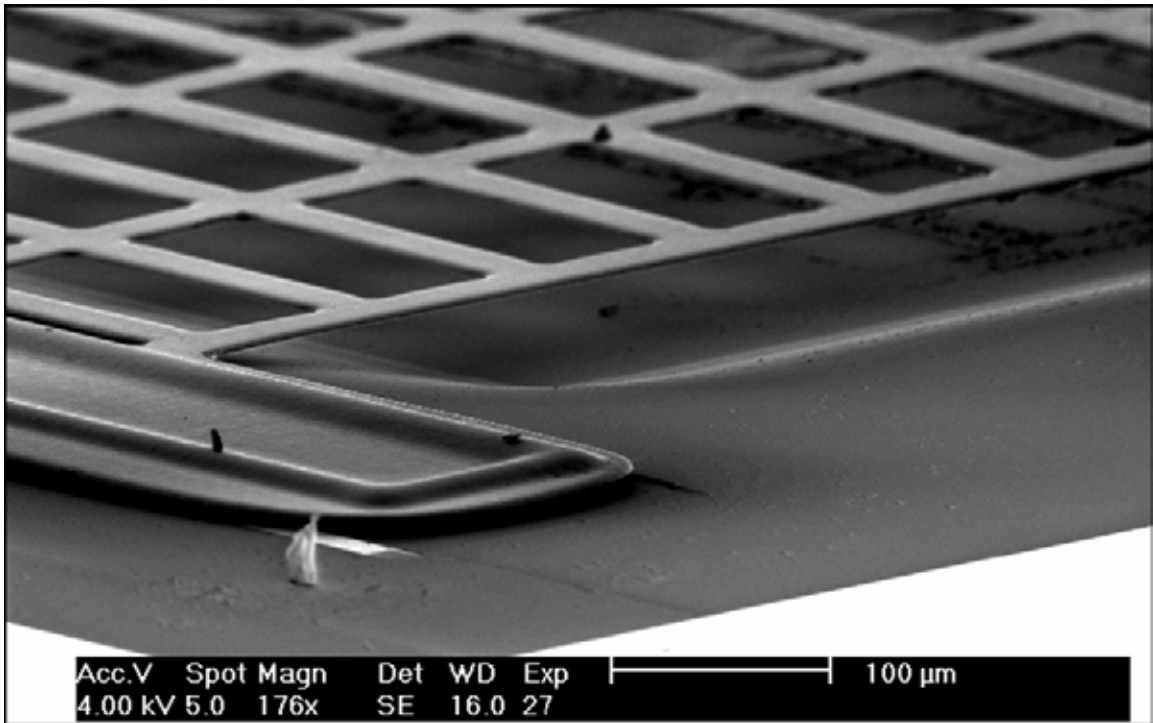


Figure 4.23: SEM of the suspended heater grid, anchor, recess, and electrical feedthrough.

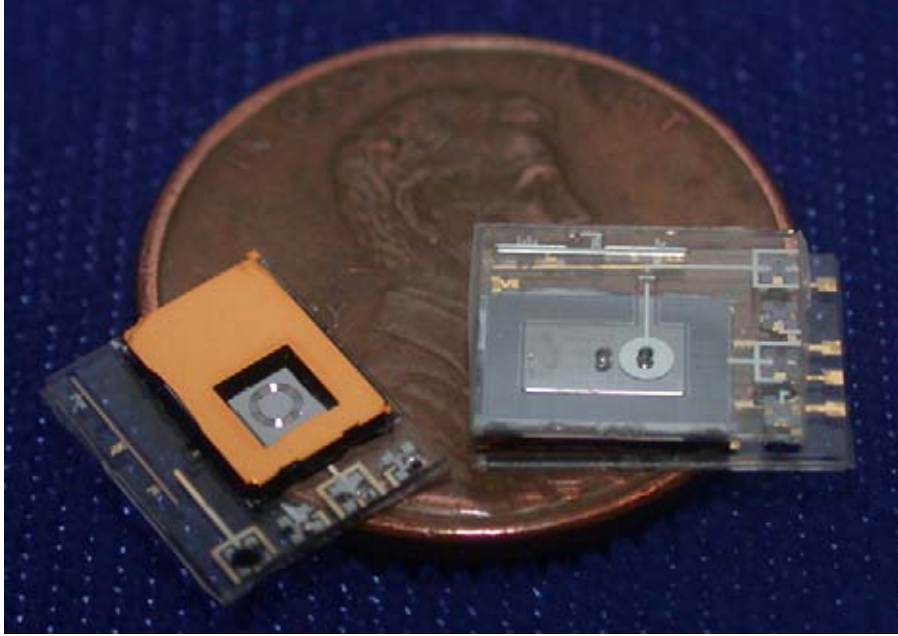


Figure 4.24: The finished valve die (right) and bottom side of the valve body (left).

bond, and then diced to separate the individual die, as shown in Fig. 4.24. After fabrication, the die are injected with the working fluid (pentane in this case) and sealed with epoxy.

4.4 Testing and Results

First, a scanning electron microscope was used to measure the critical dimensions of the completed device. The deep boron diffusion layer was $12\ \mu\text{m}$ thick, the shallow boron layer that forms the diaphragm was $4.2\ \mu\text{m}$ thick, and the initial valve gap distance (glass recess depth) was $38\ \mu\text{m}$.

Next, a custom test setup was designed and implemented for the specific purpose of testing the microvalve. The test setup includes a DH Instruments programmable pressure controller, two pressure transducers, a flow meter and a custom pressure

controller capable of rapidly switching between ambient and a programmable pressure. To facilitate testing, capillary tubing was epoxied into the fluidic ports of the valve and into the actuation cavity of some of the valves (for pneumatic testing).

The test setup was initially used to determine the open flow rate of the valve. First, the flow versus pressure characteristics of the valve and setup were measured. Then, the characteristics of the system alone were calculated and subtracted from the above result to give the graph in Fig. 4.25. As can be seen, the results agree well with the theory and give a flow rate of 8 sccm at 4.6 torr. The departure from theory can be attributed to the variation in the length of the flow channel due to the precision of the glass drilling. In addition, the assumption that the fluid is incompressible may introduce some error in the predicted values. Finally, the error in the measured pressure may be up to 0.2 torr at each point.

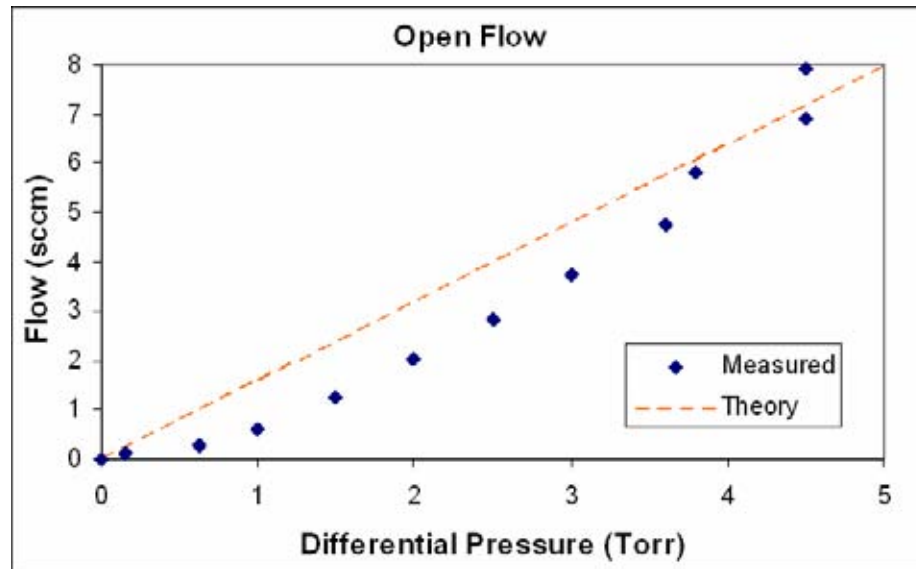


Figure 4.25: Measured open flow rate for the valve.

Next, the position sensor was tested and its response was measured using a HP 4284A LCR meter. During this measurement, the thermopneumatic actuation chamber

was connected to the programmable pressure controller. The results of the measurement are shown in Fig. 4.26 and agree well with theory. The deviation may be attributed to the simplistic theoretical model which assumes the capacitance reaches a maximum when initial touchdown occurs. However, as the pressure increases, the dielectric may compress and the diaphragm around the valve plate will continue to deflect, resulting in a more continuous capacitance curve. In addition, after the valve is released, the area where the shallow boron overlaps the deep boron diffusion is higher in elevation than the rest of the valve plate as described in [43]. This creates a small air gap in the center of the valve plate which is not modeled in the theory. This air gap serves to reduce the actual capacitance at higher pressures (when the valve plate is fully deflected). Overall, the sensor displays a sensitivity of 1.3 fF/torr over the operating range.

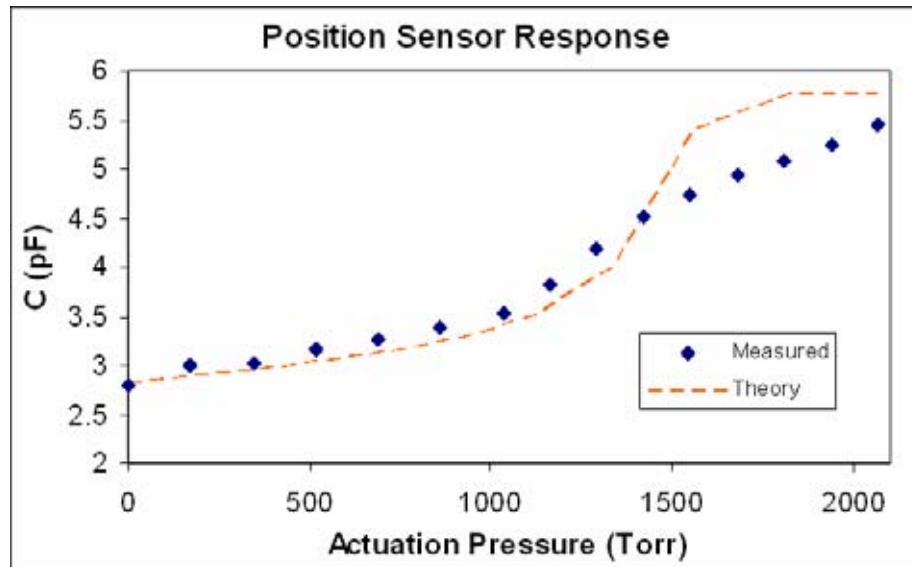


Figure 4.26: Measured response of the position sensor.

Next, the actuation chamber was connected to a pressure controller and the flow rate was measured as a function of actuation pressure. This test yields the actuation pressure required to close the valve at various initial flow rates. The measured data is

shown in Fig. 4.27 and agrees well with the diaphragm deflection theory shown in Fig. 4.3. In both cases, the pressure required to close the valve is about 1500 torr. Please note that the y-axis in Fig. 2.27 is a logarithmic scale. This plot also shows that to achieve the same leak rate, a larger actuation pressure is required for higher initial flow rate (larger differential pressure). It is interesting to note that the flow does not begin to decrease until after 1300 torr, whereas according to the theory of Section 4.2.1 and to the position sensor results of Fig. 4.26, the valve is deflecting for pressures lower than 1300 torr. This is mainly attributed to the fact that the fluidic resistance of the valve is much less than that of the test setup until the valve is nearly closed.

Next, the base switching capabilities of the valve and the time response of the test setup were characterized. For this test, the actuation chamber was connected to a programmable pressure capable of rapidly switching from ambient to a programmed

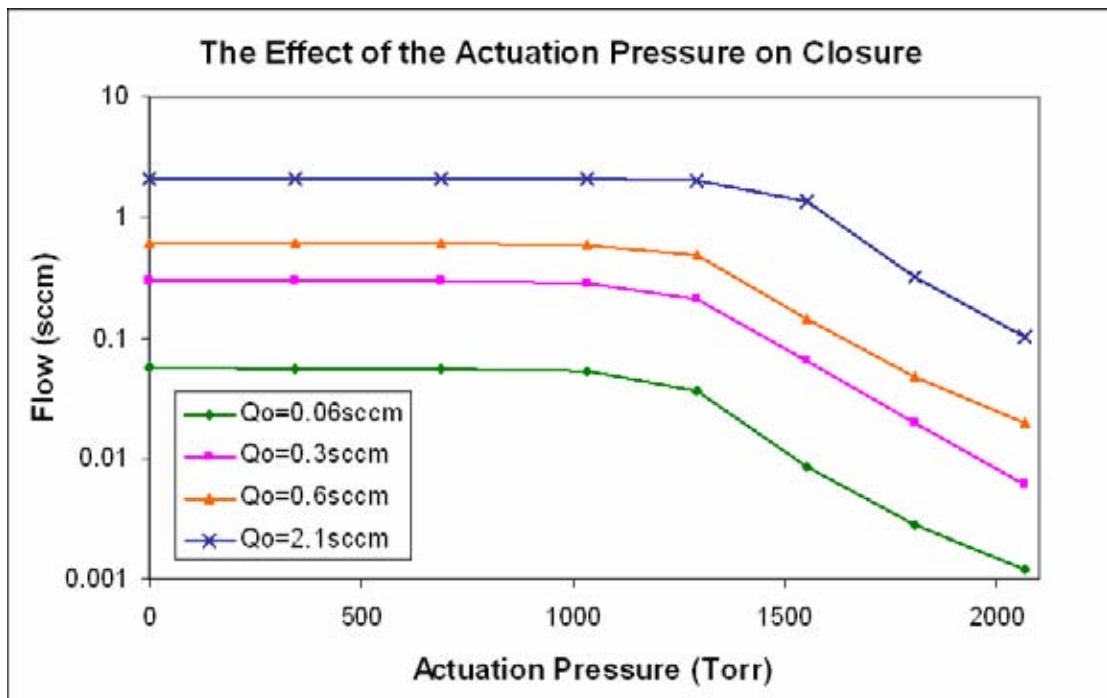


Figure 4.27: Valve flow rate as a function of the actuation pressure.

pressure. The capacitance of the position sensor and the flow rate were measured and the results are shown in Fig. 4.28 and 4.29 for two different initial open flow rates. In Fig. 4.28, the leak rate of the valve is 2×10^{-3} sccm but in Fig. 4.29, the leak rate is 0.3 sccm; a larger actuation pressure is required to achieve lower leak rates. However, this proves the valve is capable of very low leak rates if a high enough actuation pressure is used.

In addition, the time constant of the test setup may be determined from Figs. 4.28 and 4.29. In Fig. 4.29, when the pneumatic pressure is switched closing the valve, the capacitance increases very rapidly (less than 250 ms) from 2.5 pF to 5 pF. However, the flow decreases slowly with a time constant of 5.3s (90%-10% time of 6.7s). This value is the time constant of the test setup.

Next, the thermopneumatic actuator was tested after filling some of the devices with pentane and sealing them with epoxy. It should be noted that pressure should be applied to the epoxy before it has dried to keep the pentane from leaking out. In this

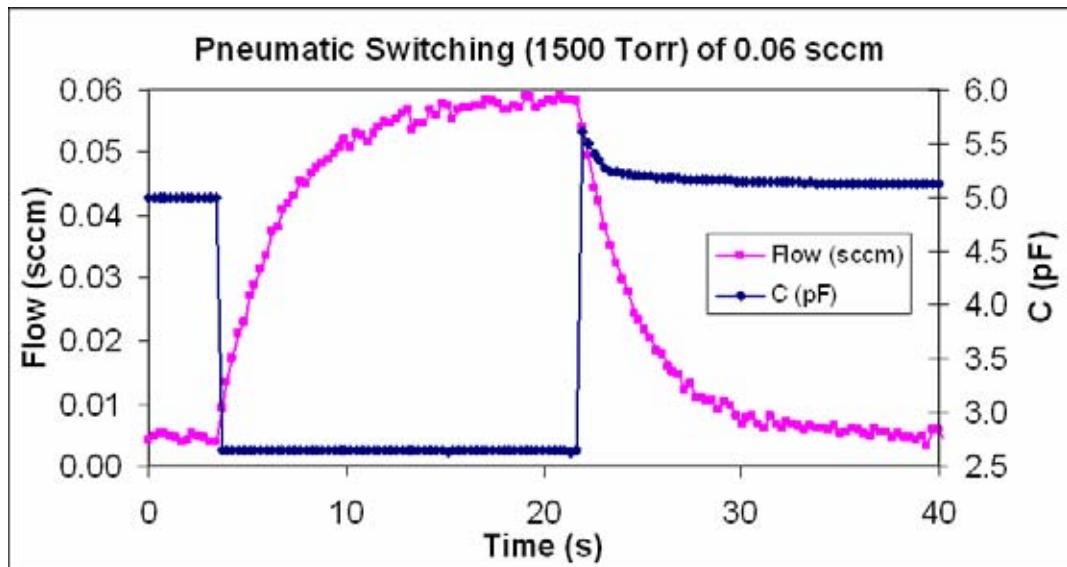


Figure 4.28: Measured results for the pneumatic switching (1500 torr) of 0.06 sccm.

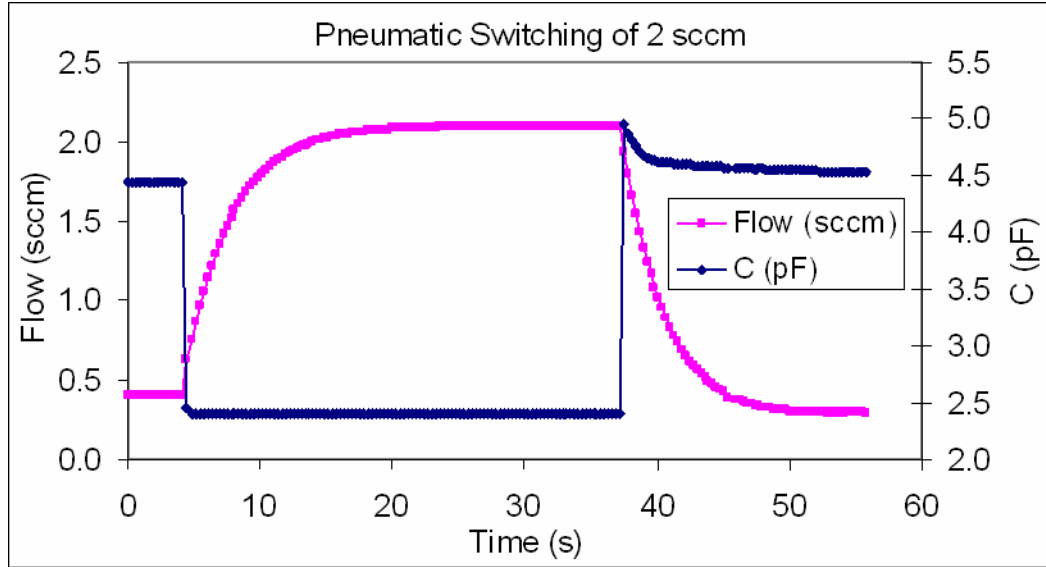


Figure 4.29: Measured results for the pneumatic switching (1500 torr) of 2.1 sccm.

case, a glass wafer was diced, each die was coated with epoxy, and then they were used to seal the bottom of the device after filling with pentane. In addition, a small weight was placed on top of the device while drying.

Before testing, the base heater resistance was measured and was found to be between 7 and 10 Ω , depending on the device. This low resistance is due to the high conductivity of p++ silicon and the relatively large cross-section of each heater beam (32 x 4.2 μm). This equates to a resistance of about 56 Ω for each of the 8, 1.7 mm-long beams in the heater.

After filling and drying, power was applied to the heater in the actuator cavity and the flow and capacitance of the position sensor were measured. Figure 4.30 shows the measured response for 90 mW applied to the heater. At 90 mW, the valve and test setup have a flow rate switching time constant of 8.9s combined (90%-10% switching time of 13.6s). After subtracting out the time constant of the test setup, this gives a time constant of 3.6s (90%-10% switch time of 6.9s) for the valve at 90 mW. When compared to the

pneumatic transients in Figs. 4.28 and 4.29 above, it is interesting to note that when pneumatic actuation is used, the position sensor capacitance increases very rapidly as the pressure is switched between two fixed values. However, in the graph of Fig. 4.30, the position sensor capacitance increases linearly over time as the valve closes. This is attributed to the fact that when using thermopneumatic actuation, the pressure continues to rise over time as the working fluid and valve heat up. Finally, the average leak rate between 33 and 38s in the graph in Fig. 4.30 is 1.3×10^{-3} sccm.

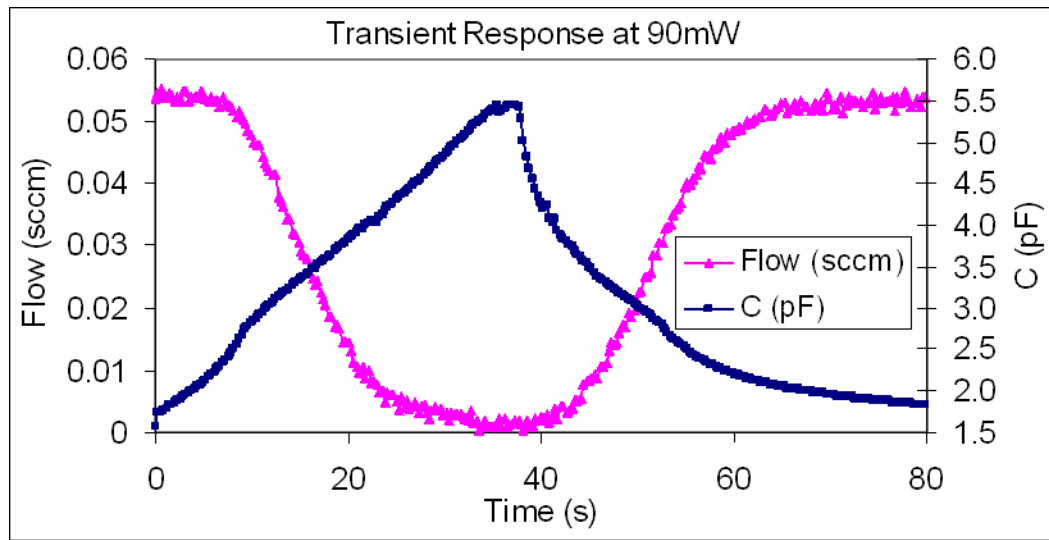


Figure 4.30: Measured thermopneumatic transient response with 90 mW applied to the heater.

After testing at low power levels, the power delivered to the heater was increased and the transient response was again measured. Fig. 4.31 demonstrates the ability of the valve to switch high flow rates. At 200 mW, the valve flow rate switches from 6.74 sccm to 2.2×10^{-3} sccm in 1.1s (90%-10%), an on-off ratio of over 3000. Due to the nature of the test setup, when the valve is open, the differential pressure across it is 4 torr. When the valve is closed, the pressure across it is 860 torr. This results in a closed-to-open fluidic resistance ratio of over one million. Finally, Fig. 4.32 shows the transient

response of the valve with 250mW applied to the heater. In only 430 ms (90%-10%), the valve switches from 1.1 sccm to 1.4×10^{-3} sccm.

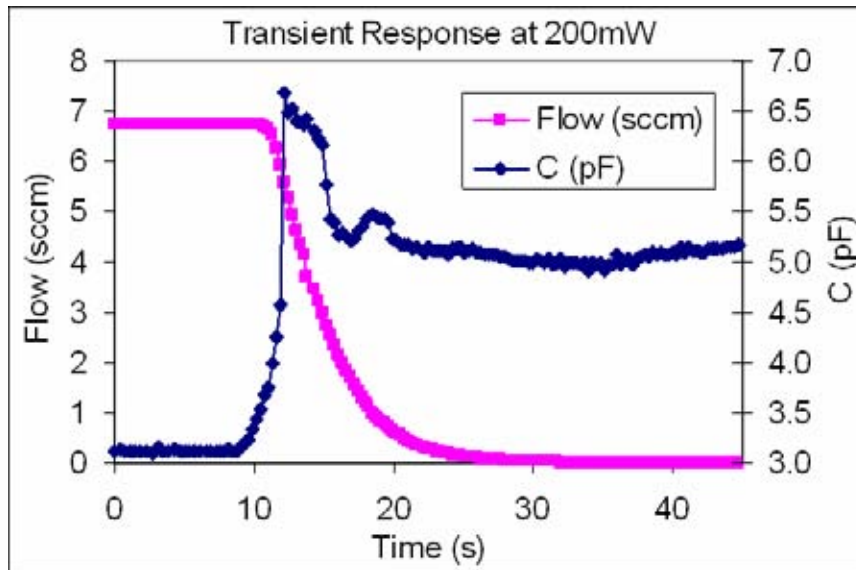


Figure 4.31: Measured thermopneumatic transient response with 200 mW applied to the heater.

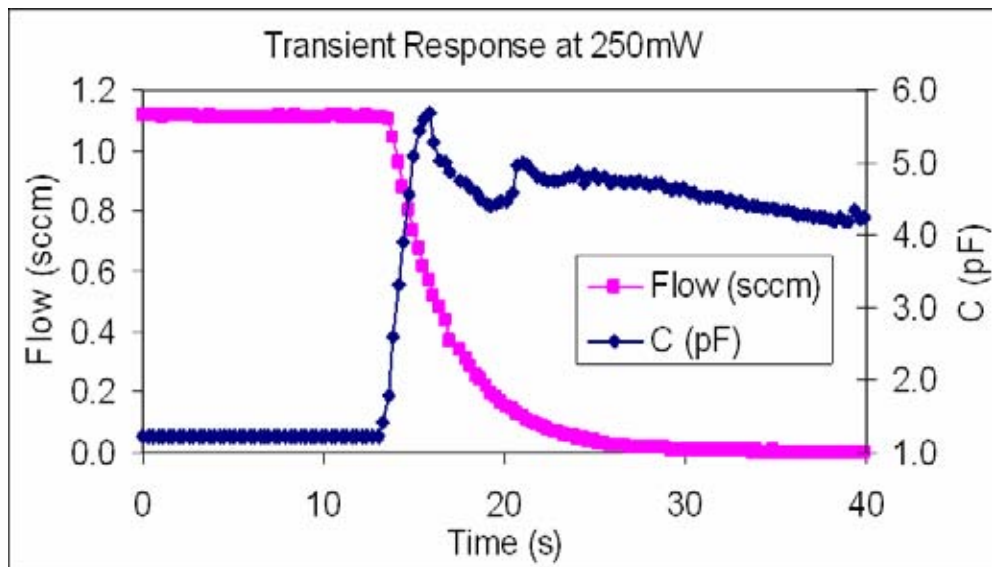


Figure 4.32: Measured thermopneumatic transient response with 250 mW applied to the heater.

It should be noted that although a high power is required to close the valve quickly, a power of 90 mW will hold the valve closed. Thus, if fast speed is required, a 430 ms pulse of power at 250 mW should be used followed by operation at 90 mW. Also, a lower hold power may be used if a leak rate as low as 1.3×10^{-3} sccm is not needed for the application.

In order to test the electrostatic latch, a valve was pneumatically actuated with a pressure of 2000 torr and the voltage to the electrostatic latch was varied. As the electrostatic latch voltage increased, the leak rate decreased as shown in Fig. 4.33. By applying up to 140V, the leak rate could be reduced by almost a factor of 2. This property of the hybrid actuator may be useful in power sensitive applications that require low leakage rates. Finally, the valve was actuated with a pneumatic pressure until it closed (2070 torr) and up to 140V was applied to the electrostatic latch. The initial flow rate was noted. The pneumatic pressure was then decreased until flow through the valve increased above this initial flow rate, which occurred at 1400 torr. Thus, the electrostatic

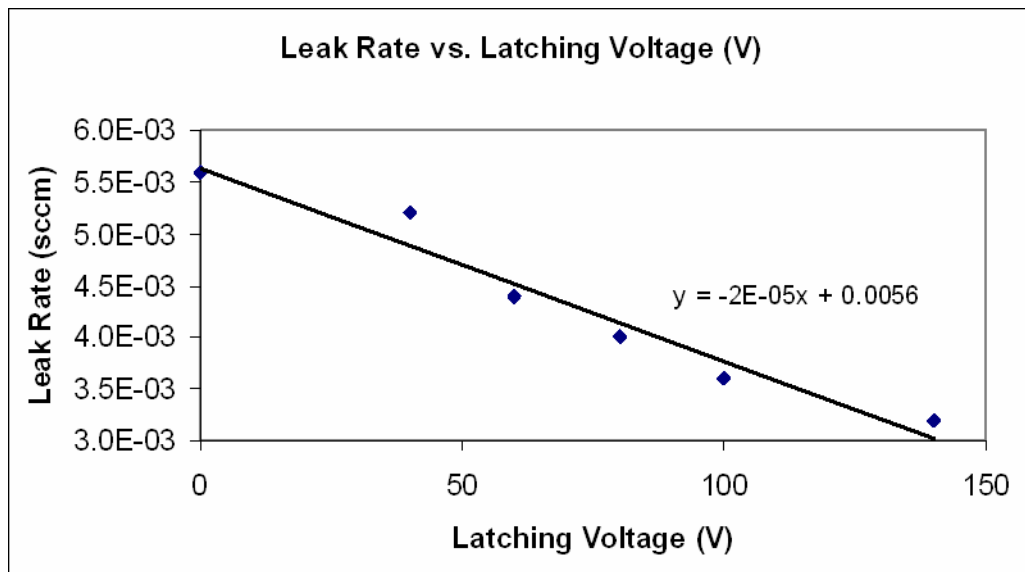


Figure 4.33: Measured leak rate versus applied electrostatic latch voltage. An actuation pressure of 2000 torr was used in conjunction with the electrostatic latch.

latch permitted the reduction of the actuation pressure by 33%. This relates an approximate 33% savings in power and equates to a required hold power of 60 mW when the valve is closed.

4.5 An Improved Microvalve

Several small changes to the design of the valve presented in this chapter would lead to a valve with improved performance. First, the diaphragm should be thinned from 4.2 μm to 3 μm in order to reduce the spring constant of the diaphragm, thereby reducing the pressure required to close the device (from 1570 to 770 torr) and reducing the required electrostatic hold voltage. Next, the thermal conductivity of the heater should be reduced in order to make the thermal losses through the heater beams negligible and improve temperature uniformity. This can be accomplished by either choosing another heater material or reducing its cross-section. Next, all of the glass underneath the heater should be removed to maximize its thermal isolation.

With these improvements, the theory and experimental results of this chapter predict a valve with the same flow and leak properties as before, but capable of closing in 140 ms at 250 mW, requiring a hold power of 6 mW without the electrostatic latch, and no hold power with an electrostatic voltage of 180V.

Chapter 5

Conclusion and Future Work

5.1 Thesis Summary

In this research, a robust, fast, and high-performance silicon-glass microcolumn for a gas chromatograph has been designed and demonstrated (with integrated pressure sensors), electrostatically-latching thermopneumatic microvalves have been fabricated and tested, and ultra-low power, very high speed Sion microcolumns have been developed and experimentally tested. A list of the accomplishments for each device is listed below, followed by the contributions of this thesis.

A Silicon-Glass Micro Gas Chromatography Column

1. Through collaboration with the Richard Sacks' group in the Chemistry Department at the University of Michigan, a system-based design approach was used that resulted in a 160 μm -wide, 250 μm -deep, 6 m-long column with 35000 theoretical plates and a holdup time of 35s.
2. A fabrication process was developed based on a silicon-glass process enabling a robust, cost effective column with integrated heaters, temperature sensors and pressure sensors.
3. Through collaboration with the Richard Sacks' group, the devices were coated with a non-polar PDMS stationary phase and achieved world record efficiencies of over 4000 plates/m and the separation of 30 components in less than 6 min.

A Low Mass Sion Micro Gas Chromatography Column

1. The chromatography, thermal, and flow theory of the column and the μ GC system requirements were analyzed to arrive at an 80 μ m-diameter, 1 m-long, semi-circular column with 16000 theoretical plates and a holdup time of 2s.
2. A fabrication process was developed in which a stress-free, silicon oxynitride layer was undercut to form the channel and then sealed and released to close and suspend the column resulting in a thermally isolated, low mass column structure with integrated heaters and temperature sensors. In addition, a bonding technology was demonstrated to vacuum encapsulate the column.
3. The lowest power (11 mW for a 100 °C temperature rise), lowest thermal time constant (10.4s) column to date was experimentally demonstrated.
4. In collaboration with the Richard Sacks' laboratory, coated the devices with a non-polar PDMS stationary phase and demonstrated the high quality separation of 10 VOCs in 52s and four CWA simulants and an explosive simulant in 60s.

A Hybrid Thermopneumatic and Electrostatic Microvalve

1. The first hybrid thermopneumatic and electrostatic actuator and valve was designed and developed. The complete theoretical analysis predicted a valve that closes in 400 ms at 250mW, a required electrostatic latch voltage of 260V, and an open flow rate of 8 sccm at a differential pressure of 5 torr.
2. A robust design and fabrication process for the microvalve were developed based on the dissolved wafer process and featuring a corrugated boron-doped diaphragm and elevated, thermally isolated heater. The process achieved a valve body yield of over 90%.
3. The valve achieved a response time of 430 ms, a large open flow rate (8sccm @ 4.6 torr), a low leak rate (1.3×10^{-3} sccm @ 860 torr), a closed-to-open fluidic resistance ratio greater than one million, zero static power when open, 60 mW hold power when closed, zero power required to open the valve, and a required energy of 108 mJ to close the valve.
4. With minor improvements, the valve requires 35 mJ to close in 140 ms, a hold power of 6 mW without the electrostatic latch, and no hold power with an electrostatic voltage of 180V.

Contributions of this thesis:

- I. Microsystem Design & Theory

1. A system-based approach to GC column design and fabrication, including the tradeoffs in the system and limits of performance
 2. The first low-mass and low-power microcolumn to perform the high quality separation of complex mixtures
 3. The first hybrid thermopneumatic and electrostatic microvalve and actuator
 4. A fundamental understanding of the design tradeoffs of the hybrid thermopneumatic and electrostatic actuator and microvalve
- II. Fabrication Technology
1. A robust process for the fabrication of low mass, suspended microcolumns with integrated heaters and temperature sensors.
 2. A high yield, reliable fabrication process for a hybrid thermopneumatic and electrostatic microvalve with closed-loop position sensing.
 3. A new bond technology utilizing metal feedthroughs, a PECVD isolation layer, and a Si/Au eutectic bond.
- III. System Level Implementation
1. Characterization of the size, power, resolving power, and flow rate tradeoff for the column
 2. System-based design of the microvalve and microcolumn in a temperature - and pressure-programmed μ GC system
 3. Integration of the silicon-glass columns into the μ GC system.

5.2 Suggestions for Future Work

The silicon-glass column is robust, thoroughly tested and has a simple fabrication process. Thus, in terms of design and fabrication, there is very little additional research that needs to be done and, thus, it is not covered in this section. There is still research in the areas of silicon microcolumns, hybrid microvalves and system integration; these are covered in the following subsections.

5.2.1 Sion Microcolumn

The Sion column is the highest performing column to date in terms of power and speed. In addition, it has demonstrated high quality separations. However, there is still research to be done before the device becomes a practical reality.

First, although the column has a very low overall response time, the corner of the column heats up in 2.6s and the center heats up in 10.4s; thus, the column temperature is non-uniform during ramping. This may limit the performance of the device during fast temperature ramp rates. To alleviate this issue, the heater should be redesigned such that it offsets any temperature non-uniformity during ramping. That is, this heater should supply a different power to each area that is proportional to its local time constant. For instance, since the column center requires longer to heat up than the corner, more power should be applied to the center to correct this. Thus, the column should contain heaters that offset the steady state thermal losses, and an additional heater that is used to improve the temperature uniformity during transients.

Second, the device has been designed for vacuum packaging, but this has not yet been achieved. Thus, a vacuum packaging technique for the column should be investigated and implemented. A gold-silicon eutectic bond provides a promising option, as it has already been tested and used to cap the device and form fluidic connections. Getters should be investigated to reduce the pressure below 10 mTorr.

Next, to further make vacuum packaging possible, research must be done to reduce the diffusion of the carrier gas and sample through the bottom of the column wall. At only 1 to 2 μm thick, simple calculations show that the vacuum would degrade rapidly given the long length and surface area of the bottom of the column. Thus, after release,

another PECVD oxynitride deposition should be performed to increase the thickness of the column wall to 10 or 15 μm . Additionally, a thin metal layer may be deposited to further reduce out-diffusion and to increase the temperature uniformity of the column. However, care must be taken to minimize the stress of such a layer.

Finally, it is suggested that research in the area of localized or selective stationary phase coating be performed. The ability to selectively coat areas of the channels and column could potentially reduce or completely eliminate the problem of cold spots. Such selective coating could be performed by locally heating and, thus, cross-linking the stationary phase using the column heaters.

5.2.2 Hybrid Thermopneumatic and Electrostatic Microvalve

The microvalve presented in this thesis has a very large open flow rate, a low leak rate, a decent switching time, and a relatively low power requirement. However, it still can be improved further.

First, research should be performed in order to further improve the valves heating efficiency. This can be accomplished by first reducing the thermal conductivity of the heater material and by reducing the cross-sectional area of the heater beams. Next, the resistance of the heater's electrical leads should be minimized to reduce heat loss to the substrate. Finally, the recess under the heater may be increased ($>100 \mu\text{m}$) to further improve the heater's thermal isolation.

Finally, work should be performed to increase the effectiveness of the electrostatic latch. It is suggested that the valve diaphragm be thinned to reduce the spring constant of the diaphragm and reduce the required hold voltage. Additionally or

separately, the area of the valve diaphragm and valve plate may be increased in order to reduce its spring constant and to increase the area of the electrostatic latch. Finally, alternate diaphragm materials, such as silicone rubber or parylene, may be investigated to further reduce the spring constant. However, with a small spring constant, care must be taken to ensure that the temperature required to close the valve is much greater than the that associated with the environmental requirements of the application. It should be noted that such layers also have higher permeabilities than silicon and, thus, must be carefully designed so that the working fluid and vapor do not escape the thermopneumatic cavity over time.

5.2.3 System Integration and Design

Once the improvements to the column and valve have been made, work needs to be done to integrate the devices and form the compact pressure- and temperature-programmed system. The devices have been designed such that they can be integrated together by mounting a fluidic substrate on top of the column. The valves (and other fluidic components) would then be mounted on top of the fluidic substrate as shown in Fig. 1.10. Care should be taken to remove leaks and dead volume in the system.

For future μ GC systems, work can be done to fully integrate the micropump, valves, preconcentrator, and detector into a single fabrication process. For example, using the Sion column process in Chapter 3, the working membranes of a pump and valve may be formed from the top Sion layer (because it is flexible, zero stress, and has a buried metal layer). These membranes could be either electrostatically or thermally actuated. A thermal conductivity detector or other detectors may also be integrated into

such a process utilizing the high thermal resistance of the Sion layer. Finally, a simple preconcentrator may be formed using a short column coated with a thick stationary phase. Overall, such a system would have a very low (zero) dead volume and would facilitate further miniaturization of the column and, thus, further reduced power and energy requirements. Such miniaturization of the column dimensions (length and diameter) would require improved coating methods (to achieve thinner stationary phases) so that column performance would not be sacrificed. Finally, a number of new selective coating methods are being explored to reduce or eliminate cold spots and improve separation performance; work should continue in this area.

References

- [1] S. C. Terry, J. H. Jerman and J. B. Angell, "A Gas Chromatographic Air Analyzer Fabricated On A Silicon Wafer," *IEEE Transactions on Electron Devices*, vol. 26, pp. 1880-1886, 1979.
- [2] M. W. Bruns, "Silicon Micromachining and High Speed Gas Chromatography," *Proceedings of the 1992 International Conference on Industrial Electronics, Control, Instrumentation, and Automation. Power Electronics and Motion Control*, vol. 3, pp. 1640-4, 1992.
- [3] G. C. Frye-Mason, R. J. Kottenstette, E. J. Heller, C. M. Matzke, S. A. Casalnuovo, P. R. Lewis, R. P. Manginell, W. K. Schubert, V. M. Hietala and R. J. Shul, "Integrated chemical analysis systems for gas phase CW agent detection," *Micro Total Analysis Systems*, 1998, pp. 477-480.
- [4] R. P. Manginell, P. R. Lewis, D. R. Adkins, R. J. Kottenstette, D. Wheeler, D. Trudell, J. Byrnes, M. Okandan, J. M. Bauer and R. Manley, "Advancements in the gas-phase MicroChemLab," *2004 Joint International Meeting - 206th Meeting of the Electrochemical Society/2004 Fall Meeting of the Electrochemical Society of Japan*, Oct 3-8, 2004, pp. 2586.
- [5] "SLS Micro Technology," [Online document], Available HTTP: <http://www.sls-micro-technology.de>, 2005.
- [6] B. Wagner, H. J. Quenzer, S. Hoerschelmann, T. Lisec and M. Juerss, "Micromachined bistable valves for implantable drug delivery systems," *IEEE Engineering in Medicine and Biology Society*, 1996, pp. 254-255.
- [7] M. Capanu, J. G. Boyd IV and P. J. Hesketh, "Design, Fabrication, and Testing of a Bistable Electromagnetically Actuated Microvalve," *J Microelectromech Syst*, vol. 9, pp. 181-189, 2000.
- [8] C. K. Ho, M. T. Itamura, M. Kelley and R. C. Hughes, "Review of Chemical Sensors for In-Situ Monitoring of Volatile Contaminants," [Online document], 2001 [cited 03/2005], Available HTTP: <http://www.sandia.gov/sensor/SAND2001-0643.pdf>.
- [9] C. K. Ho, "Micro-Chemical Sensors for In-Situ Monitoring and Characterization of Volatile Contaminants," [Online document], July 13, 2001, [cited 03/2005], Available HTTP: <http://www.sandia.gov/sensor/noframes.htm>.
- [10] W. H. Steinecker, M. Rowe, A. Matzger and E. T. Zellers, "Chemiresistor array with nanocluster interfaces as a micro-GC detector," *IEEE International Solid-State Sensors and Actuators Conference, 8-12 June 2003*, 2003, pp. 1343-6.

- [11] A. J. Ricco and S. J. Martin, "Multiple-frequency SAW devices for chemical sensing and materials characterization," *TRANSDUCERS '91. 1991 International Conference on Solid-State Sensors and Actuators. Digest of Technical Papers, 24-27 June, 1991*, pp. 385-8.
- [12] J. K. Silk and E. R. Schildkraut, "Imaging fourier transform spectroscopy for remote chemical sensing," *Electro-Optical Technology for Remote Chemical Detection and Identification, Apr 8-9, 1996*, pp. 169-177.
- [13] J. Park, W. A. Groves and E. T. Zellers, "Vapor recognition with small arrays of polymer-coated microsensors. A comprehensive analysis," *Anal. Chem.*, vol. 71, pp. 3877-3886, 1999.
- [14] M. Hsieh and E. T. Zellers, "Limits of Recognition for Simple Vapor Mixtures Determined with a Microsensor Array," *Anal. Chem.*, vol. 76, pp. 1885-1895, 2004.
- [15] Meng-Da Hsieh and E. T. Zellers, "Adaptation and evaluation of a personal electronic nose for selective multivapor analysis," *Journal of Occupational and Environmental Hygiene*, vol. 1, pp. 149-60, 2004.
- [16] A. Hierlemann, U. Weimar, G. Kraus, M. Schweizer-Berberich and W. Goepel, "Polymer-based sensor arrays and multicomponent analysis for the detection of hazardous organic vapours in the environment," *Sensors and Actuators, B: Chemical*, vol. B26, pp. 126-134, 1995.
- [17] R. R. Reston and E. S. Kolesar, "Silicon-Micromachined Gas Chromatography System Used to Separate and Detect Ammonia and Nitrogen Dioxide-Part I: Design, Fabrication, and Integration of the Gas Chromatography System," *JMEMS*, vol. 3, pp. 134-146, December 1994.
- [18] "New Enhanced Hand-Held Gas Chromatograph," [Online document], 2002, [cited 03/2005], Available HTTP: <http://www-eng.llnl.gov/GCwebsite/>.
- [19] U. Lehmann, O. Krusemark and J. Muller, "Micro Machined Gas Chromatograph Based on a Plasma Polymerised Stationary Phase," *Proceedings μ TAS*, pp. 167-170, 2000.
- [20] H. Noh, P. J. Hesketh and G. C. Frye-Mason, "Parylene Gas Chromatographic Column for Rapid Thermal Cycling," *JMEMS*, vol. 11, pp. 718-725, 2002.
- [21] "Concept to Volume," [Online document], Available HTTP: <http://www.c2v.nl/>, 2005.
- [22] "Defiant technologies," [Online document], Available HTTP: <http://www.defiant-tech.com/>, 2005
- [23] "Nanodetex corporation," [Online document], Available HTTP: <http://www.nanodetex.com/>, 2005.

- [24] "DARPA MGA," [Online document], Available HTTP: <http://www.darpa.mil/mto/mga/index.html>, 2005.
- [25] M. McGuigan and R. Sacks, "Band-trajectory model for temperature-programmed series-coupled column ensembles with pressure-tunable selectivity," *Anal. Chem.*, vol. 73, pp. 3112-3118, 2001.
- [26] R. Ong, P. Marriott, P. Morrison and P. Haglund, "Influence of chromatographic conditions on separation in comprehensive gas chromatography," *Journal of Chromatography A*, vol. 962, pp. 135-152, 2002.
- [27] L. M. Blumberg and M. S. Klee, "Elution parameters in constant-pressure, single-ramp temperature-programmed gas chromatography," *Journal of Chromatography A*, vol. 918, pp. 113-120, 2001.
- [28] L. M. Blumberg and M. S. Klee, "Quantitative comparison of performance of isothermal and temperature-programmed gas chromatography," *Journal of Chromatography A*, vol. 933, pp. 13-26, 2001.
- [29] M. Van Deursen, H. Janssen, J. Beens, G. Rutten and C. Cramers, "Design considerations for rapid-heating columns applied in fast capillary gas chromatography," *J. Microcolumn Sep.*, vol. 13, pp. 337-345, 2001.
- [30] H. M. McNair and G. L. Reed, "Fast gas chromatography: The effect of fast temperature programming," *J. Microcolumn Sep.*, vol. 12, pp. 351-355, 2000.
- [31] A. J. Grall and R. D. Sacks, "Pressure-tunable column selectivity for high-speed vacuum-outlet GC," *Anal. Chem.*, vol. 72, pp. 2507-2513, 2000.
- [32] H. Smith and R. D. Sacks, "Column selectivity programming and fast temperature programming for high-speed GC analysis of purgeable organic compounds," *Anal. Chem.*, vol. 70, pp. 4960-4966, 1998.
- [33] C. Coutant and R. Sacks, "Programmable control of column selectivity for temperature-programmed GC," *Anal. Chem.*, vol. 72, pp. 5450-5458, 2000.
- [34] C. A. Rich, "A thermopneumatically-actuated silicon microvalve and integrated microflow controller," Ph.D. Dissertation, University of Michigan, 2000.
- [35] IC Sensors Model 4425 Microvalve, "Gas microvalve normally closed low cost," Milpitas, CA, 1997.
- [36] "Redwood Microsystems, Inc.," [Online document], 2004, [cited 03/2005], <http://www.redwoodmicro.com>.
- [37] K. Sato and M. Shikida, "An Electrostatically Actuated Gas Valve With an S-Shaped Film Element," *Journal of Micromechanics and Microengineering*, vol. 4, pp. 205-209, 1994.

- [38] D. Bosch, B. Heimhofer, G. Muck, H. Seidel, U. Thumser and W. Welser, "A silicon microvalve with combined Electromagnetic/Electrostatic actuation," *Sensors and Actuators A*, 1993, pp. 684-692.
- [39] J. Sihler, A. H. Slocum and J. H. Lang, "An electrostatically actuated low-leakage silicon microvalve," *Solid-State Sensor, Actuator, and Microsystems Workshop*, 2004, pp. 282-285.
- [40] K. Skrobaneck, M. Kohl and S. Miyazaki, "Stress-optimised shape memory microvalves," *Micro Electro Mechanical Systems*, 1997, pp. 256-261.
- [41] E. - Yang, C. Lee and J. Mueller, "Normal-closed, leak-tight piezoelectric microvalve under ultra-high upstream pressure for integrated micropropulsion," *Micro Electro Mechanical Systems*, 2003, pp. 80-83.
- [42] X. Yang, C. Grosjean and Y. - Tai, "Design, Fabrication, and Testing of Micromachined Silicone Rubber Membrane Valves," *J Microelectromech Syst*, vol. 8, pp. 393-402, Dec. 1999.
- [43] C. A. Rich and K. D. Wise, "A High-Flow Thermopneumatic Microvalve With Improved Efficiency and Integrated State Sensing," *JMEMS*, vol. 12, pp. 201-208, April 2003.
- [44] K. W. Oh and C. H. Ahn, "A review of microvalves," *J Micromech Microengineering*, vol. 16, pp. 13-39, 2006.
- [45] J. A. Frank and A. P. Pisano, "A low-power, low-leakage, bi-stable planar electrolysis micro gate valve," *Solid-State Sensor, Actuator and Microsystems Workshop*, 2004, pp. 156-159.
- [46] W.-C. Tian and S.W. Pang, "Freestanding Microheaters in Si with High Aspect Ratio Microstructures," *Journal of Vacuum Science and Technology*, pp. 1008-12, 2002.
- [47] H. K. L. Chan, S. W. Pang, R. A. Veeneman, E. T. Zellers and M. Takei, "Microfabricated preconcentrator for quantitative analysis of low concentration volatile organic compounds," *TRANSDUCERS '05. 13th International Conference on Solid-State Sensors, Actuators and Microsystems. Digest of Technical Papers, 5-9 June, 2005*, pp. 2091-4.
- [48] J. A. Potkay, J. A. Driscoll, M. Agah, R. D. Sacks and K. D. Wise, "A high-performance microfabricated gas chromatography column," *Proceedings IEEE Sixteenth Annual International Conference on Micro Electro Mechanical Systems, 19-23 Jan, 2003*, pp. 395-8.
- [49] M. Agah, J. A. Potkay, G. Lambertus, R. Sacks and K. D. Wise, "High-performance temperature-programmed microfabricated gas chromatography columns," *J Microelectromech Syst*, vol. 14, pp. 1039-1050, 2005.

- [50] G. Lambertus, A. Elstro, K. Sensenig, J. Potkay, M. Agah, S. Scheuring, K. Wise, F. Dorman and R. Sacks, "Design, Fabrication, and Evaluation of Microfabricated Columns for Gas Chromatography," *Anal. Chem.*, vol. 76, pp. 2629-2637, 2004.
- [51] J. A. Potkay, G. R. Lambertus, R. D. Sacks and K. D. Wise, "A low-power temperature- and pressure-programmable uGC column," *Solid-State Sensors, Actuators and Microsystems Workshop (Hilton Head)*, 2006, pp. 144.
- [52] W. Y. Cai and E. T. Zellers, "Dual-Chemiresistor GC Detector Employing Monolayer-Protected Metal Nanocluster Interfaces," *Anal. Chem.*, vol. 74, pp. 3533-3539, 2002.
- [53] H. Kim, K. Najafi, A. Astle, L. P. Bernal and P. Washabaugh, "Fabrication and performance of a dual-electrode electrostatic peristaltic gas micropump," *μ TAS*, 2005, pp. 1173-1176.
- [54] H. Kim, A. Astle, K. Najafi, L. P. Bernal and P. Washabaugh, "Integrated peristaltic 18-stage electrostatic gas micro pump with active microvalves," *Solid-State Sensors, Actuators and Microsystems Workshop (Hilton Head)*, 2006, pp. 292-3.
- [55] J. A. Potkay and K. D. Wise, "An electrostatically latching thermopneumatic microvalve with closed-loop position sensing," *18th IEEE International Conference on Micro Electro Mechanical Systems, 30 Jan.-3 Feb, 2005*, pp. 415-18.
- [56] S. Reidy, G. Lambertus, J. Reece and R. Sacks, "High-performance, static-coated silicon microfabricated columns for gas chromatography," *Anal. Chem.*, vol. 78, pp. 2623-2630, 2006.
- [57] Golay, M. J. E., *Gas Chromatography*. New York: Academic Press, 1958,
- [58] G. E. Spangler, "Relationships For Modeling The Performance Of Rectangular Gas Chromatographic Column," *Journal of Microcolumn Separations*, vol. 13, pp. 285-292, 2001.
- [59] T. Veriotti, J. Driscoll and R. D. Sacks, "Separation channel design for a micro fabricated gas chromatograph with atmospheric pressure inlet and air as carrier gas," *WIMS Industrial Advisory Board Meeting*, 2002.
- [60] S. T. Cho, K. Najafi, C. E. Lowman and K. D. Wise, "An ultrasensitive silicon pressure-based microflow sensor," *IEEE Trans. Electron Devices*, vol. 39, pp. 825-835, 1992.
- [61] A. V. Chavan, "An integrated high-resolution capacitive barometric pressure sensing system," Ph.D. Dissertation, University of Michigan, 1999.
- [62] M. Giovanni, *Flat Corrugated Diaphragm Design Handbook*. New York: Marcel Dekker Inc, 1982.

- [63] Chia-Jung Lu, W. H. Steinecker, Wei-Cheng Tian, M. C. Oborny, J. M. Nichols, Masoud Agah, J. A. Potkay, H. K. L. Chan, J. Driscoll, R. D. Sacks, K. D. Wise, S. W. Pang and E. T. Zellers, "First-generation hybrid MEMS gas chromatograph," *Lab on a Chip*, vol. 5, pp. 1123-31, 2005.
- [64] de Boer, M. J., R. W. Tjerkstra, J. W. Berenschot, H. V. Jansen, G. J. Burger, Gardeniers, J. G. E., M. Elwenspoek and van den Berg, A., "Micromachining of Buried Micro Channels in Silicon," *J Microelectromech Syst*, vol. 9, pp. 94-103, March 2000.
- [65] General Electric, *Fluid Flow Databook*, Genium Publishing, 1982.
- [66] M. Kaviany, Author, A. Kanury and Reviewer, "Principles of Heat Transfer," *Appl. Mech. Rev.*, vol. 55, pp. B100-B102, September 2002.
- [67] D. Pitts and L. Sissom, *Schaum's Outline of Theory and Problems of Heat Transfer*. New York: McGraw Hill, 1998.
- [68] J. Mitchell, G. R. Lahiji and K. Najafi, "Encapsulation of vacuum sensors in a wafer level package using a gold-silicon eutectic," *TRANSDUCERS '05. the 13th International Conference on Solid-State Sensors, Actuators and Microsystems. Digest of Technical Papers, 5-9 June, 2005*, pp. 928-31.
- [69] J. K. Robertson, "An Electrostatically-Actuated Integrated Microflow Controller," Ph.D. Dissertation, University of Michigan, 1996.
- [70] P. L. Bergstrom, J. Ji, Y. Liu, M. Kaviany and K. D. Wise, "Thermally-Driven Phase-Change Actuation," *J Microelectromech Syst*, vol. 4, pp. 10-17, March 1995.
- [71] J. H. Jerman, "The Fabrication and Use of Micromachined Diaphragms," *ICSensors, Custom Product Papers and Briefs*, pp. 4-13-4-18, 1989.
- [72] J. A. Haringx, "Design of corrugated diaphragms," *American Society of Mechanical Engineers -- Transactions*, vol. 79, pp. 55-61, 1957.
- [73] L. Renhuai, "Nonlinear analysis of corrugated annular plates under compound load," *Scientia Sinica, Series A (Mathematical, Physical, Astronomical & Technical Sciences)*, vol. 28, pp. 959-69, 1985.
- [74] "Material: Silicon (Si), bulk," [Online document], Available HTTP: <http://www.memsnet.org/material/siliconsibulk/>, 2006.

Distribution List

1	MS 0892	Richard Cernosek	1744
1	MS 0892	R. Joseph Simonson	1716
2	MS 1425	Alex L Robinson	1744
2	MS9018	Central Technical Files	8944
2	MS0899	Technical Library	4536